2010

Experimental Studies of Turbulent Boundary Layers Over a Rough Forward-facing Step and its Coarse Scale Resolution Approximations

Huiying Ren
Wright State University

Experimental Studies of Turbulent Boundary Layers Over a Rough Forward-facing Step and its Coarse Scale Resolution Approximations

A thesis submitted in partial fulfillment
of the requirements for the degree of
Master of Science in Engineering

by

Huiying Ren
B.E, 2007, Dalian University of Technology

2010
Wright State University

Wright State University
SCHOOL OF GRADUATE STUDIES

October 29, 2010

I HEREBY RECOMMEND THAT THE THESIS PREPARED UNDER MY SUPERVISION BY Huiying Ren ENTITLED Experimental Studies of Turbulent Boundary Layers Over a Rough Forward-facing Step and its Coarse Scale Resolution Approximations BE ACCEPTED IN PARTIAL FULFILLMENT OF THE REQUIREMENTS FOR THE DEGREE OF Master of Science in Engineering.

Yanhua Wu, Ph.D.
Thesis Director

George P. G. Huang, Ph.D., Chair
Department of Mechanical and Materials Engineering
College of Engineering and Computer Science

Committee on
Final Examination

Yanhua Wu, Ph.D.

Scott Thomas, Ph.D.

Joseph Shang, Ph.D.

Andrew Hsu , Ph.D.
Dean, School of Graduate Studies

ABSTRACT

Ren, Huiying. M.S.Eng, Department of Mechanical and Materials Engineering, Wright State University, 2010. *Experimental Studies of Turbulent Boundary Layers Over a Rough Forward-facing Step and its Coarse Scale Resolution Approximations.*

High spatial resolution PIV experiments are performed in the $x - y$ plane at two different spanwise positions to compare the turbulent boundary layers over smooth and rough forward-facing-steps as well as the rough step's two coarse scale-resolution approximations. The Reynolds number based on the step's mean height, Re_h, is 3450 and the ratio of the boundary layer thickness to the step's height is $\delta/h = 8$. The roughness topography on the top surface of the rough step is replicated from a realistic turbine blade and is intrinsically three-dimensional and highly irregular. The surface topographies of the coarse scale-resolution approximations of the rough step are obtained from a multi-resolutional analysis using discrete wavelet transform (DWT).

Mean flow structures, Reynolds normal and shear stresses, quadrant analysis of instantaneous ejections and sweeps, spanwise vorticity and characteristics of the coherent spanwise vortices are first compared between flows over the smooth and rough forward-facing steps. The results illustrate that the rough surface conditions on the top surface of the forward-facing step tend to weaken the separated flows from the sharp edge. The comparison of the results at two different measurement positions indicates that the slope of the roughness profile immediately after the step's edge plays an important role in affecting the flow. This is probably due to the local pressure gradients induced by the roughness topography. A relatively strong favorable pressure gradient may prevent the generation of a recirculation region downstream of the step.

The effects of roughness length scales on the forward-facing turbulent flow are explored by comparing the characteristics of the flow over the rough step and its two approximations, A6 and A4, which contain about 44% and 88% of the roughness energy, respectively. It is observed that the coarse-scale roughness only slightly distorts the downstream recircu-

lation region. For the higher resolution step approximation A4, the flow characteristics are significantly modified at measurement position P2 compared with the case of step A6. However, A4 still cannot reproduce the flow over the step of full roughness studied herein. On the other hand, a much smaller difference exists in the flow characteristics between A4 and full surface at position P1 than at P2, suggesting that the high resolution approximation may be needed only in the part of the roughness topography that has a larger impact on the forward-facing turbulent flow.

Contents

List of Figures

List of Tables

List of Symbols

a_j	Singular values of matrix$\mathbf{A}$
A_i	Approximation at level i of the original rough surface
$\mathbf{A}$	Fluctuating roughness heights of the rough surface
$\mathbf{A_k}$	Low-order model of rank k of the rough surface
h	Mean step height
H	Threshold for quadrant analysis
K	Acceleration parameter, $K \equiv \frac{\nu}{U_\infty^2}\frac{dU_\infty}{dx}$
N	Total number of PIV realizations
N_Q	Space fraction occupied by each quadrant event
I_Q	Indicator function of quadrant analysis
Q_i	Different Reynolds-shear-stress contributors

Re_h	Reynolds number $U_\infty h/\nu$
Re_θ	Reynolds number $U_\infty \theta/\nu$
Re_τ	Reynolds number $U_\tau \delta/\nu$
$R_{\lambda\omega}$	Correlation between swirling strength and spanwise vorticity
$\mathbf{U}$	Orthogonal matrix for SVD
U	Streamwise component of the mean velocity
U_∞	Free stream velocity
$\langle u'^2 \rangle$	Streamwise Reynolds normal stress
$\langle v'^2 \rangle$	Wall-normal Reynolds normal stress
$\langle u'v' \rangle$	Reynolds shear stress
$\langle u'v' \rangle\|^{\mathrm{SM}}_{\mathrm{max}}$	Maximum value of the mean Reynolds shear stress over the smooth step
$\mathbf{V}$	Orthogonal matrix for SVD
V	Vertical component of the mean velcocity
$W(a,b)$	Wavelet coefficient
X_r	The attachment length
x	Streamwise direction
y	Wall-normal direction
z	Spanwise direction
δ	Turbulent boundary layer thickness
λ_i	Eigenvalues of $\mathbf{A}\mathbf{A}^T$
λ_{ci}	Swirling strength, the imaginary part of the complex eigenvalue of $\nabla\mathbf{u}$
ν	Kinematic viscosity of the air
σ_u	Streamwise RMS velocity, $\sigma_u = \sqrt{\langle u'^2 \rangle}$
σ_v	Wall-normal RMS velocity, $\sigma_v = \sqrt{\langle v'^2 \rangle}$
$\psi_{a,b}(t)$	A family of functions termed wavelet
$\psi(t)$	Mother wavelet
ω_Z	spanwise vorticity
$\mathbf{\Sigma}$	Diagonal matrix containing singular values of matrix$\mathbf{A}$
$\mathbf{\Sigma_k}$	Diagonal matrix where a_j=0 for $j > k$
$\Delta\mathbf{X}$	Average particle displacement
Δt	Time separation for PIV system
$\nabla\mathbf{u}$	Local velocity gradient tensor
DWT	Discrete wavelet transform
FFS	Forward-facing step
FSC	Fraction surface content: $\frac{(k^A_{rms})^2}{(k_{rms})^2}$
POD	Proper orthogonal decomposition
SVD	Singular value decomposition

Acknowledgement

I am heartily thankful to my advisor, Dr. Yanhua Wu, for his guidance and inspiration during my past two years of studies. His guidance, inspiration and support from the initial to the final level enabled me to achieve this thesis. I owe my deepest gratitude to him. I also would like to extend my thanks to other Committee-on-Studies members: Dr. Thomas and Dr. Shang for their help in my studies.

Dedicated to

This thesis is dedicated to my beloved husband and parents who have always supported me through my studies.

Introduction

1.1 Motivation

Most practical wall-bounded turbulent flows of interest, like flows over turbine blades, through heat exchangers, and over aircraft and ship hulls, are influenced by surface-roughness effects. In some applications, surface defects can be small on an absolute scale but can still be aerodynamically important if they are large relative to the viscous length scale of the turbulence (at high Reynolds number (Re), for example). In most cases surface roughness significantly increases the wall shear stress and can augment heat and mass transfer at the wall, resulting in an increase in the thermal loading of a system. This latter effect can severely reduce the lifetime of vital parts of many practical engineering systems (like turbine blades). Therefore, a clear understanding of the impact of surface roughness on wall-bounded turbulent flow is imperative for successful modeling and control of these flows to improve both the efficiency and lifetime of a variety of practical engineering systems.

Although rough-wall turbulence has received intense research attention for the last several decades (see review articles of Raupach *et al.* (1991) and Jimenez (2004)), almost all of these studies used "simulated roughness" such as sand grain, ordered arrays of elements and wire mesh, etc. However, studies of Bons and his coworkers (Bons *et al.* (2001); Bons (2002)) revealed that the surface topographies on the turbine blades of land-based gas turbines are distinctively different from those of simulated roughness and that the results of past studies on the simulated roughness cannot be directly applied to the realistic rough surfaces to predict the drag and heat transfer coefficient with satisfactory accuracy. Inspired

by their work, Christensen and his coworkers (Wu & Christensen (2007, 2010); Johnson & Christensen (2009); Mejia-Alvarez & Christensen (2010)) have performed several studies to investigate the impacts of realistic highly-irregular rough surface on the zero-pressure-gradient turbulent boundary layer and turbulent channel flows. In spite of these recent efforts, there still exist many research issues concerning the turbulent flows over realistic rough surfaces. One of the issues is that the effects of the realistic roughness on the separated flow at the surface discontinuity such as surface transitions from smooth to rough or from rough to smooth are not yet known. Smooth forward-facing steps have been used to model such surface discontinuities for the study of acoustics in turbulent flows (Ji & Wang (2010)). Another research issue is that, due to the large range of the topographical length scales of the realistic roughness, it is difficult to generate computational grids for advanced modeling even for sophisticated grid generating methods (Bons *et al.* (2008)). Therefore, the impacts of a roughness with reduced complexity on the turbulent flows need to be understood so that the strict requirement for grid generation may be relaxed in CFD studies. The present experimental effort is meant to address some parts of these two research issues.

1.2 Literature review

1.2.1 Forward-facing step flows

Surface discontinuities such as gaps, ribs and panel mismatches exist routinely in many mechanical vehicles which can be representative as steps. Turbulent flows over smooth forward-facing steps (FFSs) have been studied in the past to try to understand the separating and reattaching flow phenomena that is important for many engineering applications such as turbine blade cooling, heat transfer enhancement for electronic devices, and wind energy. The separation and recirculation of the turbulent boundary layer caused by the presence of a FFS have been found to be responsible for the generation of noise and structure vibrations. Also, the understanding of the unique characteristics of the separated and reattached flows

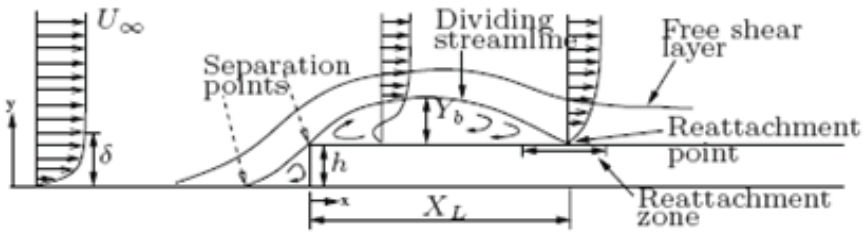

Figure 1.1: Schematic of the features of the forward-facing flow. Sherry *et al.* (2009).

shows significant practical interest in industry.

The features of a turbulent boundary layer over a FFS are shown in figure 1.1 according to the studies of Sherry *et al.* (2009). The upcoming turbulent flow approaches the step from left to right.The experimental studies show that the turbulent flow over FFSs, two recirculation regions exist. One occurs upstream in the lower front corner of the step when the upcoming turbulent boundary layer encounters the adverse pressure gradient incurred by the FFS; the other one occurs downstream on the top surface of the step when the flow is separated by the step's leading edge. A mixing layer which is generated from the impact of the flow at upstream to the step which can expand above the recirculation bubble at the downstream on the top of the step. In the downstream recirculation region on top of the FFS, the attachment length, X_r, which is X_L in Figure1.1, defined as the mean distance between the step's leading edge and the reattachment point.

For the upstream recirculation region, Leclercq *et al.* (2001) pointed that the flow separates at approximately $0.8h$ upstream to the step and reattaches to the approximately $0.6h$ above the vertical surface wall. The measurements were obtained by performing the experiments in a wind tunnel working section for 3 m$\times$0.5 m$\times$0.5 m (length$\times$ width$\times$ Height), free stream velocity of $U_\infty = 50$ m/s, Reynolds number based on height was $Re_h = 1.7 \times 10^5$ and the ratio of boundary layer thickness of the oncoming flow over step height was δ/h=0.7. The forward flow accelerated to 15% above the U_∞, but the forward flow separation does not generate a significant amount of turbulence. Also, the

width of the recirculation bubble increases with the boundary layer thickness, δ, of the oncoming turbulent flow (Moss & Baker (1980)). According to the studies of Bowen and Lindley (1977), the upstream recirculation region contains nearly stagnant flow which acts as an "equivalent" slope angle. For the downstream recirculation region, the sharp corner initiates another separation that extends to $X_r = 3.2h$. Farabee and Casarella (1984) found that X_r varied between $3 \sim 4h$ depending on flow configurations which is much higher than those found in open channel flows which varies between $2 \sim 2.5h$ found by Mohsen (1967). Leclercq *et al.* (2001) found that strong shear occurs at the sharp corner which causes a significant increase of turbulence whose levels is 40% above of free stream, U_∞, are reaching in the shear layer that develops between the recirculation flow and the outer accelerated flow. Also, the highest turbulent levels are located in the first half of the separation region which is $0 < x/h < 1.5$. Sherry *et al.* (2009) also noted that the enhanced local mixing caused by the shear layer above the step and the elevated turbulent intensity within the boundary are the primary mechanisms promoting reattachment.

Laboratory measurements of aerodynamic fields made in separated flows over FFSs with step height, $h = 30$, 40, 50 mm were carried out by Largeau & Moriniere (2007) in s subsonic wind tunnel with open test section 2.35 m $\times$ 1 m$\times$ 0.65 m (length$\times$ width$\times$ Height). The Reynolds number based on step height is $Re_h = 2.88 \times 10^4$ with upcoming free stream velocity $U_\infty = 15$ m/s for step height $h = 30$ mm to $Re_h = 12.82 \times 10^4$ with $U_\infty = 50m/s$ for step height $h = 50$ mm. The aspect ratio l/h (l is width of the open test section) is equal to 15, 11.25, and 9 for $h = 30$, 40 and 50 mm, respectively. According to the studies of Kiya and Sasaki (1983) and Moss and Baker (1979), the ratio of l/h should be greater than 10 to obtain a two-dimensional flow in a closed section wind tunnel, and the ratio of boundary layer thickness over step height is δ/h=0.26, 0.2 and 0.16 for $h = 30$, 40, 50 mm respectively. They noticed that the separation bubble generated by turbulent flow at the front of the step, characterized by very slow motion u = $0.1U_\infty$, is $X_r = 1.27h$, $1.25h$ and $1.22h$ for $h = 30$, 40, 50 mm, respectively. The reattachment

point on the vertical wall for these three scale models are all $0.5h$. On the front step, the flow velocity is accelerated to about u = $1.2U_\infty$ when the fluid passes over the front. This flow separation is responsible for the formation of the recirculation bubble downstream and for the shear layer which develops on the top. For $h = 40$ mm and 50 mm downstream of the front, the recirculation structures develop within the recirculation bubble and are shed downstream. The length of the recirculation bubble, X_r, is in term of the Reynolds number Re_h, the ratio δ/h and the aspect ratio l/h. They also found the recirculation bubble decreases when the ratio δ/h increases. Large scale structures in the shear layer and the low frequency flapping motion at the separation play an important role in the generation of wall pressure fluctuations rather than the near wall pattern bounded in the recirculation zone. After leading edge of the step, locally three-dimensional effects were observed.

Studies on flow features over FFS are summarized recently by Sherry *et al.* (2009). They performed PIV experiment and pressure measurement in two facilities. One is the FLAIR recirculation water channel with a working speed range of $0.09 < U_\infty < 0.64$ m/s over a Reynolds number range $2000 < Re_h < 20000$. The tests run in the water channel is turbulent flow with boundary layer thickness, δ = 40 mm, over smooth FFS in different step heights and the range of ratio boundary thickness over step height of $0.9 < \delta/h < 2.7$. The other facility is a low speed boundary layer wind tunnel with a maximum speed of $U_\infty = 3.4$ m/s over a Reynolds number range $2500 < Re_h < 4300$. The boundary layer thickness of the flow is δ=76mm and the ratio δ/h = 4. Based on the flow conditions, the reattachment length is obtained to be $1.1h < X_r < 4h$ and it tended to increase with the Reynolds number for a given value of δ/h ratio. The sensitivity of the value of X_r varies in two regimes: one is when $Re_h < 8500$ where X_r is heavily dependent on Re_h. The other is for $Re_h > 8500$ where the value of Re_h only weakly affects X_r. But the regimes of Re_h change occurred independently of the ratio of δ/h and the change is postulated to occur due to a change in the dynamic between the upstream and downstream recirculation regions. Indeed, Mohsen (1967) and Tashie *et al.* (2001) illustrated that the structures developing

on the step are immersed in the boundary layer as long as the ratio δ/h is larger and the dimensions of the recirculation bubble is weakly dependent on the external flow velocity when the step is immersed in the upstream boundary layer. Sherry *et al.* (2009) broadly categorized past studies into two groups: $\delta/h > 1$ and $\delta/h < 1$. In the case of $\delta/h > 1$, which is a blunt flat plate, it was shown that X_r is strongly dependent on δ/h although the mechanism of upstream turbulent level is unclear. The reattachment point varies with the unsteady behavior of the shear layer. For $\delta/h < 1$ X_r was relatively insensitive to ratio of δ/h and generally X_r was approximately $4h \sim 5h$. Research of Sherry *et al.* (2009) also revealed that X_r increased monotonically with Re_h for a given δ/h ratio for $2000 < Re_h < 20000$.

Addad *et al.* (2003) used computational fluid dynamics (CFD) with large eddy simulation (LES) of a flow over a forward-backward facing step with step height $h = 50$ mm and longth $l = 10h$. The free stream velocity of the flow is $U_\infty = 50m/s$, $Re_h = 1.7 \times 10^5$ $\delta/h = 0.7$, which is based on the value of the upstream boundary layer thickness reported from the laser doppler anemometry (LDA) measurements of Leclercq *et al.* (2001). In the experiments made by Leclercq *et al.* (2001) and Moss and Baker (1980), for the upstream region, the flow detaches at $0.8h \sim 1.5h$ before the step to reattach on the vertical wall at $0.6h \sim 0.65h$. The corresponding values based on the LES calculation by Addad *et al.* (2003) are $1.2h$ and $0.6h$, respectively. In the downstream region, $X_r = 4.7h$ is obtained by LES which is the same value reported by Moss and Baker (1980), while Leclercq *et al.* (2001) reported a rather smaller distance of $3.2h$. The vortices in the free shear layer show the relation with the acoustic source term identification. The results of LES show great agreement with the LDA data collected by Leclercq *et al.* (2001).

Ji & Wang (2010) performed a CFD study using LES to analyse a flow over FFSs at Reynolds number based on the momentum thickness $Re_\theta = 4100$. The simulations are executed with four different heights of δ/h = 1.89, 7.69, 30 and 120.48, respectively. They obtained excellent agreement with experimental results with the same flow condi-

tion. Furthermore, it is found that the difference in agreement with previous experimental observations is much reduced as the step height is decreased. For the turbulent boundary layer thickness range from 1.89 to 120.48 of the step height, the recirculation regions at the upstream before the step always exist but for the downstream on the top of the step, there is no recirculation region when δ/h is greater than 30.

1.2.2 Impact of low-order models on rough-wall turbulent boundary layers

Christensen and coworkers (Johnson & Christensen (2009); Mejia-Alvarez & Christensen (2010)) have applied singular value decomposition (SVD) which is akin to proper orthogonal decomposition (POD) to produce low-order models of realistic rough surface and studied their impacts on turbulent flows.

In SVD, the matrix $\mathbf{A}$ which represents the fluctuating roughness heights of the rough surface can be decomposed as

$$\mathbf{A} = \mathbf{U}\mathbf{\Sigma}\mathbf{V}^T, \tag{1.1}$$

where $\mathbf{U}$ and $\mathbf{V}$ are orthogonal matrices and $\mathbf{\Sigma}$ is a diagonal matrix containing non-zero singular values of $\mathbf{A}$, a_i, arranged in decreasing order. A low-order model of rank k of the rough surface is then obtained by keeping only the first k leading singular values as

$$\mathbf{A}_k = \mathbf{U}\mathbf{\Sigma}_k\mathbf{V}^T \tag{1.2}$$

where $\mathbf{\Sigma}_k$ is obtained by setting $a_j = 0$ where $j > k$ in $\mathbf{\Sigma}$ and k is less than the rank of $\mathbf{A}$. SVD is related to POD in that the squares of the singular values, a_i^2, are the eigenvalues, λ_i, of $\mathbf{A}\mathbf{A}^T$ or $\mathbf{A}^T\mathbf{A}$. Since the singular values are arranged in non-ascending order, the low-order roughness model $\mathbf{A}_k$ obtained from equation 1.2 is optimum in that $\mathbf{A}_k$ possesses the highest value of the sum of the squares of the roughness heights than any other k-rank roughness approximations.

Johnson & Christensen (2009) performed PIV measurements in turbulent channel flows over short fetches of a full rough surface replicated from a turbine blade damaged by spallation and four low-order representations at ranks of k =1, 5, 10, 20 at $Re_\tau \approx 1828$. They found that a surface model with $k = 20$ (only 9% of the total number of POD modes of the full surface) produces almost the same turbulence statistics such as the mean velocity profile, profiles of Reynolds normal and shear stresses, and the instantaneous shear-stress-contributing events from quadrant analysis, with flow over the full surface. Note than in this study, since the rough surfaces are short, the internal roughness layer developed from the leading edge of the rough surface has not grown to occupy the entire wall-normal extent of the flow yet and therefore the rough-wall flow is a developing channel flow.

Mejia-Alvarez & Christensen (2010) conducted PIV measurements in the streamwise–wall-normal ($x - y$) plane of a zero-pressure-gradient boundary layer over both short and long streamwise fetches of a rough surface and its low-order models at $Re_\theta = 11400$. The rough surface was replicated from a turbine blade damaged by deposition of foreign materials and is the same roughness as studied in the present effort. Low-order models of ranks $k = 5$ and 16 were used as shown in figure 1.2. A comparison of both single- and two-point statistics indicated that a 16-mode model which contains approximately 95% of the full surface content resulted in the same effects as the full rough surface on the turbulent flow under both developing and developed conditions. For the developed flow with long fetches of rough surfaces, both the 5- and 16-mode low-order models reproduced the characteristics of the turbulent boundary layer outside the roughness sublayer. However, neither of the two surface models was found to faithfully reproduce the details of the intense ejections and sweeps within the roughness sublayer.

1.2.3 Objectives of the present study

The objectives of the present study include:

1. Exploring the impacts of the realistic roughness topography which is intrinsically

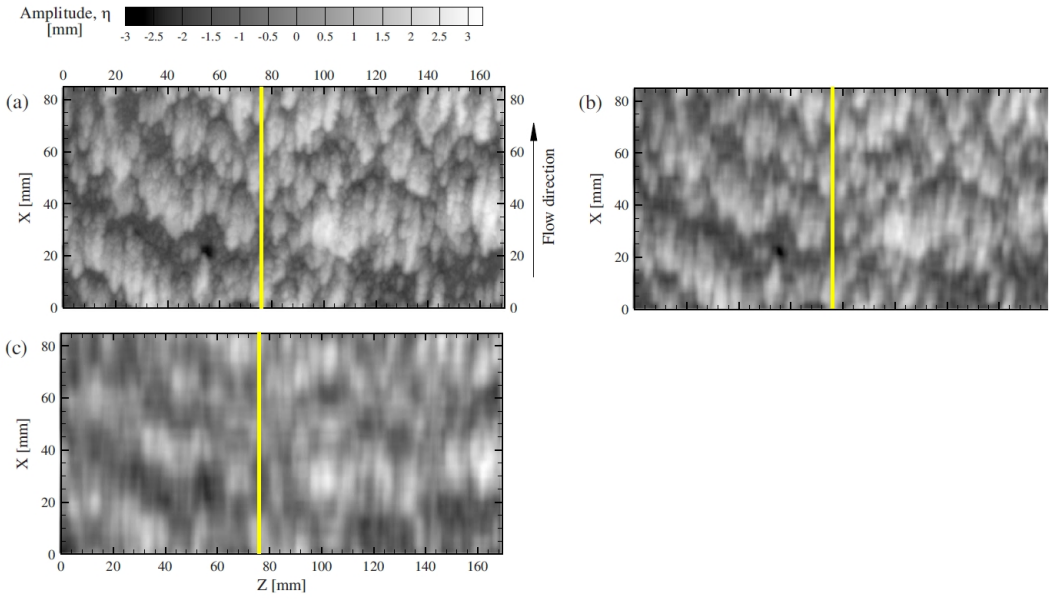

Figure 1.2: (a) Topography of the full rough surface in Mejia-Alvarez & Christensen (2010). (b) Low-order model with the first 16 SVD modes. (c) Low-order model with the first 5 modes.

three-dimensional, highly irregular and random on the turbulent boundary layer over forward-facing steps.

2. Exploring how the turbulent boundary layer will be affected if the rough forward-facing step is approximated at its coarse scale resolutions obtained from discrete wavelet analysis of the roughness topography.

In order to achieve these objectives, high spatial resolution particle image velocimetry (PIV) measurements are performed and various turbulence statistics as well as characteristics of coherent vortical structures are obtained and compared.

Wavelet Analysis of the Roughness

This chapter describes the topography of the rough forward-facing step under current consideration and the details of the discrete wavelet analysis of the roughness topography that yields its approximations at different scale resolutions.

2.1 Roughness

The roughness topography considered herein is replicated from the profilometry measurements of a roughened turbine blade (surface 4 in Bons *et al.* (2001)). This kind of roughness is attributable to the deposition of foreign materials and is often observed on the trailing edge of the pressure surface of land-based turbine blades. The present roughness was scaled from the original topographical information in all three dimensions to yield an average peak-to-valley roughness height of $k = 4.2$ mm and a RMS (root-mean-square) height of $k_{rms} = 1.0$ mm. Figure 2.1 shows a contour plot of this highly irregular rough surface. It can be seen that this realistic roughness is distinct from other idealized ones such as wire mesh and arrays of cylinders or hemispheres. The complexity of this surface is evident by a broad range of topographical scales and random distribution of roughness elements which are generally elliptical in shape and are roughly aligned in the flow direction.

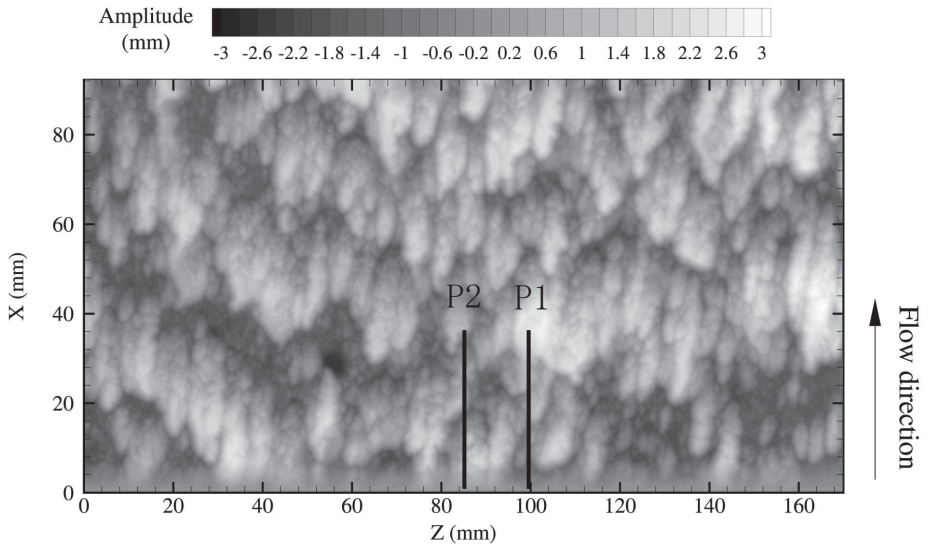

Figure 2.1: Contour plot of the fluctuating heights of the roughness on the top surface of the rough block. P1 and P2 mark the locations of the PIV measurement planes.

2.2 Multi-resolution analysis using discrete wavelets

Wavelet transform has been used in a variety of scientific and engineering applications such as geophysics (Kumar & Foufoula-Georgiou (1997)), biomedical engineering (Liang & Lin (2002)), and image compression (Grgic *et al.* (2001)). The continuous wavelet transform (CWT) of a one-dimensional function $f(t)$ is defined as the integral transform (Daubechies (1992))

$$W(a,b) = \int_{-\infty}^{\infty} f(t)\overline{\psi}_{a,b}(t)dt, \tag{2.1}$$

where $W(a,b)$ is the wavelet coefficient, the overbar denotes complex conjugate, the function

$$\psi_{a,b}(t) = \frac{1}{\sqrt{a}}\psi\left(\frac{t-b}{a}\right) \tag{2.2}$$

represents a family of functions termed wavelets which are generated by scaling and translation of the mother wavelet $\psi(t)$, and a, b are the scale and translation parameters, respectively.

In practice, the discrete wavelet transform (DWT) is usually implemented on sampled

signals to reduce the redundancy and computational complexity of the CWT. In the DWT, the scale parameter a is normally chosen to be powers of 2 and the translation parameter b is chosen to be an integer multiple of the scales to form an orthonormal wavelet basis of $L^2(R)$. That is, the wavelet functions in equation (2.2) are discretized as

$$\psi_{j,k}(t) = 2^{-j/2}\psi\left(\frac{t-2^j k}{2^j}\right), \tag{2.3}$$

and the DWT is given by

$$W(j,k) = \int_{-\infty}^{\infty} f(t)\overline{\psi}_{j,k}(t)dt. \tag{2.4}$$

Multi-resolution analysis (MRA) is an efficient algorithm introduced by Mallat (1989) to perform discrete wavelet transform of a signal. In MRA, a signal can be decomposed at different resolution levels. At each level, the signal is represented by a low-resolution approximation plus the details on that level and on each higher resolution level. That is,

$$f(t) = A_i(t) + \sum_{k=1}^{i} D_k(t), \tag{2.5}$$

where $A_i(t)$ is the approximation at level i and $D_k(t)$ is the detail at level k. The approximation $A_i(t)$ can be computed by

$$A_i(t) = \sum_{k=-\infty}^{\infty} C_{i,k}^A \cdot \phi_{i,k}(t), \tag{2.6}$$

where

$$\phi_{i,k}(t) = 2^{-i/2}\phi(\frac{t-2^i k}{2^i}) \tag{2.7}$$

is a set of orthonormal basis generated from the scaling function $\phi(t)$, which is a companion function of the wavelet function. $C_{i,k}^A$ are the coefficients obtained by projecting $f(t)$ on the basis $\phi_{i,k}(t)$, i.e., $C_{i,k}^A = \int f(t) \cdot \phi_{i,k}(t)dt$. Multi-resolution analysis of a two-dimensional signal such as the rough-surface topography can be derived from 1D DWT described above. The 2D scaling function used to generate approximations of a 2D function is obtained by

multiplying two 1D scaling functions in each direction, i.e., $\phi(x,y) = \phi(x)\phi(y)$.

The Daubechies wavelet of order 10 (db10) is used to generate 7 levels of multi-resolution approximations of the two-dimensional highly irregular roughness topography illustrated in figure 2.2. Daubechies wavelets are a family of frequently used orthogonal asymmetric discrete wavelets. Order 10 is used here due to its regularity so that the multi-resolution approximations of the complex rough surface are smoother and therefore easier to be related to other regular roughness topographies in the future. Further levels of roughness approximations are not pursued since they are only represented by waviness of very low amplitudes. For example, the fractional surface content (FSC), defined by Johnson & Christensen (2009) as the ratio of the variance of the surface approximation to the variance of the original surface $\frac{(k^A_{rms})^2}{(k_{rms})^2}$, for level 8 is only 7%. For comparison, the FSC for the first POD mode of this surface is 30%.

Figure 2.2 presents the multi-resolution surface approximations from level 7 (A_7) to level 2 (A_2). Since A_1 is very close to the original rough surface (FSC=99.9%), it is omitted in the figure. It is seen that at the coarsest resolution, A_7 only shows the broad features of the rough surface and the height variation is slow with large length scales. When the resolution becomes finer, smaller-scale roughness features are emerging in the approximations. This progression of the surface approximations to the original one with scale resolutions can be further illustrated in figure 2.3 which presents roughness height profiles along $z = 144$ mm (This position is chosen arbitrarily). It is seen in figure 2.3 (a) that although the original roughness profile has several prominent peaks, the approximation at the coarse resolution, A_7, only reflect a general trend that the roughness heights on the right is slightly larger than those on the left. With finer resolutions, the roughness profiles in the approximations begin to illustrate distinct peaks as in figure 2.3 (b) and (c). At resolution level 4, the approximation A_4 captures all major roughness peaks in the original surface. A_3 is already an excellent approximation of the highly irregular roughness but at an expense of including much smaller roughness scales. Also note that although A_3 has a FSC as high

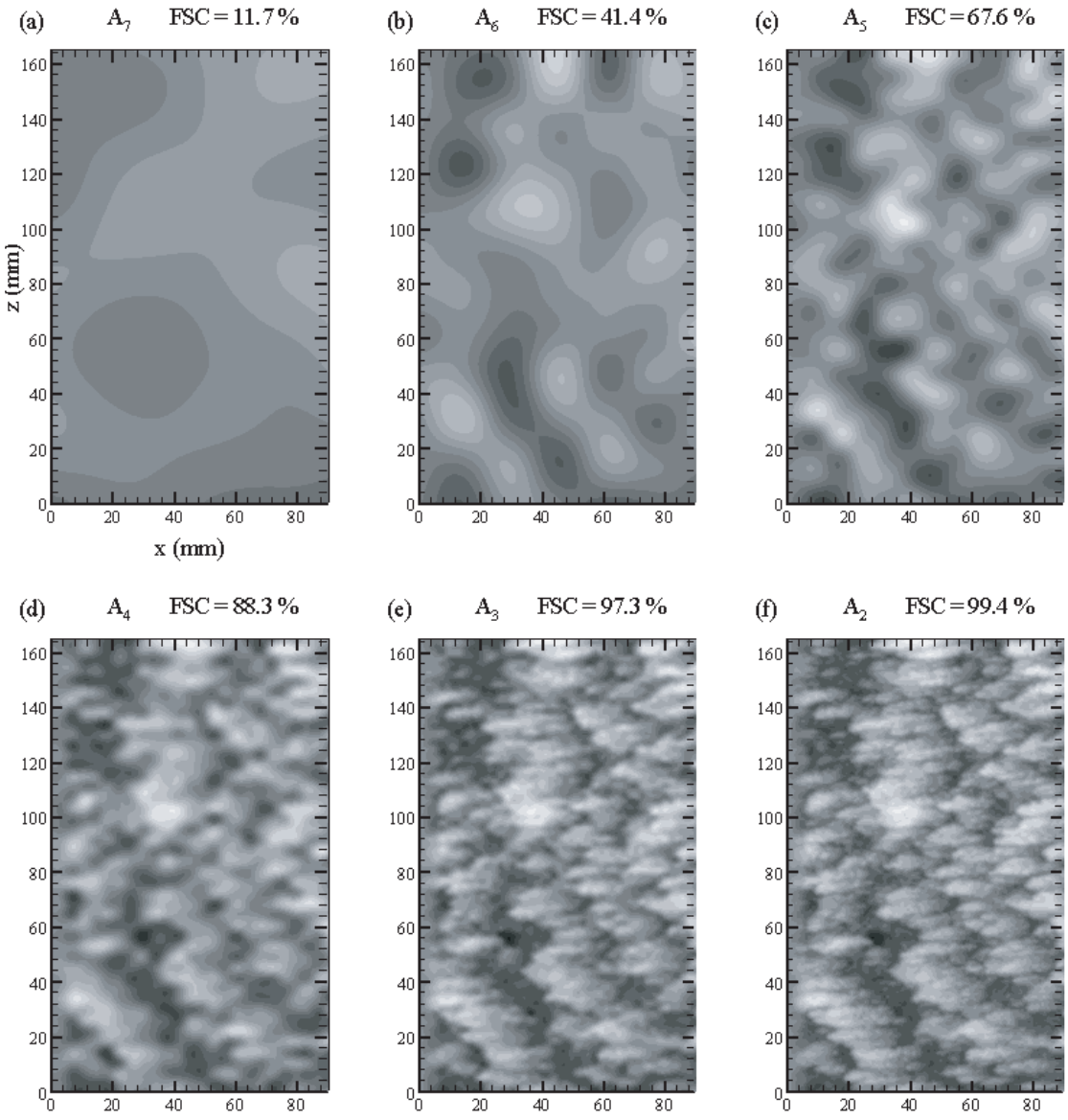

Figure 2.2: Multi-resolution approximations of the highly irregular rough surface. (a) A_7 at level 7; (b) A_6 at level 6; (c) A_5 at level 5; (d) A_4 at level 4; (e) A_3 at level 3; (f) A_2 at level 2. The contour levels are the same as in figure 2.1.

as 97.3%, its profile is still remarkably smooth due to the regularity of the db10 wavelet. Finally, the difference between A_2 and the original rough surface is observed to be trivial as shown in figure 2.3 (f).

A comparison between multi-resolution approximation using DWT and low-order reconstruction using POD of the rough surface is provided below. As mentioned before, the major inadequacy of the POD is its non-universal basis. To understand this, let's take a quarter of the current rough surface (say, 0 mm $\leq x \leq$ 46 mm and 0 mm$\leq z \leq$ 85 mm) as a new surface to compare. The fraction surface content (FSC) for these two surfaces of different sizes are presented in figure 2.4 (a) as a function of POD modes. Firstly, since the number of POD modes is equal to the rank of the roughness matrix, POD for the smaller surface only has half number of the modes as for the full surface. Secondly, the FSC of the first few dominant POD modes are totally different between the full surface and the smaller surface as can be clearly observed in figure 2.4 (a). Therefore, the POD modes used to optimize the variance of the smaller rough surface are entirely different from the modes optimized for the full surface. As a result, it is not straightforward to apply the results of the turbulence studies in a laboratory on a small piece of rough surface to the engineering flows where that laboratory-studied roughness is only a smaller sample of a much larger surface. On the other hand, DWT can overcome this inadequacy of POD. Figure 2.4 (b) shows the roughness profiles along $z = 24$ mm (arbitrarily chosen) in the surface approximations at resolution level 4 for both the full and the smaller surfaces. It is seen that the roughness profile in A_4 of the smaller surface is right on the profile in A_4 of the original surface. As such, unlike the low-order reconstruction using POD modes, the multi-resolution approximation of the roughness using DWT does not depend on the size of the sampled surface.

Another inadequacy of POD is that it optimizes only the variance of the roughness height. On the contrary, DWT offers a local space-scale decomposition of the roughness topography and therefore incorporates local roughness features. Although roughness height

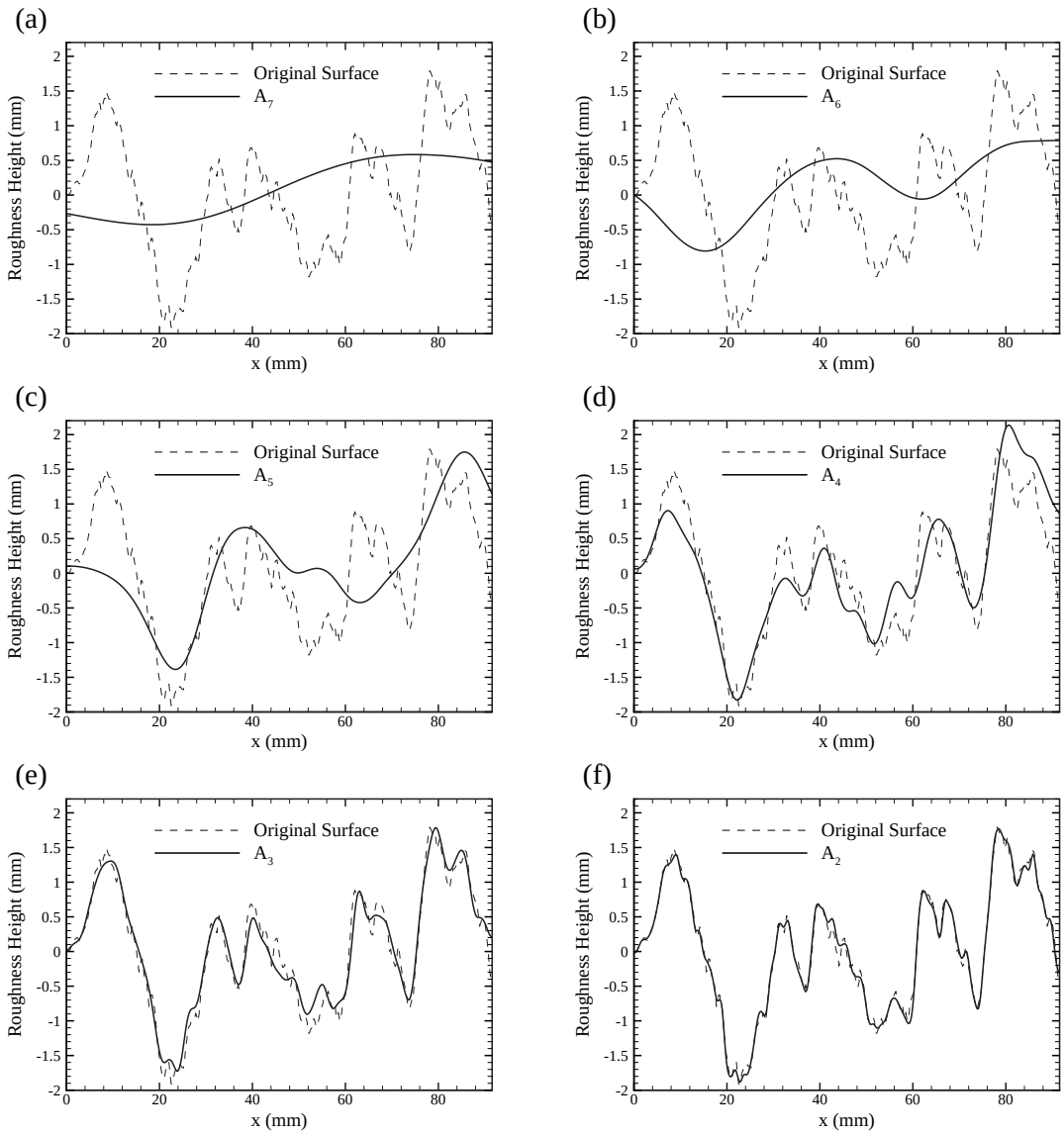

Figure 2.3: Roughness height profiles along $z = 144$ mm in (a) A_7; (b) A_6; (c) A_5; (d) A_4; (e) A_3; and (f) A_2. The roughness height profile at the same z location in the original rough surface is also included as dashed line in each plot for comparison.

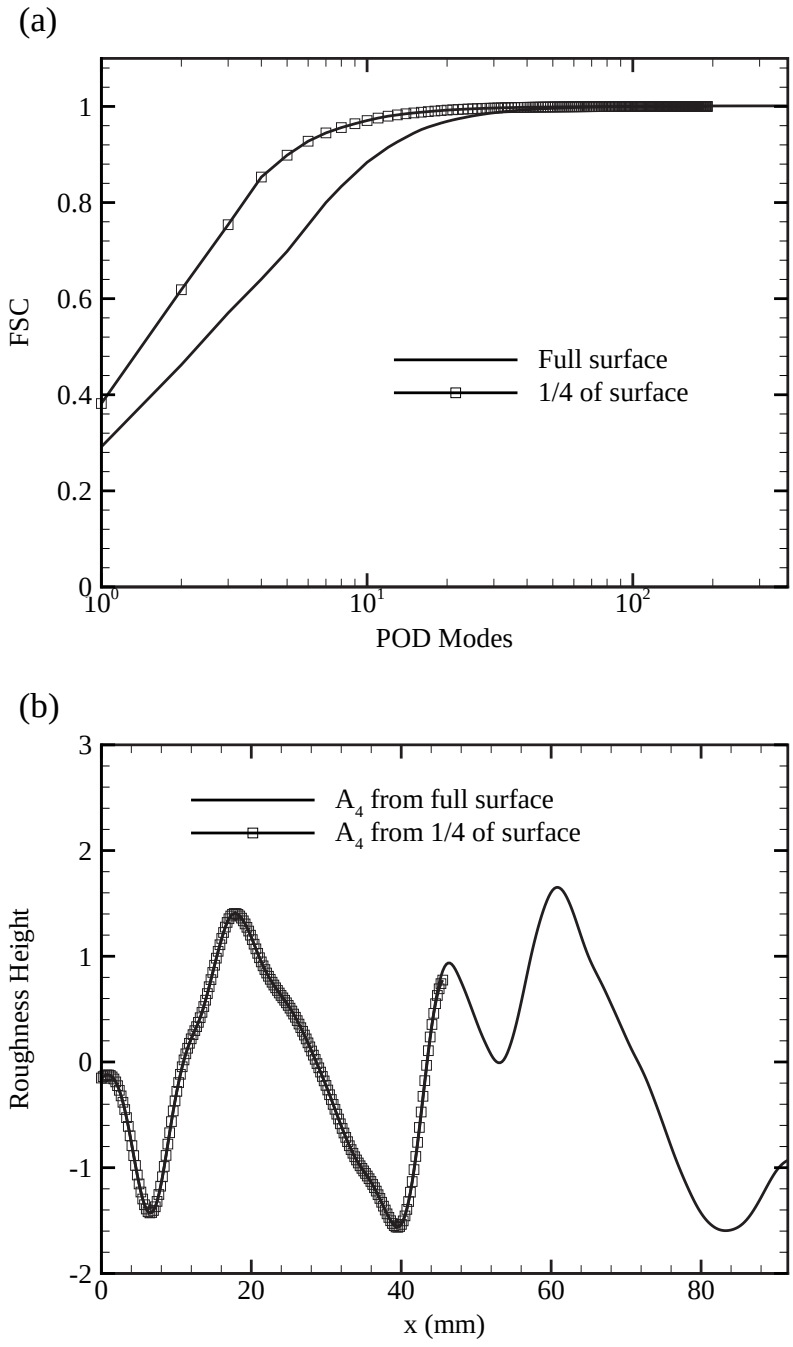

Figure 2.4: The roughness height profile along $z = 24$ mm for surfaces from (a) Fraction surface content (FSC) as a function of POD modes for the full and a quarter of the rough surface. (b) The full and a quarter of the rough surface using DWT at resolution level 4.

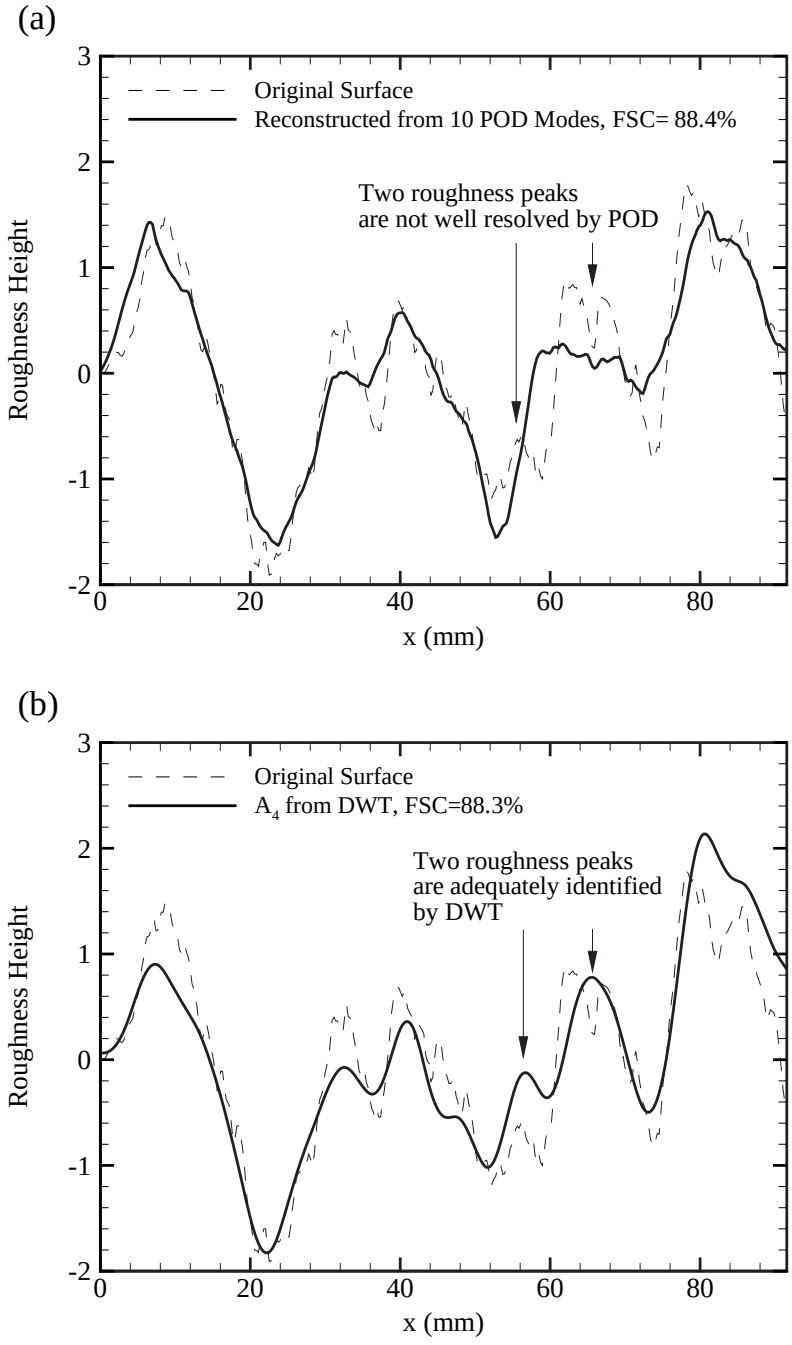

Figure 2.5: The roughness height profile along $z = 144$ mm for surfaces from (a) low-order reconstruction from the first 10 POD modes, (b) Level-4 approximation from DWT (A_4). The roughness height profile at the same z location in the original rough surface is also included as dashed lines for comparison.

is an important roughness parameter that affects the turbulent flows, other parameters such as slope and aspect ratio are also observed to have significant impacts (see Bandyopadhyay & Watson (1988); Schultz & Flack (2009)). Therefore, it may not be enough to optimize just the roughness height using POD. The advantage of DWT in this respect is shown in figure 2.5 which presents the roughness height profiles along $z = 144$ mm for the original surface, level-4 approximation from DWT, and low-order reconstruction from the first 10 POD modes. The two simplified rough surfaces by DWT and POD presented here are suitable for a direct comparison since they have about the same FSC (88.3% for A_4 from DWT and 88.4% for the reconstruction from the first 10 POD modes). As indicated by the arrows in figure 2.5 (a) and (b), two distinct roughness peaks in the original rough surface are clearly identified by DWT but are not well resolved by POD. In addition, it is observed that the approximated rough surface using DWT is much smoother than the one from POD, which is another advantage of DWT.

It has been illustrated that the Wavelet-based multi-resolution approximation is a promising alternative method to proper orthogonal decomposition (POD) for simplifying a realistic highly irregular rough surface for turbulence studies. The inadequacies of the POD method to reduce the complexity of the roughness topography has been shown here to be overcome by the wavelet method. Therefore, in addition to the full roughness topography, its coarse scale resolution approximations at levels A6 and A4 are also studied here to investigate their impacts on the turbulent boundary layers over forward-facing steps. For roughness approximation A6, the average peak-to-valley roughness height is $k = 2.34$ mm and the RMS height is $k_{rms} = 0.64$ mm. For roughness approximation A4, $k = 4.01$ mm and $k_{rms} = 0.94$ mm.

Three rough blocks, the full surface and its two approximations A6 and A4, are fabricated using an Eden 350 3D printer with a resolution of 16 microns at the MechSE Ford Lab at the University of Illinois at Urbana-Champaign. The top surface of these blocks are rough while the bottom surface is smooth. A photo of these blocks is presented in figure

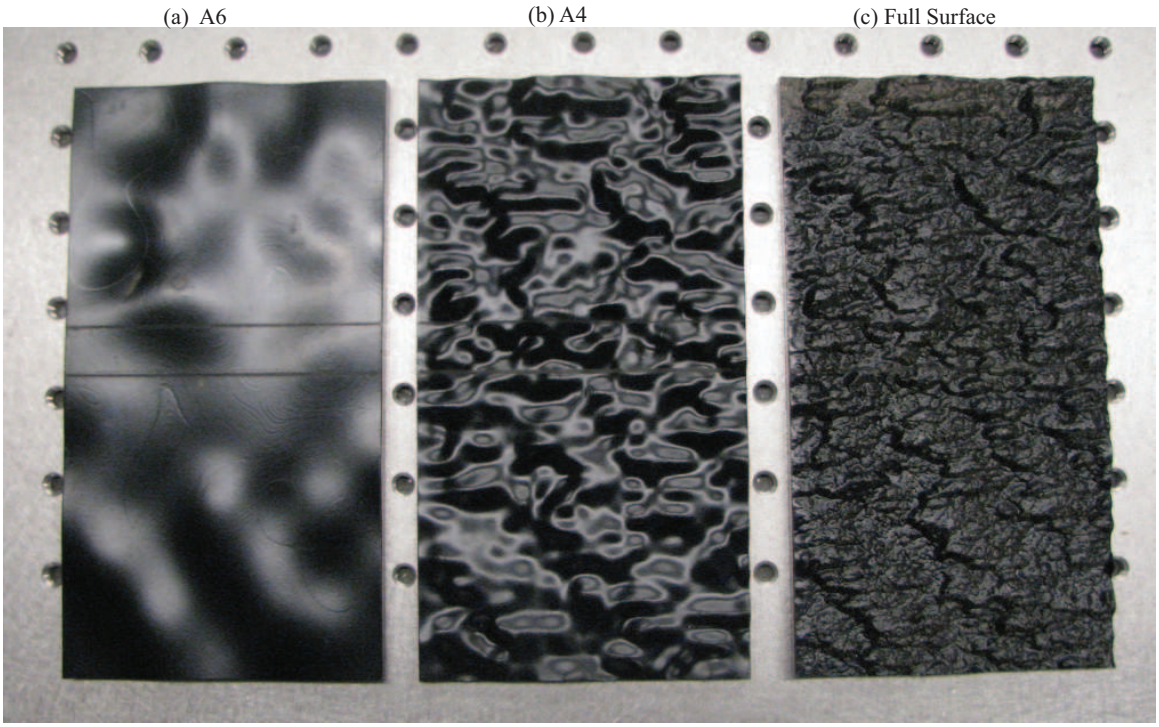

Figure 2.6: Photo of rough blocks for the experiment: (a) Level-6 approximations (A_6), (b) Level-4 approximation(A_4), (C) Full rough surface.

2.6. They are spray painted black in order to reduce the reflection of the laser light sheet during PIV measurements. All the three blocks are of 90 mm (14 h) long, 169 mm (27 h) wide and with a mean height of $h = 6.35$ mm. The current study concentrates on the flow over the forward-facing step (FFS) of the block.

Experiments

This chapter describes all aspects of the experiments undertaken, including a description of the flow facility, PIV system, as well as all details pertaining to the particle image velocimetry (PIV) measurements.

3.1 Flow facility

The particle image velocimetry (PIV) experiments were performed in an Eiffel-type, open circuit, boundary layer wind tunnel at the department of Mechanical and Materials Engineering at Wright State University. It was initially designed by ELD Inc. (Engineering Laboratory Design, Inc. of Minneapolis, MN). A new test section was recently installed to allow optical measurements. The test section is 0.67 m $\times$ 0.67 m in cross-section and 3 m in length. The ceiling and the side walls of the test section are made of high-quality glass to allow optical access. One side wall is composed of two windows that can be opened to facilitate necessary operations inside the test section. The bottom of the test section consists of six removable panels, five of which are made of glass and one of which is made of plexi-glass allowing mounting models for aerodynamic studies. Air is drawn into the tunnel via an elliptical inlet and the flow is conditioned prior to entering the test section with a series of screens and honeycomb to maximize uniformity and minimize turbulence levels. This conditioning yields a freestream turbulence intensity of $\sim$0.45%. The flow rate of the air is controlled through the fan speed by adjusting the frequency input. The boundary layers are developed on a 2.90 m long hydraulically smooth flat plate which has an

elliptically shaped leading edge and is suspended 90 mm above the floor of the tunnel. In order to ensure spanwise uniform transition as well as to stabilize the streamwise location of transition, flow over the flat plate is normally tripped by a 4.7 mm-diameter cylindrical rod placed just downstream of the leading edge of the plate. A 100 mm-long tail flap is attached to the trailing edge of the plate and is set at $\sim 5^\circ$ in the present experiments to prevent separation at the leading edge of the plate. The physical growth of the boundary layer and the inclined tail flap created a slight favorable pressure gradient with the acceleration parameter $K \equiv \frac{\nu}{U_\infty^2}\frac{dU_\infty}{dx} < 7.0 \times 10^{-8}$ at the measurement location, where U_∞ is the freestream velocity and ν is the kinematic viscosity of the air.

3.2 PIV system

Particle image velocimetry (PIV) is a non-intrusive optical technique to measure the instantaneous velocity distribution in a two-dimensional plane of the flow through the imaging of tracer particles embedded within the flow during a very short time interval between times t_1 and t_2. The region of interest is illuminated with two thin sheets of laser light produced by a double-pulsed laser at t_1 and t_2, respectively. The scattered light from the particles is recorded and digitized by a charge-coupled device (CCD) camera. Two-frame cross correlation analysis is performed to extract the average particle displacements, $\Delta\mathbf{X}$, of a small sub-domain of the image field which is called the interrogation region. To the first order, the velocity is estimated to be

$$\mathbf{u} \doteq \frac{\Delta\mathbf{X}}{\Delta t}, \tag{3.1}$$

where $\Delta\mathbf{X}$ is the average displacement of the particles in the interrogation region over the time interval $\Delta t = t_2 - t_1$. A two-dimensional velocity vector field is generated after the velocity information is extracted for each interrogation region across the whole image plane.

A New Wave Research Solo PIV Nd:YAG laser system is used as the illumination

source for the current measurements. The system has two laser cavities and can provide a pair of laser pulse with a minimum time separation of 1 μs at a maximum frequency of 15 Hz. Each laser pulse has a pulse width of approximately 5 ns and about 120 mJ energy.

A series of optics including high-energy mirrors, a spherical lens, a cylindrical lens and prisms are used to generate a thin laser light sheet ($\sim$ 200 μm thick) that is perpendicular to the boundary layer plate and parallel to the flow (streamwise–wall-normal ($x - y$) plane). Since the smooth and rough blocks are not transparent, the laser light is directed from the ceiling of the wind tunnel which is made of glass.

A 1600 $\times$ 1200 pixel (width $\times$ height) Dantec Dynamics 8-bit CCD camera with frame-straddle capabilities is used to image the tracer particles illuminated by the laser light sheet. A Sigma 105 mm focal length lens is used to focus the camera on a field of view in the wind tunnel with a high spatial resolution of 50 pixels/mm.

3.3 PIV measurements

Two-dimensional PIV measurements were performed in the streamwise–wall-normal ($x - y$) plane at two different spanwise positions (P1 and P2 in figure 1) for both smooth and rough FFSs (including full surface, A6 and A4) at $Re_h = \frac{U_\infty h}{\nu}$ =3450, where U_∞ is the freestream velocity, h is the mean step height, and ν is the kinematic viscosity of the air. The flow was seeded with 1 μm droplets generated by a fog generator. As mentioned above, the flow field was illuminated through the transparent glass ceiling with a 200μm-thick laser sheet generated by a pair of Nd:YAG lasers. An 8-bit frame-straddle CCD camera of 1200 $\times$ 1600 pixels was used in conjunction with a 105 mm lens, yielding a field of view of 3.8 h $\times$ 5 h (wall-normal $\times$ streamwise) and a magnification factor of about 50 pixels/mm. Measurements were first made in the upstream region of the steps and then the camera was moved to measure the flow fields downstream of the steps. More than one thousand statistically independent pairs of particle images are acquired for each measurement using

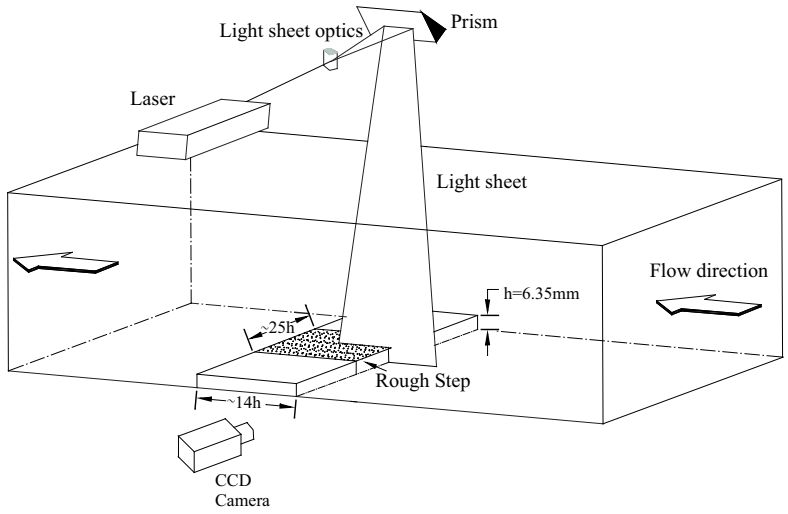

Figure 3.1: Schematic of experimental setup.

Dantec Dynamics FlowMaster software. For each measurement, it needs seven runs each of which takes eight seconds to acquire ∼150 image pairs and it takes about four minutes to save the images from memory to disk. The total acquisition time is about 30 minutes for each measurement. The laser frequency is kept at 15 Hz. The experimental schematic is shown in figure 3.1.

The pairs of PIV images were interrogated using the two-frame cross-correlation method with interrogation window size of 20 $\times$ 20 pixels with 50% overlap. The interrogation was carried out within the *Insight 3G* software (TSI, Inc.). An iterative, two-pass scheme was employed to improve the accuracy of the velocity fields. The resulting velocity vector fields have a grid spacing of 0.2 mm or $h/32$. The relevant PIV interrogation parameters are summarized in Table 3.1.

The vector fields are also validated using objective statistical methods such as magnitude difference comparison and median criteria to remove erroneous velocity vectors. The parameters used in the validation procedures are listed in Table 3.2. On average, 97-99% of the velocity vectors in any given velocity realization are found to be valid minimizing

Table 3.1: PIV interrogation parameters for streamwise–wall-normal ($x - y$) plane measurements. In *Insight 3G*, "PIV Processor Setup", the "Grid Engine", "Spot Mask Engine", "Correlation Engine" and "Peak Engine" are chosen to be "RecursiveNyquistGrid", "No-Mask", "FFTCorrelator" and "GaussianPeak", respectively.

Parameters		Full Surface	A6	A4
Pass 1: ($x \times y$ (pix))	Window 1	32×32	32×32	32×32
	Window 2	32×32	32×32	32×32
Pass 2: ($x \times y$ (pix))	Window 1	20×20	20×20	20×20
	Window 2	20×20	20×20	20×20
Window Offset in x (pix)		0	0	0
Time Separation Δt (μs)		20	20	20
		UPSTRM DWNSTRM	UPSTRM DWNSTRM	UPSTRM DWNSTRM
Magnification (μm/pix)	P1	21.07 21.07	21.01 21.01	20.95 20.95
	P2	22.14 22.14	22.06 22.06	22.16 22.07
Number of Realizations	P1	1057 1101	1567 1117	1309 1036
	P2	1041 1048	1092 1148	1082 1148

Table 3.2: PIV validation parameters for $x - y$ plane measurements.

Procedure	Parameters
Magnitude difference (MD)	1.5
Magnitude difference (MD)	1.5
Interpolate (% neighbors required)	50%
Smooth with Gaussian	0.9

the need for interpolation of holes. Finally, each vector field is low-pass filtered to remove noise associated with frequencies higher than the sampling frequency of the interrogation.

The measurement uncertainty of the instantaneous velocity for the recursive image interrogation procedure used in this study is approximately 0.05 pixels at 95% confidence level (see Scarano (2002)). Upstream approaching the smooth-wall turbulent boundary layer was also measured using PIV at 50 h ahead of the smooth and rough steps. The turbulence statistics of the measured upstream boundary layer was not found to be altered due to the presence of the steps. The Reynolds number based on the momentum thickness of the approaching boundary layer is $Re_\theta = 3130$. The ratio of the upstream boundary

layer thickness to the mean step height is, δ/h = 8, which means the perturbation of the present steps are quite weak (see Bradshaw & Wong (1972)). The roughness Reynolds numbers, $k^+ = ku_\tau/\nu$, for the full roughness and approximations A4 and A6 are 84, 80, and 47, respectively.

Turbulent Boundary Layers Over Smooth and Rough Forward-facing Steps

The focus of this chapter is to explore the impact of the roughness on the turbulent boundary layers over forward-facing steps. Comparison of mean flow structures, Reynolds normal and shear stresses, quadrant analysis of instantaneous shear stress contributing events, and ensemble averaged spanwise vorticity has been performed. The coherent spanwise vortices have also been extracted from the field of correlation between swirling strength and vorticity. The impact of the rough forward-facing step on the characteristics of these vortical structures such as the numbers of vortices, spatial distribution, size and circulation distributions is investigated.

4.1 Mean flow structures

Figure 4.1 shows the ensemble averaged velocity fields for the smooth FFS at positions P1 and P2. The velocity vectors are set to be uniform to highlight the two recirculation regions upstream and downstream of the step. The streamlines are also imposed on the vectors to illustrate the flow fields. The mean velocity fields at either spanwise position clearly shows two separation bubbles located upstream and downstream of the step. The separation point of the upstream recirculation region is found from the x-location where

the streamwise component of the mean velocity is approximately equal to zero, $U \approx 0$, at the grid point closest to the ground. The reattachment position on the vertical side of the step is determined from the y-location where the vertical velocity component is equal to zero, $V \approx 0$. The reattachment position of the downstream recirculation region on the top surface of the step is found from the x-location where $U \approx 0$. No attempts are made to extrapolate the dividing streamline to the wall for these separation and reattachment positions. It is observed from figure 4.1 that the turbulent boundary layer separates at $\sim$0.8h upstream and reattaches to the vertical step wall at $\sim$0.44h above the ground surface for both spanwise positions. The measurement uncertainty is $\pm 0.10h$ (95%) in locating the separation point and is $\pm 0.03h$ in locating the reattachment position on the step's vertical wall. These observations are in good agreement with the results of Leclercq *et al.* (2001). Figure 4.1 also shows that the reattachment length, X_r, is 1.17$\pm 0.03h$ in both PIV measurement planes. It is very close to the value of the reattachment length ($X_r = 1.1h$) obtained from the flow visualization in Sherry *et al.* (2009) for $\delta/h = 4$ and $2500 < Re_h < 4300$, but is quite low compared with other studies ($2 \sim 5h$ Leclercq *et al.* (2001); Gasset *et al.* (2005); Largeau & Moriniere (2007); Camussi *et al.* (2008); Agelinchaab & Tachie (2008); Ji & Wang (2010)), probably due to the large δ/h ratio and the low Reynolds number in the current study. Note that since the current PIV measurements cannot reach very close to the step's surfaces due to laser reflection, the measured values in separation and reattachment point in the upstream recirculation region and X_r for the downstream recirculation region will be slightly lower than the true values. The centers of the separation bubbles in the upstream and downstream recirculation regions are estimated from the streamlines to be ($-0.24 \pm 0.02h$, $0.20 \pm 0.02h$) and ($0.71 \pm 0.05h$, $0.14 \pm 0.02h$), respectively, for both measurement planes. Although "branching structures" may exist in the flow of FFS for large W/h ratios (W is the width of the facility's test section) as observed in Largeau & Moriniere (2007), the resemblance of the mean flow structures shown in figure 4.1 indicates that, at most, the spanwise wavelength of the branching structures in the current

Table 4.1: Locations of the separation point, reattachment position on the vertical wall of the step, and the bubble center in the upstream recirculation region.

	Separation Point	Reattachment Position	Bubble Center
Smooth	$x = -0.80 \pm 0.10h$	$y = 0.44 \pm 0.03h$	$(-0.24 \pm 0.02h, 0.20 \pm 0.02h)$
Rough P1	$x = -0.80 \pm 0.10h$	$y = 0.52 \pm 0.03h$	$(-0.26 \pm 0.02h, 0.21 \pm 0.02h)$
Rough P2	$x = -0.78 \pm 0.10h$	$y = 0.51 \pm 0.03h$	$(-0.26 \pm 0.02h, 0.21 \pm 0.02h)$

study is quite long compared with the separation distance between the two measurement planes. Therefore, only the results at P1 over the smooth step will be presented hereinafter to compare with the rough step cases.

Ensemble averaged flow fields of the rough FFSs at positions P1 and P2 are presented in figure 4.2. The velocities very close to the top surface cannot be measured in the present experiments due to either the laser light sheet reflection or the blockage of the higher roughness elements located closer to the camera. Figure 4.2 shows that the upstream recirculation regions of the rough step are qualitatively similar to those of the smooth step. The locations of the separation point, reattachment position, and the centers of the bubbles in the upstream recirculation region at P1, P2 of the rough step and over the smooth step are summarized in Table 4.1. It can be observed that these values are quite similar between the smooth and the rough steps. Note that not much significance can be attached to the relatively larger difference of about $0.08h$ in the reattachment position between the smooth and the rough steps since the measured velocity vectors for the smooth step are less close to the vertical wall.

On the other hand, the flow field of the downstream recirculation region on the step's top surface is strongly affected by the surface topography of the rough steps. At position P2, the downstream recirculation bubble disappears as shown in figure 4.2 (b). This may be explained by the positive slope of the roughness profile after the sharp edge of the rough step at P2. A local favorable pressure gradient may be generated due to this positive slope and therefore prevents the generation of the separation bubble. In contrast, a clearly

defined bubble is observed at measurement position P1 at the downstream recirculation region. At this spanwise position, the roughness profile illustrates a negative slope and thus may produce a local adverse pressure gradient. The center of this bubble at P1 is observed to be located at (0.83$\pm 0.05h$, 1.14$\pm 0.02h$). Compared with the smooth step case where the downstream recirculation bubble is at (0.71$\pm 0.05h$, 1.14$\pm 0.02h$), the streamwise location of the bubble on the rough step at P1 is moved a bit further downstream while the vertical location is not affected by the roughness. Therefore, the mean velocity fields of the turbulent flow close to the top surface of the rough step are observed to be highly three-dimensional in contrast to the smooth step case and strongly dependent on the specific roughness topographies.

4.2 Reynolds stresses

The normalized streamwise Reynolds's stress, $\frac{\langle u'^2 \rangle}{U_\infty^2}$, over the smooth step is presented in figure 4.3 (a). As the turbulent boundary layer approaches the FFS, the steamwise Reynolds stress is increased slightly due to the presence of the step. The maximum streamwise RMS (root-mean-square) velocity, $\sigma_u = \sqrt{\langle u'^2 \rangle}$ occurs at about (-0.5h, 0.5h) and is approximately 5% of the freestream velocity. However, $\frac{\langle u'^2 \rangle}{U_\infty^2}$ is enhanced significantly within the downstream recirculation region on top of the step initiated by the sharp edge. The highest levels are located in the strong shear layer between the recirculation bubble and the outer high-velocity fluids. The maximum σ_u reaches to about 30% of the freestream velocity, U_∞. This increase in the streamwise RMS velocity agrees with those in the study of Agelinchaab & Tachie (2008) ($\sim$30-34%) but is lower than those found in Leclercq *et al.* (2001) ($\sim$40%) and Sherry *et al.* (2009) ($\sim$37-45%). The main reason for these differences in σ_u may be due to the different δ/h ratios used in these studies: lower levels of σ_u were found in studies with large δ/h ratios (δ/h = 9.3 in Agelinchaab & Tachie (2008) and δ/h = 8 in the present study) while higher levels were observed with relatively small δ/h ratios

(δ/h = 0.8 in Leclercq *et al.* (2001) and δ/h = 0.9$\sim$4 in Sherry *et al.* (2009)). For a lower δ/h, the region with higher velocity within the turbulent boundary layer is perturbed by the step and thereby generating more streamwise turbulence.

The normalized streamwise Reynolds's stress, $\frac{\langle u'^2 \rangle}{U_\infty^2}$ over the rough FFS at measurement positions P1 and P2 are presented in figure 4.3 (b) and (c), respectively. It can be observed that the streamwise Reynolds normal stresses ahead of the rough step at these two different spanwise positions are very similar to that over the smooth step. Obvious differences are present in flow regions above the rough step where the flows are directly affected by the specific roughness topographies. At P1 where the roughness profile possesses a negative slope immediately downstream of the sharp edge, the peak σ_u value is reduced by about 27% and the region with high levels of $\frac{\langle u'^2 \rangle}{U_\infty^2}$ extends less further downstream when compared to the smooth step case. At position P2 where a positive-slope roughness profile follows the sharp edge, large values of $\frac{\langle u'^2 \rangle}{U_\infty^2}$ do not appear to extend beyond $x = h$, in contrast to the smooth step case. However, the peak σ_u is comparable to that over the smooth step at this spanwise measurement position.

Figure 4.4 (a) shows the normalized wall-normal Reynolds stress, $\frac{\langle v'^2 \rangle}{U_\infty^2}$, over the smooth FFS. The black line overlaid in this figure is the contour line corresponding to a zero mean wall-normal velocity, $V = 0$. The mean wall-normal velocity is negative inside the region enclosed by this line and V is positive outside of this contour line. It can be observed that as the turbulent boundary layer approaches the step, The maximum wall-normal RMS velocity, $\sigma_v = \sqrt{\langle v'^2 \rangle}$ is increased up to 10% of the freestream velocity in the recirculation region ahead of the FFS. Another region of high levels of wall-normal Reynolds stress is located in the vicinity of the sharp edge of the step in which σ_v is also about 10% of U_∞. Further downstream of the step is a large region with significant levels of wall-normal Reynolds stress that extends beyond the current field of view of $5h$. The peak σ_v in this region is found to be approximately 17% of the freestream velocity, U_∞. In addition, a majority of this region is found to be located in where $V < 0$. As such, the generation of the

large amounts of the wall-normal Reynolds stress in this region may largely be associated with the process that the free stream is trying to recover from the adverse pressure gradient and to reattach to the top surface.

Wall-normal Reynolds stresses over the rough FFS at P1 and P2 are presented in figures 4.4 (b) and (c), respectively. It is seen that the two smaller regions of elevated $\langle v'^2 \rangle$ located both ahead of the step and in the vicinity of the step's edge are quite similar irrespective of the surface conditions on the step's top surface. However, the distribution of $\langle v'^2 \rangle$ within the large region over the top of the step is strongly dependent on the surface topography. At position P1, the coherence of the highest levels of $\langle v'^2 \rangle$ observed between $0.8h$ and $2.2h$ is broken by the roughness. However, the peak σ_v is still comparable to the value over the smooth step. Unfortunately, no information is available in the flow region very close to the roughness and therefore the correspondence between the roughness profile and the distribution of $\langle v'^2 \rangle$ cannot be inferred in the current study. At position P2, the levels of the wall-normal Reynolds stress are significantly suppressed, probably due to the favorable pressure gradient locally produced by the roughness topography that balances part of the adverse pressure gradient generated by the step's edge. Remarkably, the region with high levels of $\langle v'^2 \rangle$ between $0.8h$ and $2.2h$ over the smooth step disappears at measurement position P2. Further downstream, the wall-normal Reynolds stress is also much weaker when compared not only with $\langle v'^2 \rangle$ over the smooth step but also with that at position P1 of the rough step.

The Reynolds shear stress, $\frac{\langle u'v' \rangle}{U_\infty^2}$, over the smooth step is presented in figures 4.5 (a). The shear stress of the turbulent boundary layer is slightly increased around the sharp edge of the step. Immediately downstream of the step, a small region of strong positive Reynolds shear stress exists. Further downstream is a large region of high levels of negative shear stress, indicating a strong turbulent mixing process that entrains high momentum freestream fluid into the recirculation region above the step. The distributions of the Reynolds shear stress over the rough step at P1 and P2 (figures 4.5 (b) and (c), respec-

tively) show that $\langle u'v' \rangle$ is reduced by the surface roughness, more significantly at P2 due to its positive slope of the roughness profile immediately downstream of the step. It is also interesting to note that at measurement position P2, very little Reynolds shear stress is produced around $x = h$ where, in contrast, $\langle u'v' \rangle$ obtained significant values for smooth step and rough step at position P1.

4.3 Quadrant analysis

Since Reynolds shear stress can be contributed by four different quadrant events, outward interactions (Q1), ejections (Q2), inward interactions (Q3), and sweeps (Q4), two-dimensional quadrant analysis is performed to study the impact of the step's surface roughness conditions on the dominant Reynolds-shear-stress contributors. Similar to the one-dimensional analysis conducted recently by Wu & Christensen (2006 a) and Mejia-Alvarez & Christensen (2010), the mean Reynolds shear stress at each grid across the whole PIV field of view is decomposed into contributions from four quadrants excluding a hyperbolic hole of size H as

$$\langle u'v' \rangle(\mathbf{x}) = \frac{1}{N} \sum_{j=1}^{N} u'(\mathbf{x}) v'(\mathbf{x}) I_Q(\mathbf{x}), \tag{4.1}$$

where N is the total number of PIV realizations and I_Q is the indicator function defined as

$$I_Q(\mathbf{x}) = \begin{cases} 1, \text{ when } |u'(\mathbf{x}), v'(\mathbf{x})|_Q \geq H |\langle u'v' \rangle|^{\mathrm{SM}}_{\mathrm{max}} \\ 0, \text{ otherwise.} \end{cases} \tag{4.2}$$

where $|\langle u'v' \rangle|^{\mathrm{SM}}_{\mathrm{max}}$ represents the maximum value of the mean Reynolds shear stress over the smooth step. This universal threshold is used here in order to clarify the effects of the roughness on the quadrant events relative to the smooth step case. The space fraction occupied by each quadrant event for a given H is given by

$$N_Q(\mathbf{x}) = \frac{\sum I_Q(\mathbf{x})}{N} \tag{4.3}$$

Hole sizes $H = 0$ and 4 are used here to represent shear stress contributions from all and only strong events, respectively. Of particular interest in this study are the Q2 (ejections) and Q4 (sweeps) events which contribute the most to the Reynolds shear stress.

Figures 4.6 presents contributions of ejections (Q2 events) and sweeps (Q4 events) to the Reynolds shear stress for the threshold of $H = 0$ over the smooth FFS, the rough step at two different spanwise measurement positions P1 and P2. In the vicinity of the sharp edge, the majority of the shear stress contributions is coming from ejections while the contributions from sweeps are mainly concentrated in front of the step. Further downstream, ejections contribute a little more than sweeps. In addition, contributions from the ejections are distributed slightly further away from the top surface of the step than the contributions from the sweeps. It can also be observed that ejections and sweeps contribute negligibly in the small region immediately downstream of the sharp corner where the Reynolds shear stress is positive, as shown in figure 4.5. In that region, the positive Reynolds shear stress is almost equally contributed by outward (Q1) and inward interactions (Q3) as shown in Figure 4.7. Compared to the smooth FFS case, Reynolds shear stress contributions from Q2 and Q4 events are smaller over the rough step at both P1 and P2 positions, resulting in a smaller mean Reynolds shear stress over the rough step as shown in figure 4.5.

The space fractions occupied by ejections and sweeps for $H = 0$ over the smooth step, the rough step at two different spanwise measurement positions P1 and P2 are shown in figure 4.8. The space fractions appear similar for steps with different roughness topographies. In the vicinity of the sharp edge, sweeps occupy around 40% of the space which is a little higher than approximately 30% occupied by the ejections, although in this region sweeps contribute less than the ejections to the Reynolds shear stress as shown in figure 4.6. In the small region immediately downstream of the corner, both ejections and sweeps occupy about 10%, meaning outward and inward interactions occupy $\sim$ 80% of the total space. Further downstream of the step, the distributions of the space fractions for ejections and sweeps illustrates an opposite trend. Ejections occupy $\sim$35-40% of the space close to

the step's top surface while they occupy much less space ($\sim$25%) further way into the free stream. On the contrary, sweeps occupy less space closer to the step's top surface.

Figure 4.10 presents Reynolds shear stress contributions from ejections and sweeps for the smooth and rough steps at P1 and P2 at a threshold of $H = 4$ which includes only the most intense $u'v'$ events. At $H = 4$, the plots of space fractions as shown in Figure 4.9 illustrate that locations with high stress contributions from ejections or sweeps are where such events occupy more spaces. In the vicinity of the sharp edge, there is very little contribution from strong sweeps. On the other hand, intense ejections which occupy only 5% of the total space contribute about 50% of the mean Reynolds shear stress in this region. Furthermore, the surface conditions of the step do not appear to affect their shear stress contributions or space fractions around the sharp edge. Further downstream of the step, similar to the case for $H = 0$, ejections are found to contribute slightly more than sweeps irrespective of the surface conditions. The contributions from either ejections or sweeps can reach as high as 2/3 of the Reynolds shear stress while their space fractions are less than 10%. However, the regions with large contributions from intensive Q2 and Q4 events do not completely overlap: contributions from intensive sweeps are closer to the step's top surface while contributions from intensive ejections are located further away from the step's top surface. The roughness on top of the step reduces the occurrence of intense ejections and sweeps and thereby reduces their contributions to the Reynolds shear stress downstream of the step. A stronger inhibition of Q2 and Q4 events is observed at position P2 where the roughness topography possesses a positive slope immediately following the step, probably due to the local favorable pressure gradient generated by the roughness.

4.4 Spanwise vorticity

Figure 4.11 (a) shows the ensemble averaged spanwise vorticity, $\omega h/U_\infty$, over the smooth step. It can be observed that the vorticity of the incoming turbulent boundary layer close

to the ground surface starts to decrease slightly when the flows approaches the FFS and reaches a quite small value between -1.2h and -0.4h. The vorticity becomes stronger again at the lower corner in front of the step apparently due to the existence of the recirculation bubble. Downstream of the step, the sharp edge generates a shear layer with very strong vorticity. The strongest vorticity occurs slightly downstream of the step's sharp edge at about 0.25 h and ω drops to around 15% of its peak value beyond about 2h downstream of the leading edge.

The ensemble averaged vorticity over the rough step at P1 and P2 are presented in figures 4.11 (b) and (c), respectively. Upstream of the step, the vorticity is not much different between the smooth and rough steps. More noticeable effects of the roughness are found on the vorticity fields downstream and close to the top surface of the step, as may be expected. Compared with the smooth-step case, the peak vorticity in the downstream shear layers in both measurement planes of the rough step is significantly reduced, especially for the P2 position, which is probably due to the local favorable pressure gradient caused by the positive slope of the roughness profile. Although figure 4.11(b) shows that the shear layer on top of the rough step at P1 is extended only slightly further downstream compared to that over the smooth step, figure 4.11(c) illustrates that the shear layer generated at P2 maintains noticeably strong vorticty for a much longer distance downstream. It appears that although the leading edge roughness at position P2 prevents a separated flow, this benefit is discounted by a sustained high level of vorticity further downstream over the top surface of a rough step.

4.5 Characteristics of spanwise vortices

The spanwise vortices created by the roll-up of the shear layer between the freestream and the recirculation region were found to play important dynamic roles (Kiya & Sasaki (1983)). Since vorticity can be contaminated by the strong shear strain rate in turbulent

flows and free shear layers (Dubief & Delcayre (2000); Jeong & Hussain (1995)), coherent vortical structures have been identified by using other advanced methods such as those based on continuous wavelet transforms (Schram *et al.* (2004)) and on the analysis of local velocity gradient tensor, $\nabla\mathbf{u}$ (Zhou *et al.* (1999); Chakraborty *et al.* (2005); Jeong & Hussain (1995); Hunt *et al.* (1988); Chong *et al.* (1990)). Among them, swirling strength (λ_{ci}), the imaginary part of the complex eigenvalue of $\nabla\mathbf{u}$, has recently been successfully applied on velocity fields obtained from PIV measurements in turbulent flows to elucidate vortical structures whose rotational sense is identified by assigning the sign of the fluctuating spanwise vorticity to λ_{ci} (Wu & Christensen (2010); Natrajan *et al.* (2007)).

In this study, the correlation between swirling strength and spanwise vorticity obtained from 2D PIV velocity fields, defined as

$$R_{\lambda\omega}(\mathbf{x}) = \lambda_{ci}(\mathbf{x}) \times \omega_z(\mathbf{x}) \tag{4.4}$$

is introduced to identify spanwise vortices. Not only does $R_{\lambda\omega}$ reveal the rotational sense of vortices but it will also enhance the signal to noise ratio compared to the swirling strength field. The efficacy of $R_{\lambda\omega}$ to suppress the noise embedded in the swirling strength fields is illustrated in figures 4.12 (a) and (b) which present the three-dimensional contour plots of λ_{ci} and $R_{\lambda\omega}$, respectively, computed from the same instantaneous velocity field. It is clear that much less small-scale noise exists in the field of $R_{\lambda\omega}$ than in the swirling strength field.

Two times the ensemble and area averaged standard deviation of $R_{\lambda\omega}$ over the smooth step is used as the magnitude threshold for valid vortices. As in quadrant analysis, a universal magnitude threshold based on the smooth step case is used in order to evaluate the effects of the roughness on the characteristics of the spanwise vortices. Note that slightly higher thresholds have been used in experiments than in numerical simulations in order to minimize the effect of experimental noise associated with the computation of velocity gradients. For example, two times the standard deviation of vorticity is used by Schram *et al.* (2004) and 1.5 times the standard deviation of λ_{ci} is used by Wu & Christensen (2006

b) and Natrajan *et al.* (2007) to elucidate vortices from PIV measured velocity fields. Only one RMS of Q, the second invariant of $\nabla\mathbf{u}$, is used as the threshold in the numerical simulations of turbulent open channel flow by Nagaosa & Handler (2003). Nevertheless, two different thresholds, 1 and 1.5 times the RMS value of $R_{\lambda\omega}$ are also tried to test the dependence of the results on the values of the thresholds. With 1 RMS of $R_{\lambda\omega}$, about 30% more vortices are identified while only approximately 11% more are found for the threshold of 1.5 RMS compared with the total number of vortices identified for 2 RMS. Therefore, the number of vortices is relatively insensitive to the threshold levels between 1.5 and 2 times standard deviations of $R_{\lambda\omega}$. All other results concerning the characteristics of spanwise vortices presented here are not observed to have any dependence on the threshold levels. The flow region upstream and downstream of the steps are analyzed separately using their own standard deviations of $R_{\lambda\omega}$ over the smooth step. As can be inferred from the vorticity field presented in figure 4.11, the threshold in the flow region downstream of the step is almost three times of that in the upstream region. Therefore, two times the RMS value of $R_{\lambda\omega}$ in the downstream region will be too strong a threshold for the upstream region of the step. Additionally, since the size of the smallest resolvable vortex is limited by the spatial resolution of the PIV measurements, a size threshold is subsequently applied to the $R_{\lambda\omega}$ fields after the magnitude threshold is applied. Similar to the study of Wu & Christensen (2006 b), clusters of $R_{\lambda\omega}$ with fewer than three grid points across their span in both x and y directions are not considered as valid vortices due to insufficient spatial resolution. As in Wu & Christensen (2006 b), vortices with negative $R_{\lambda\omega}$ (clockwise rotation when the flow is from left to right) are termed prograde vortices and those with positive $R_{\lambda\omega}$ (counter-clockwise rotation) are termed retrograde vortices.

The number of vortices per measurement field both upstream and downstream of the smooth and rough steps at an interval of h in the streamwise direction are presented in figure 4.13. In the flow region upstream of the steps, figure 4.13 (a) shows that the numbers of prograde vortices between the smooth step and the rough step at P1 and P2 positions are

differed by ∼10% and therefore the effect of the roughness on top of the steps is considered small. Figure 4.13 (b) shows that the number of retrograde vortices in front of the steps is much less than that of prograde ones. However, it is obvious that the number of retrograde vortices are increased when the flow approaches the step. There are more than twice as many retrograde vortices within h ahead of the step than 4 h ahead of the step. The effect of the roughness on the number of retrograde vortices is also seen to be very small. Within 1 h downstream of the steps, figure 4.13 (c) illustrates that the number of prograde vortices over the rough step at P2 is more than 40% lower than that over the smooth step while approximately the same number of prograde vortices are observed between P1 and the smooth step. At $1h < x < 2h$, compared with the number of prograde vortices over the smooth step, 40% less vortices are found over the rough step at P1 and about 50% less vortices are observed at P2. Further downstream, the difference in prograde vortex numbers is reduced to within about 15%. Finally, figure 4.13 (d) shows that there exist negligible numbers of retrograde vortices within 1 h downstream of the steps. Albeit the numbers of retrograde vortices are all very small over $1h < x < 2h$, approximately half the number of retrograde vortices are found over the rough steps than over the smooth step. The effect of the roughness on the number of retrograde vortices is becoming smaller further downstream of the step.

The spatial probability distributions of the prograde vortices are presented in figure 4.14. In the boundary layer far upstream of the step, more prograde vortices exist closer to the wall, which is consistent with Wu & Christensen (2006 b). When the boundary layer approaches the step, vortices are convected further away from the wall due to the deflection of the streamlines. As the turbulent boundary layer approaches the step, prograde vortices are diffused further away from the bottom wall. The spatial distributions of the prograde vortices upstream of the step are the same irrespective of the roughness conditions on top of the steps. Downstream of the step, the PDF functions spread further into the free stream along the streamwise direction. A narrow band of high probability to find prograde vortices

exists between about $0.2h$ and $1h$ downstream of the smooth step. The peak PDF region is extended further downstream for the rough step at position P1. At position P2 of the rough step, high probability exists in a much smaller region right after the step's front and several other scattered spots as far as beyond $3h$ downstream of the step.

Probability density functions of the sizes of prograde vortices downstream of the steps along the streamwise direction are presented in figure 4.15 (a), (b) and (c). The PDF functions are all peaked at the same size irrespective of the downstream directions and roughness conditions. The PDFs are similar for both the smooth step and the rough step at P1 position in that more large-size vortices occur within 2 h of the step. In contrast, figure 4.15 (c) shows that the vortex size distributions over the rough step at P2 are essentially the same at different streamwise locations. On the other hand, the size distributions of the prograde vortices upstream of the steps (as shown in figure 4.16 (a), (b) and (c)) and the size distributions of the retrograde vortices both upstream (as shown in figure 4.16 (d), (e) and (f)) and downstream of the steps (as shown in figure 4.15 (d), (e) and (f))) are invariant to either the streamwise locations or the step's surface conditions. The comparison of the size distribution for prograde vortices downstream of the steps between smooth and rough steps is presented in figure 4.17 (a) and (b). Within 2 h, there is no difference between the smooth step and the rough step at P1 position. However, at P2 position of the rough step, there is a significantly smaller chance of large-size vortices. Beyond 2 h, the vortex size distributions are not changed by the surface conditions. It is also observed that neither the size distributions of the prograde vortices ahead of the steps nor those of the retrograde vortices as shown in figure 4.17 (c) and (d) are sensitive to the step's roughness conditions.

Probability density functions of circulation for vortices detected downstream of the steps as a function of streamwise locations are illustrated in figure 4.18 (a), (b) and (c). Both prograde and retrograde vortices have peak circulation at about 0.02 $U_\infty h$ and their circulation distributions do not change very much beyond 3 h along the streamwise directions. These trends are the same for both smooth and rough steps. However, the PDFs of

prograde vortices for large circulation (tails of the PDFs) at $0 < x/h < 1$ are significantly higher than the PDFs beyond 3 h for both smooth step and the rough step at P1. At P2 of the rough step, the PDF at $0 < x/h < 1$ is only slightly higher than those beyond $x/h > 3$. Further, the PDF at $1 < x/h < 2$ at position P2 is nearly the same as those beyond 3 h, in contrast to other two cases. The PDFs of the circulation for vortices upstream of the steps are invariant to the streamwise locations as present in figure 4.18 (d), (e) and (f). The circulation distributions for vortices downstream of the steps are compared in figure 4.19. It is observed that there is significantly less chance to find prograde vortices of large circulation at $0 < x/h < 2$ over the rough step at position P2 than at P1 and over the smooth step. The circulation distribution for both prograde and retrograde vortices beyond 2 h are the same irrespective of surface conditions of the step as shown in figure 4.19 (b). Finally, the pdfs of circulation for prograde and retrograde vortices identified upstream of the steps are also invariant to the roughness conditions as present in figure 4.18 (d), (e) and (f).

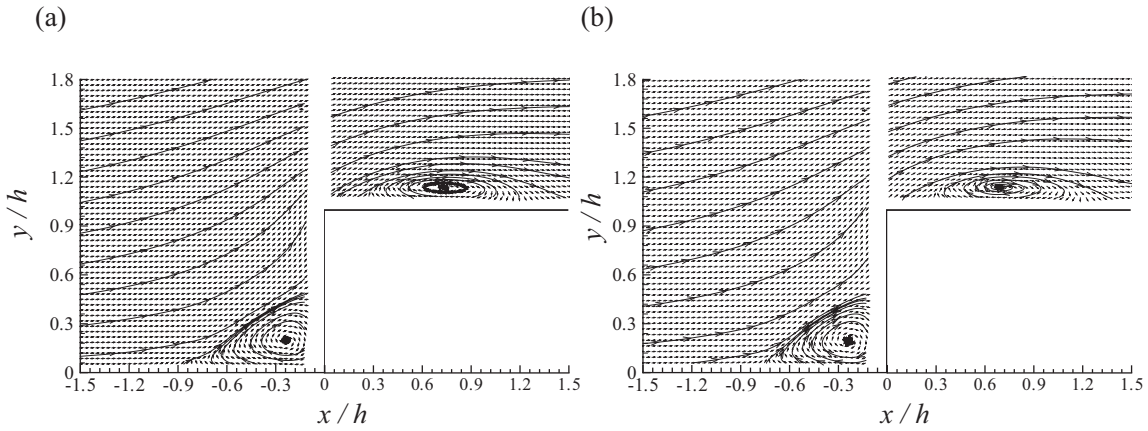

Figure 4.1: Ensemble averaged velocity fields over the smooth FFS at measurement positions of (a) P1, (b) P2. The flow direction is from left to right. The velocity vectors are set to be uniform in lengths for clarity.

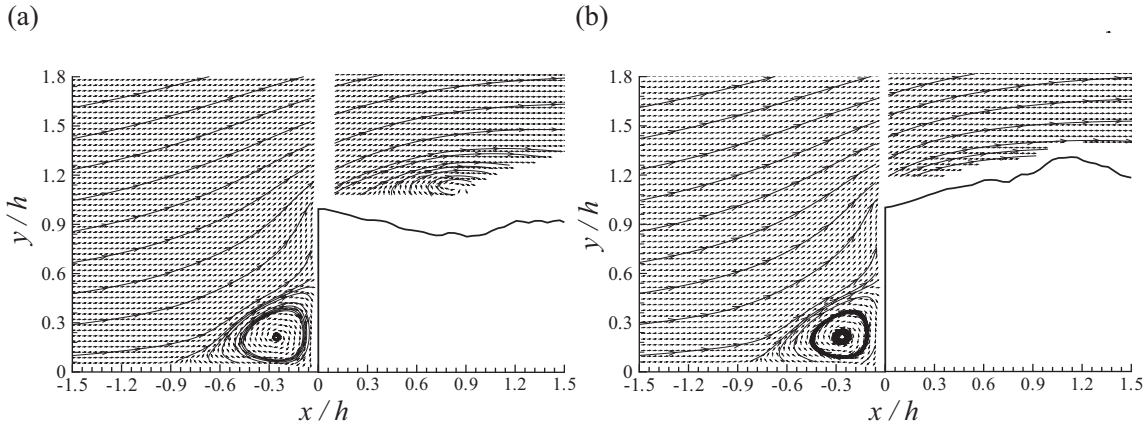

Figure 4.2: Ensemble averaged velocity fields over the rough FFS at measurement positions of (a) P1, (b) P2. The flow direction is from left to right. The velocity vectors are set to be uniform in lengths.

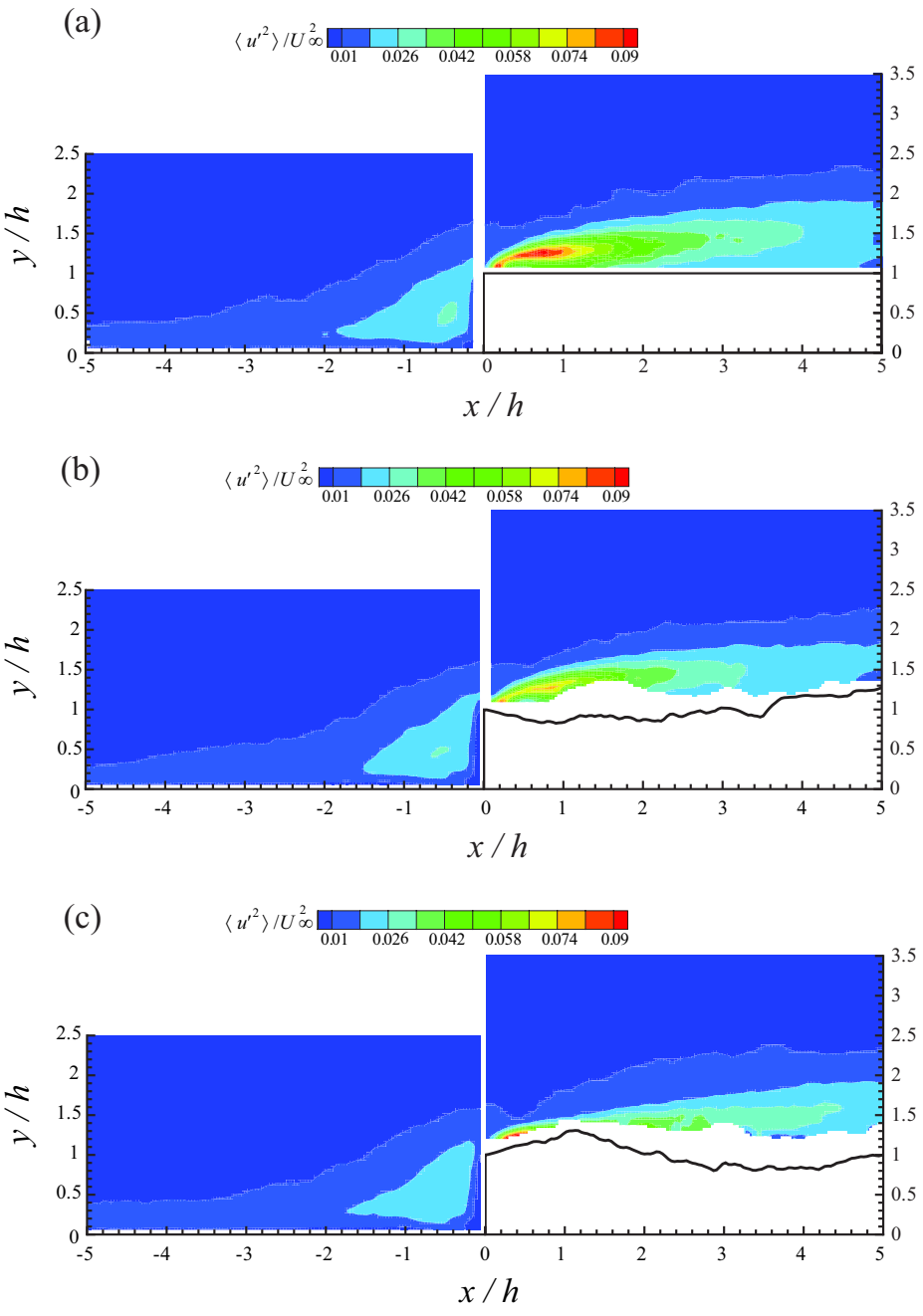

Figure 4.3: Contour of the normalized streamwise Reynolds stress, $\frac{\langle u'^2 \rangle}{U_\infty^2}$, for (a) smooth step, (b) rough step at position P1, (c) rough step at position P2.

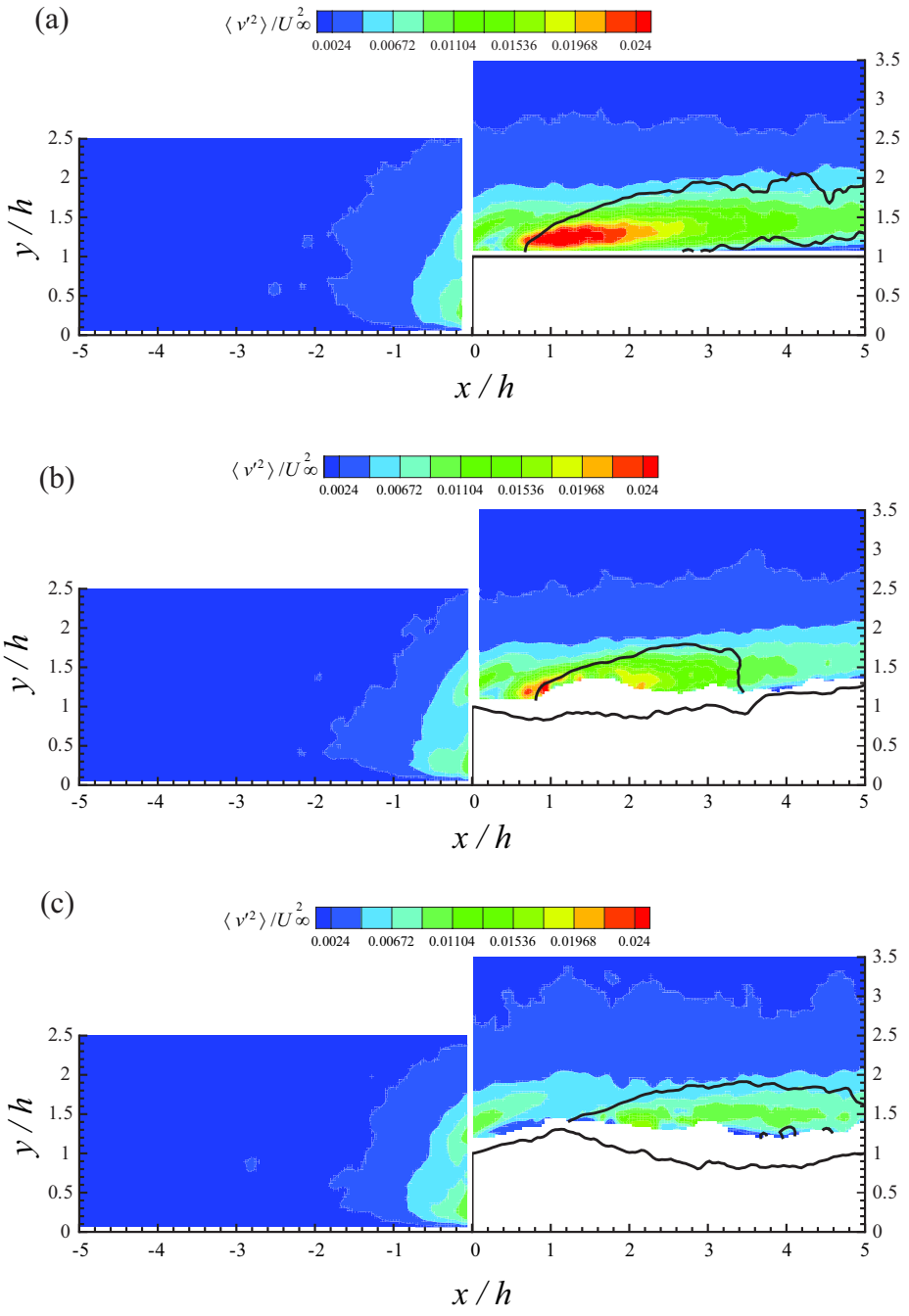

Figure 4.4: Contour of the normalized wall-normal Reynolds stress, $\frac{\langle v'^2 \rangle}{U_\infty^2}$, for (a) smooth step, (b) rough step at position P1, (c) rough step at position P2. Line contour of $V = 0$ is overlaid in the downstream region of the FFS flow. $V < 0$ within the region enclosed by this contour line and $V > 0$ outside of this contour line.

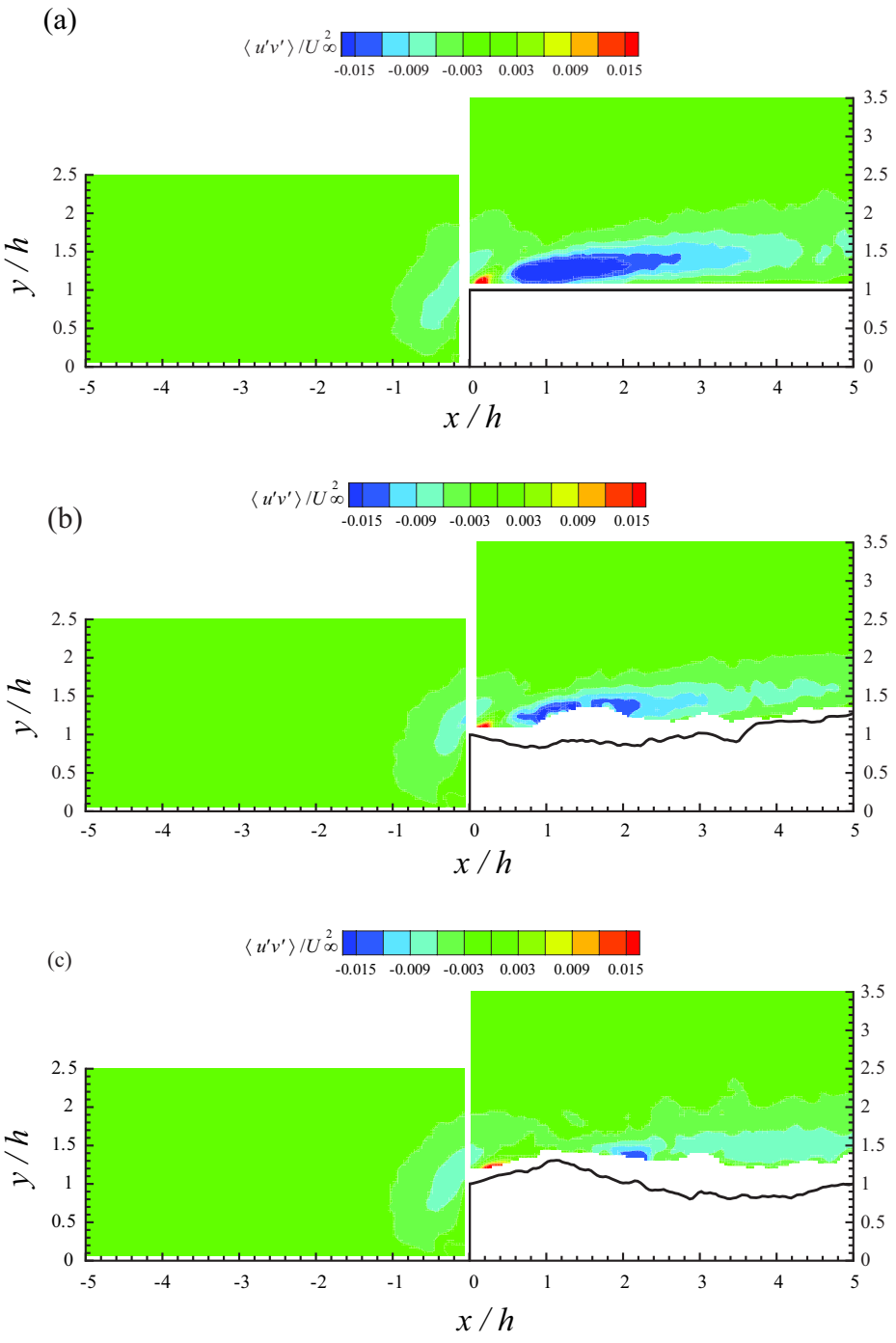

Figure 4.5: Contour of the Reynolds shear stress, $\frac{\langle u'v' \rangle}{U_\infty^2}$, for (a) smooth step, (b) rough step at position P1, (c) rough step at position P2.

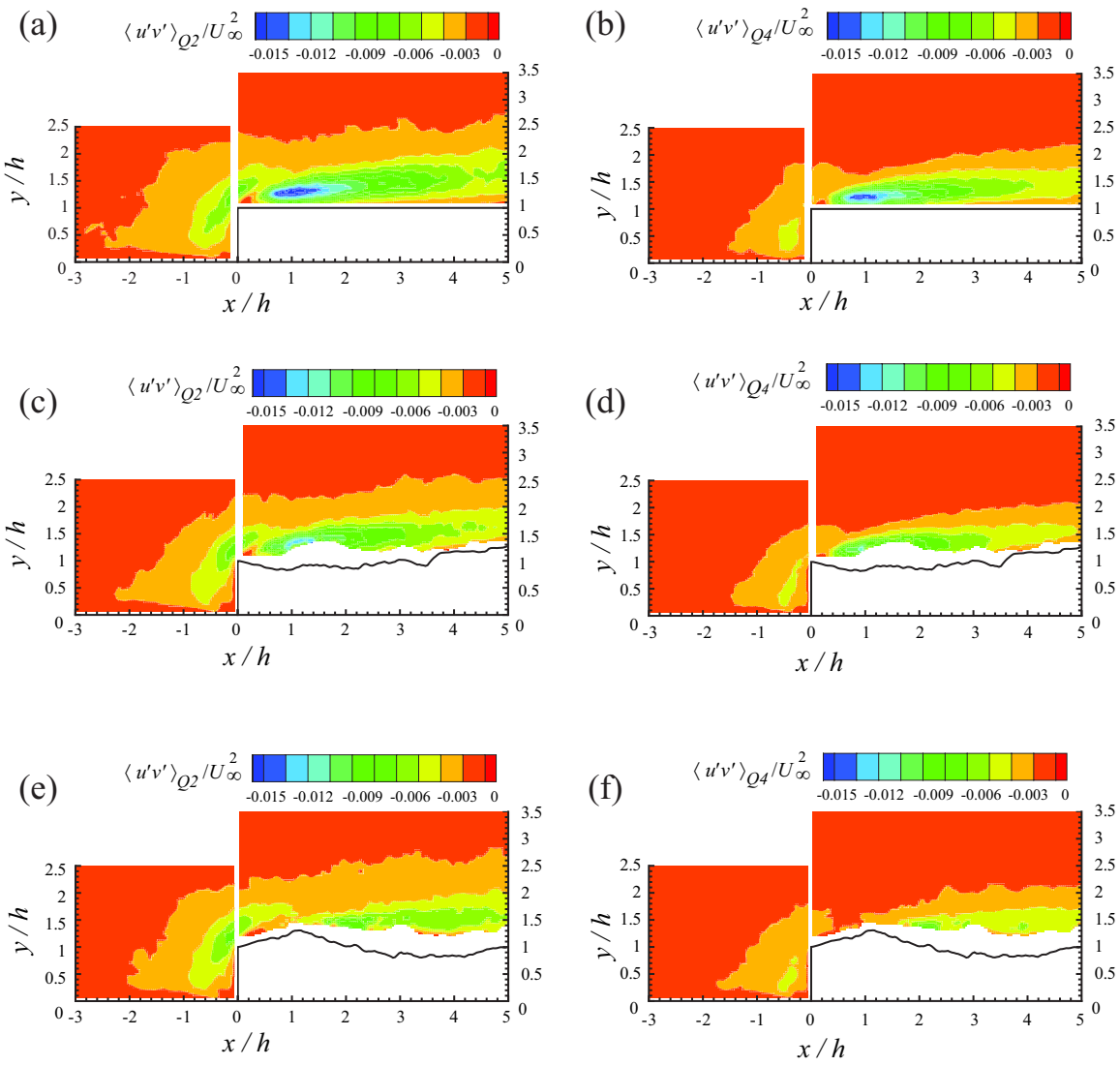

Figure 4.6: Reynolds shear stress contributions for the threshold of $H = 0$ from (a) ejections ($Q2$ event) for the smooth FFS, (b) sweeps ($Q4$ event) for the smooth FFS, (c) ejections for the rough FFS at position P1, (d) sweeps for the rough FFS at position P1, (e) ejections for the rough FFS at position P2, (f) sweeps for the rough FFS at position P2.

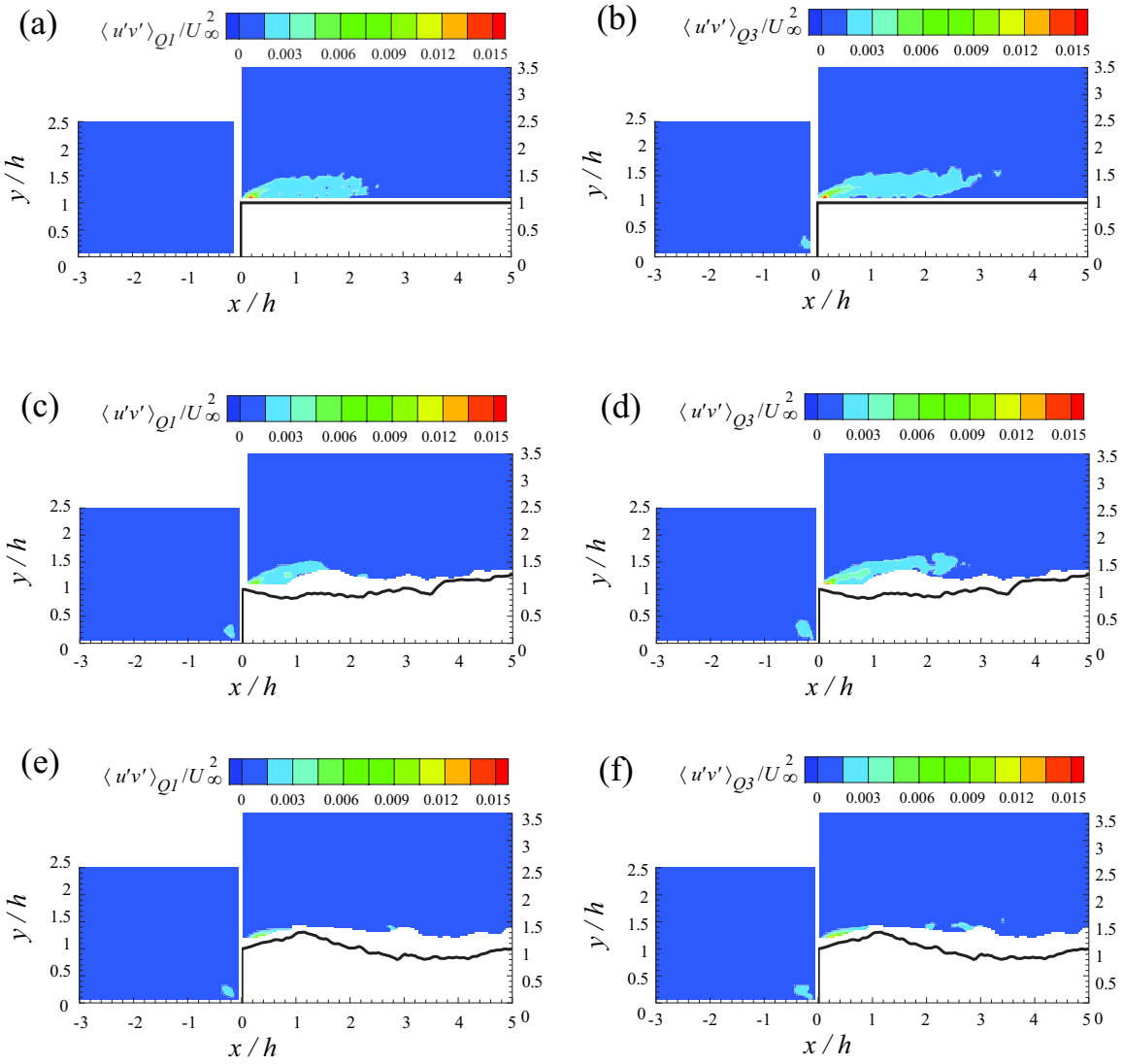

Figure 4.7: Reynolds shear stress contributions for the threshold of $H = 0$ from (a) ejections ($Q1$ event) for the smooth FFS, (b) sweeps ($Q3$ event) for the smooth FFS, (c) ejections for the rough FFS at position P1, (d) sweeps for the rough FFS at position P1, (e) ejections for the rough FFS at position P2, (f) sweeps for the rough FFS at position P2.

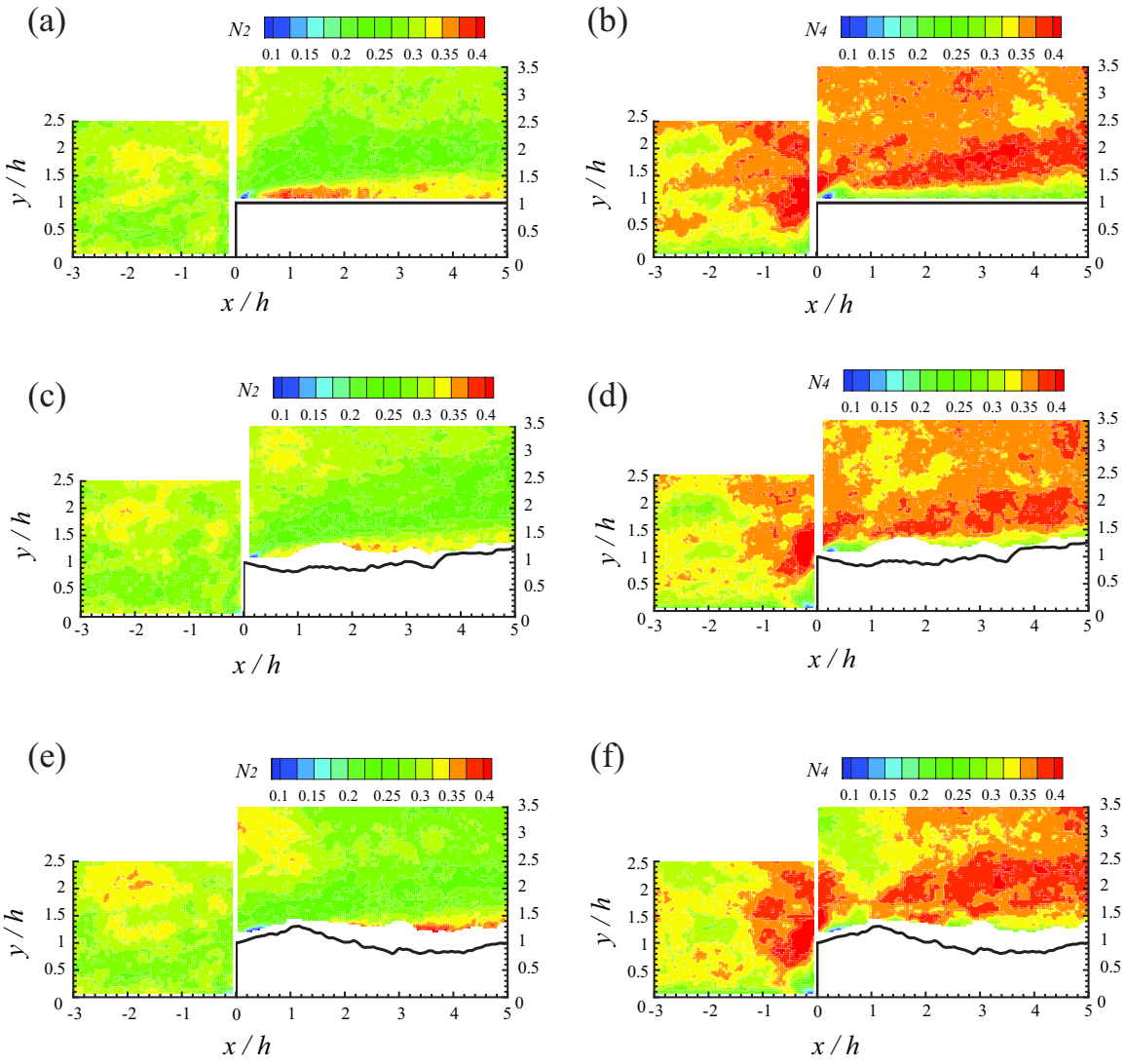

Figure 4.8: Space fractions, for a threshold of $H = 0$, occupied by (a) ejections ($Q2$ event) for the smooth FFS, (b) sweeps ($Q4$ event) for the smooth FFS, (c) ejections for the rough FFS at position P1, (d) sweeps for the rough FFS at position P1, (e) ejections for the rough FFS at position P2, (f) sweeps for the rough FFS at position P2.

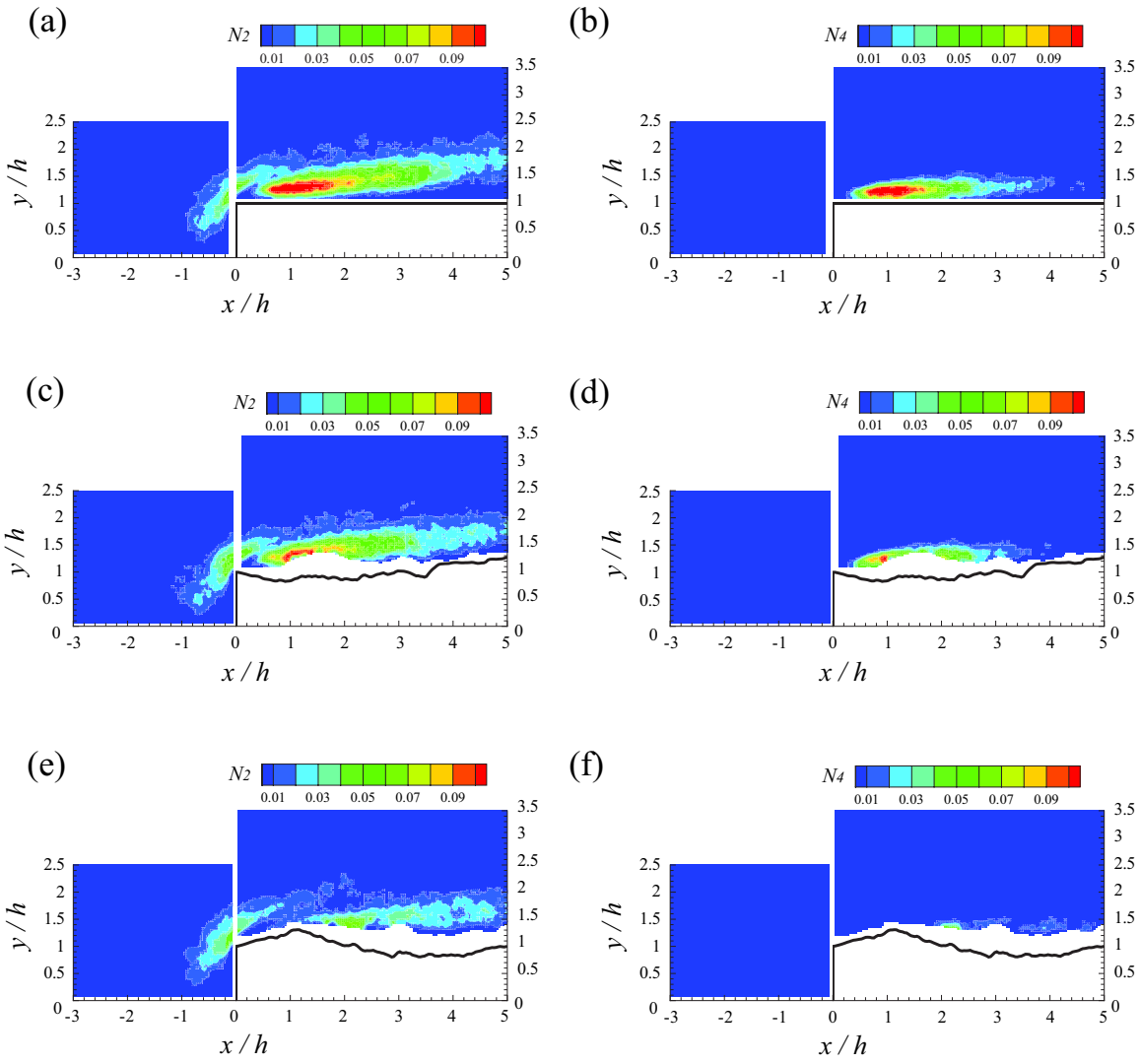

Figure 4.9: Space fractions, for a threshold of $H = 4$, occupied by (a) ejections ($Q2$ event) for the smooth FFS, (b) sweeps ($Q4$ event) for the smooth FFS, (c) ejections for the rough FFS at position P1, (d) sweeps for the rough FFS at position P1, (e) ejections for the rough FFS at position P2, (f) sweeps for the rough FFS at position P2.

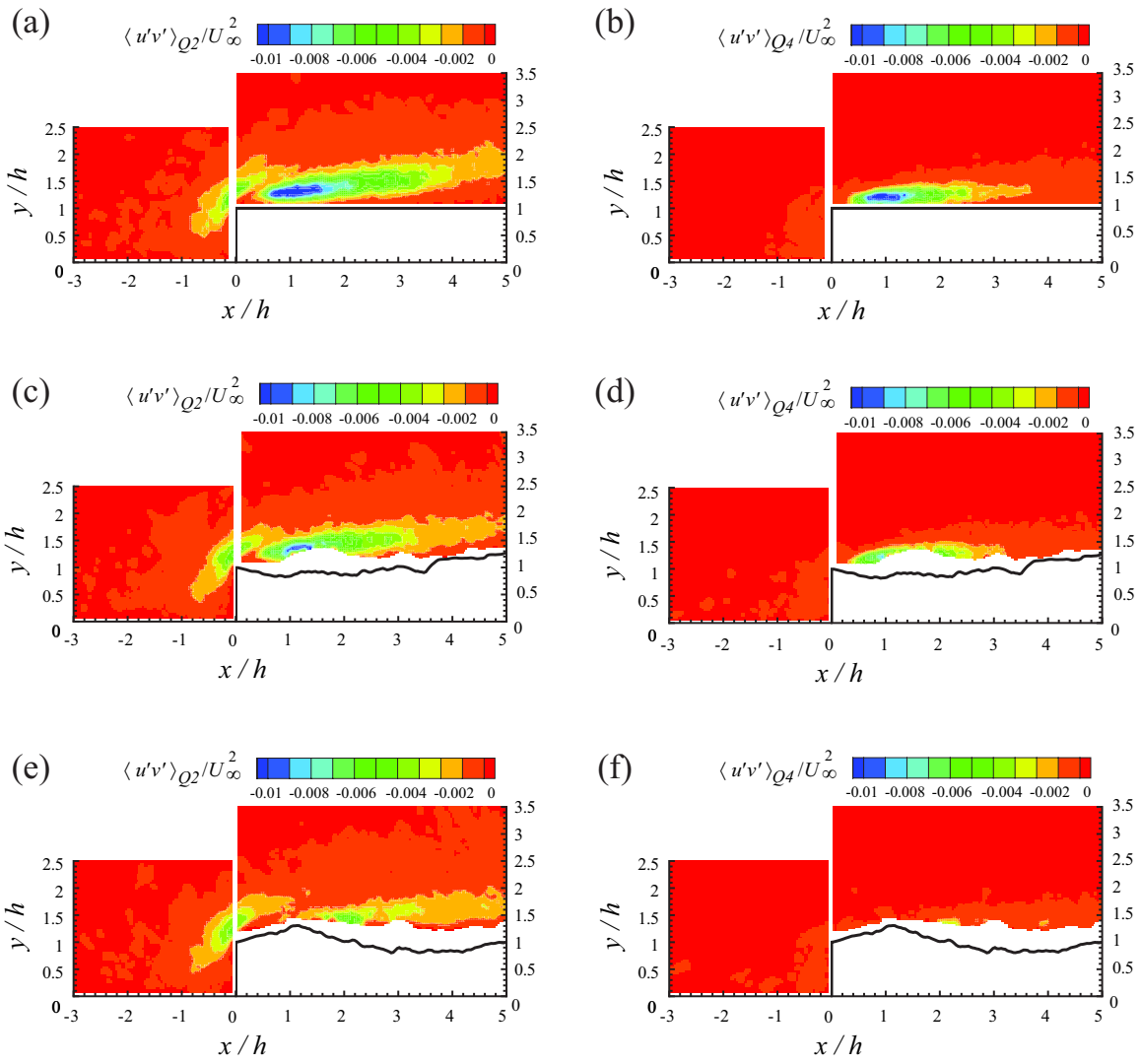

Figure 4.10: Reynolds shear stress contributions for the threshold of $H = 4$ from (a) ejections ($Q2$ event) for the smooth FFS, (b) sweeps ($Q4$ event) for the smooth FFS, (c) ejections for the rough FFS at position P1, (d) sweeps for the rough FFS at position P1, (e) ejections for the rough FFS at position P2, (f) sweeps for the rough FFS at position P2.

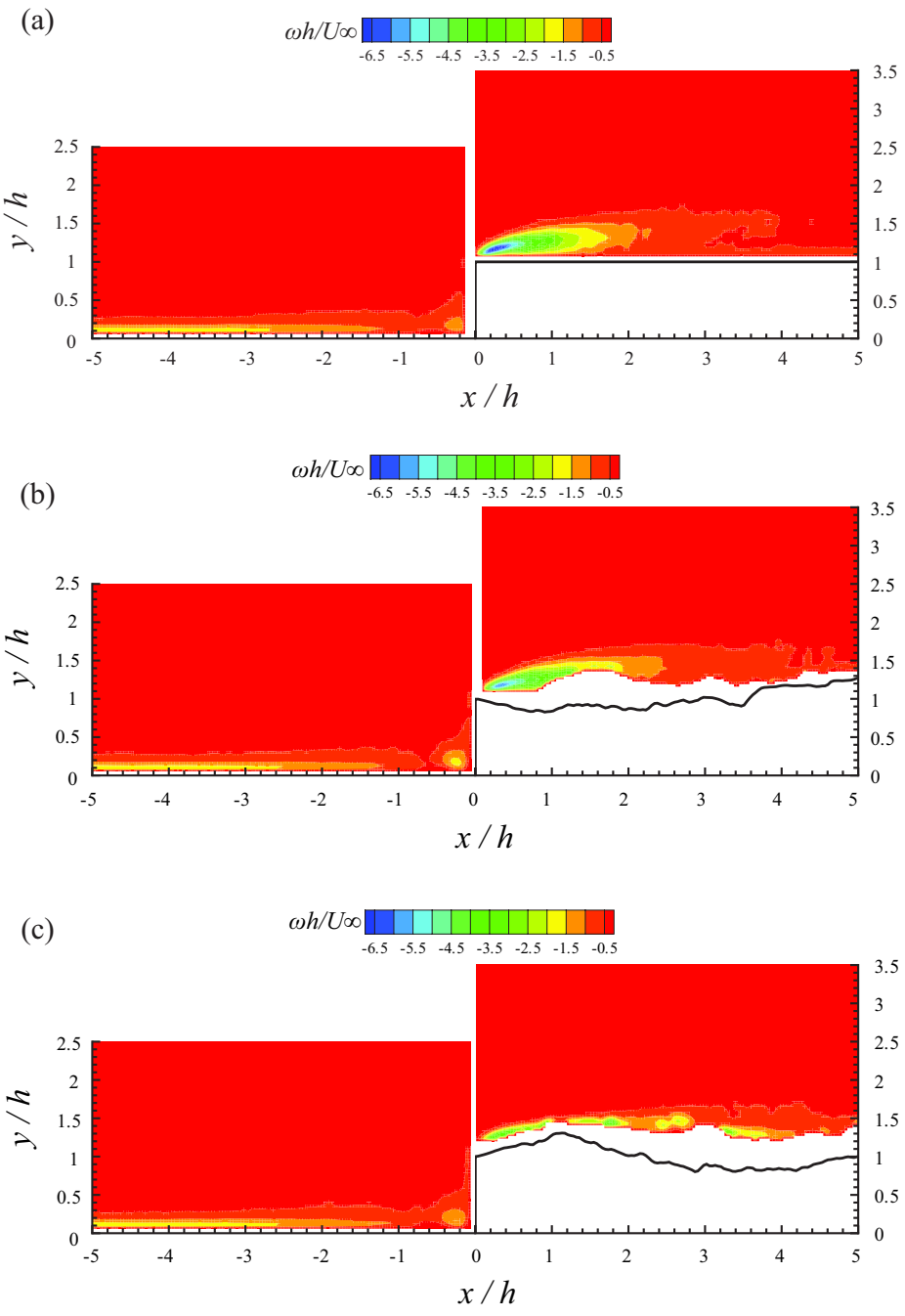

Figure 4.11: Spanwise vorticity for (a) smooth FFS, (b) rough FFS at position P1, (c) rough FFS at position P2.

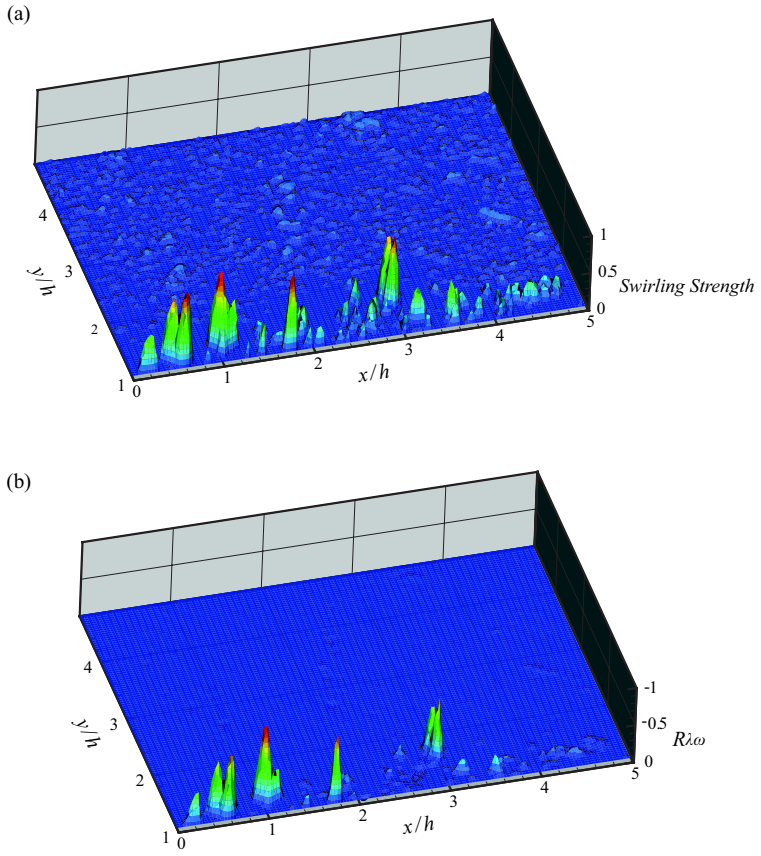

Figure 4.12: (a) A representative instantaneous field of swirling strength, λ_{ci} in the streamwise–wall-normal plane in the downstream region of the smooth step. (b) Field of $R_{\lambda\omega}$ obtained from the same velocity field as in (a). λ_{ci} and $R_{\lambda\omega}$ have been normalized by their respective maximum absolute values.

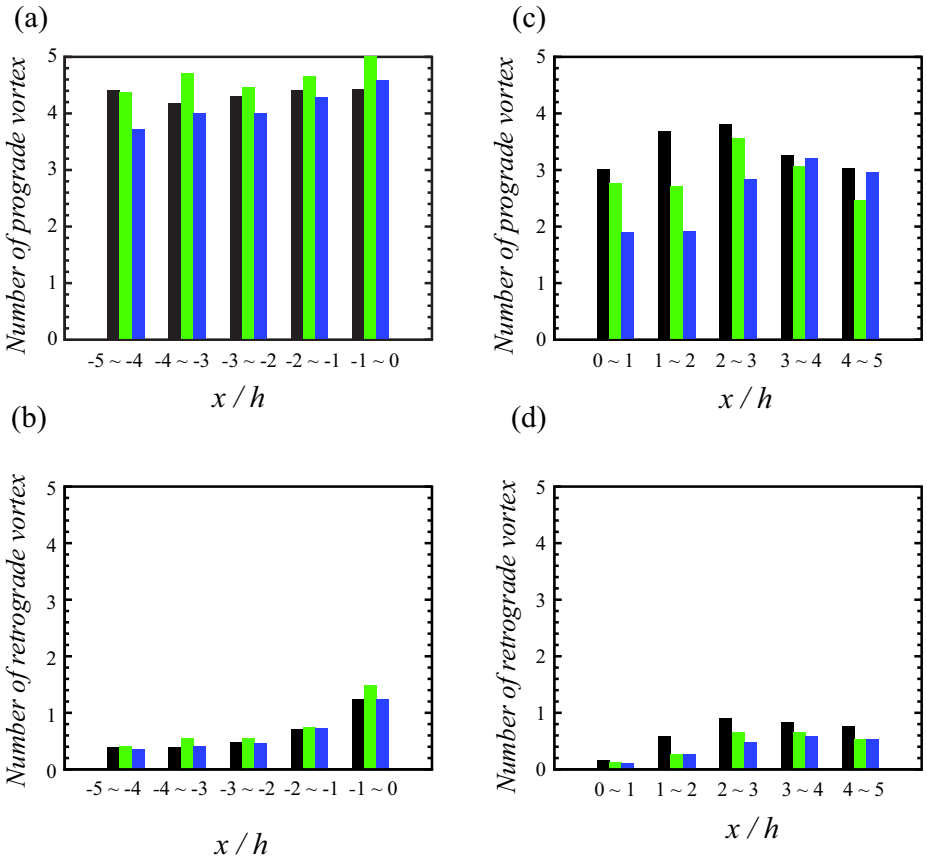

Figure 4.13: Number of spanwise vortices per measurement field. (a) Prograde ($R_{\lambda\omega} < 0$) vortices upstream of the step, (b) retrograde ($R_{\lambda\omega} > 0$) vortices upstream of the step, (c) prograde vortices downstream of the step, (d) retrograde vortices downstream of the step. Black (left) bar is for the smooth step, green (middle) bar is for the rough step at P1, and blue (right) bar is for the rough step at P2.

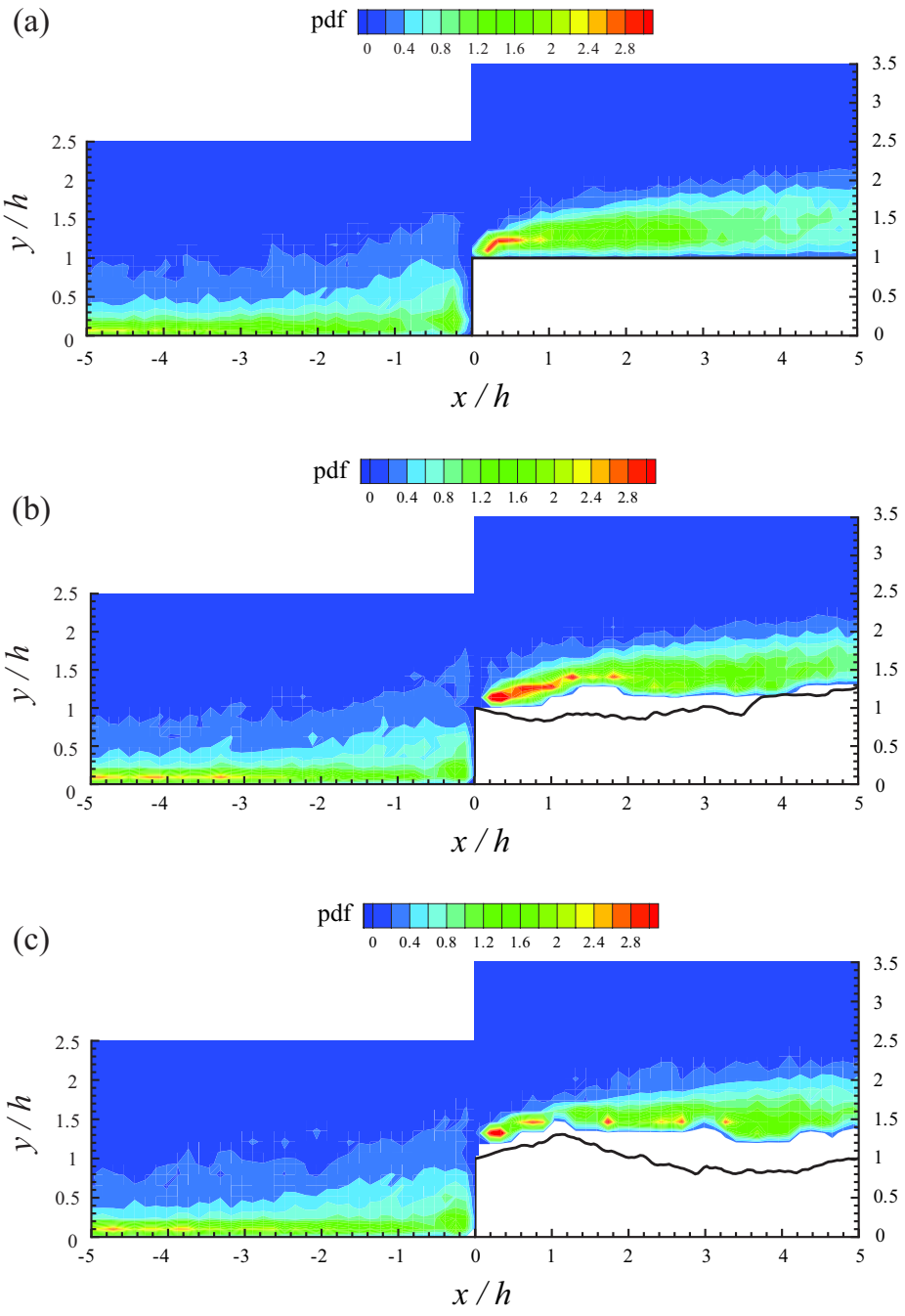

Figure 4.14: Spatial probability distributions of prograde vortices for (a) smooth FFS, (b) rough FFS at position P1, and (c) rough FFS at position P2.

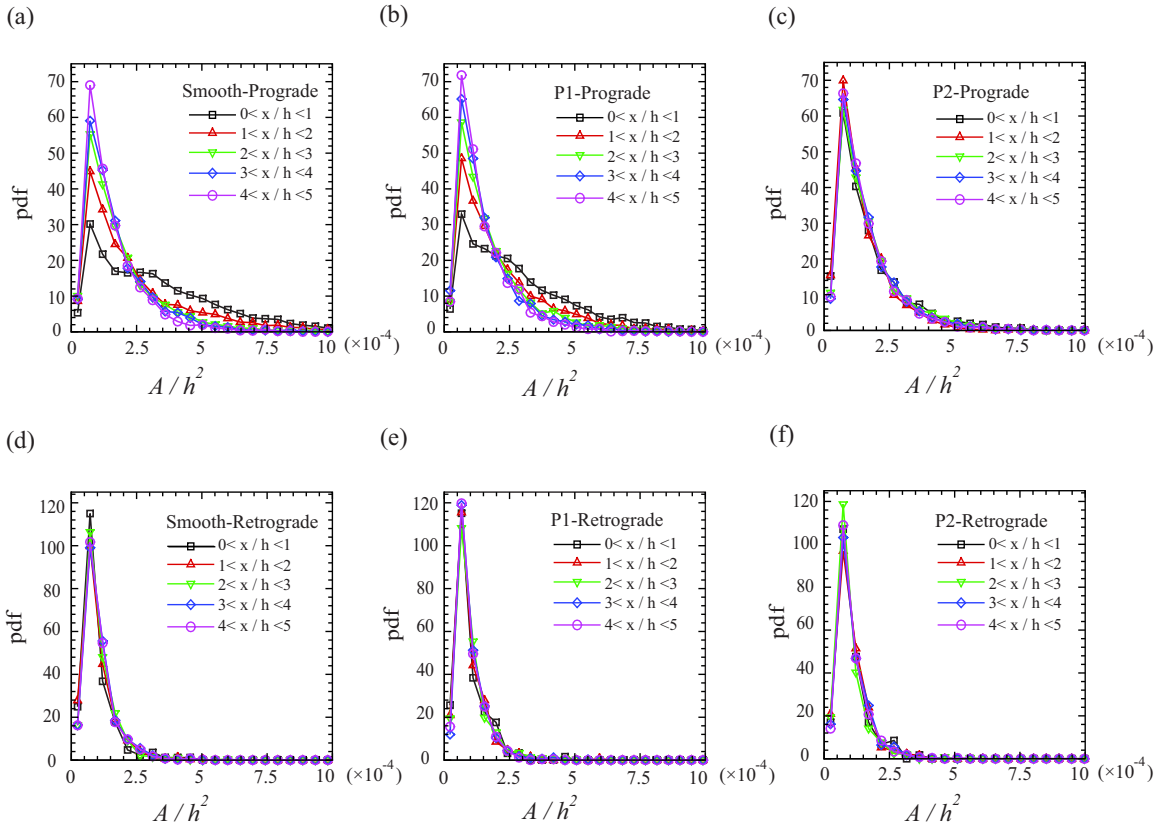

Figure 4.15: Probability density functions of the sizes of the prograde vortices downstream of the (a) smooth step, (b) rough step at P1, and (c) rough step at P2. Probability density functions of the sizes of the retrograde vortices downstream of the (d) smooth step, (e) rough step at P1, and (f) rough step at P2. Every other data is shown for clarity.

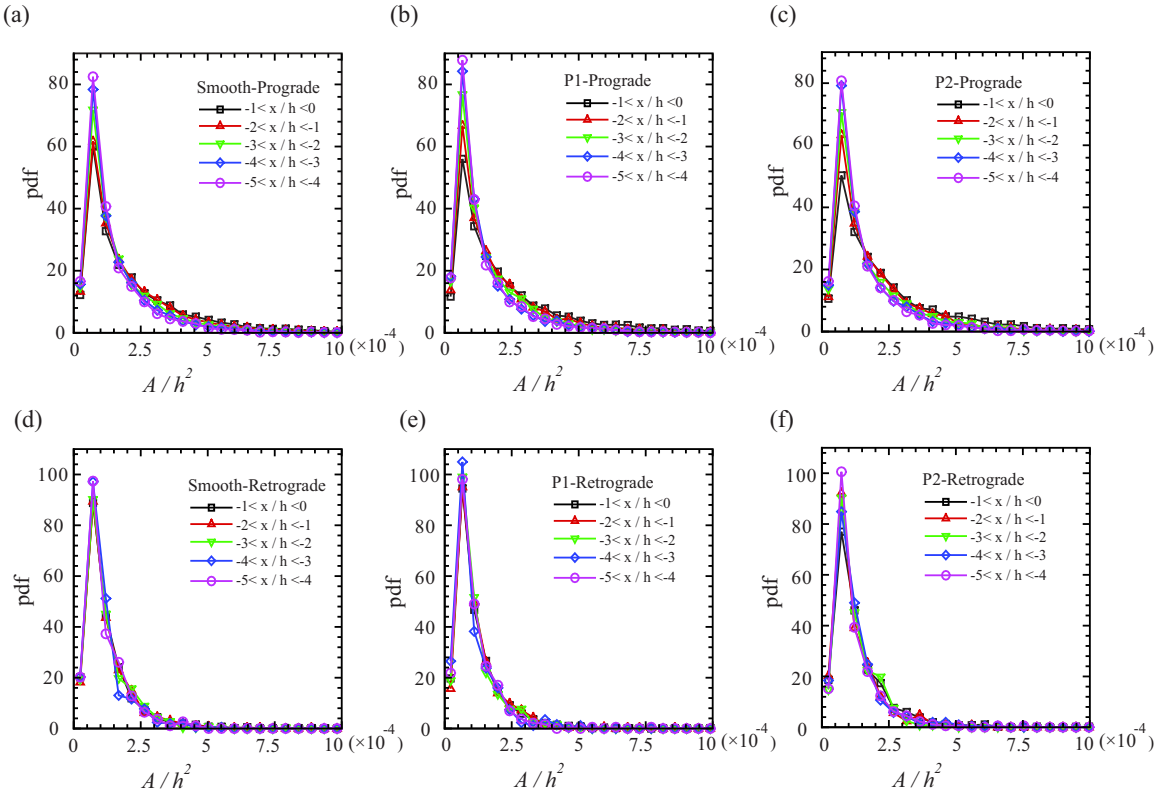

Figure 4.16: Probability density functions of the sizes of the prograde vortices upstream of the (a) smooth step, (b) rough step at P1, and (c) rough step at P2. Probability density functions of the sizes of the retrograde vortices upstream of the (d) smooth step, (e) rough step at P1, and (f) rough step at P2. Every other data is shown for clarity.

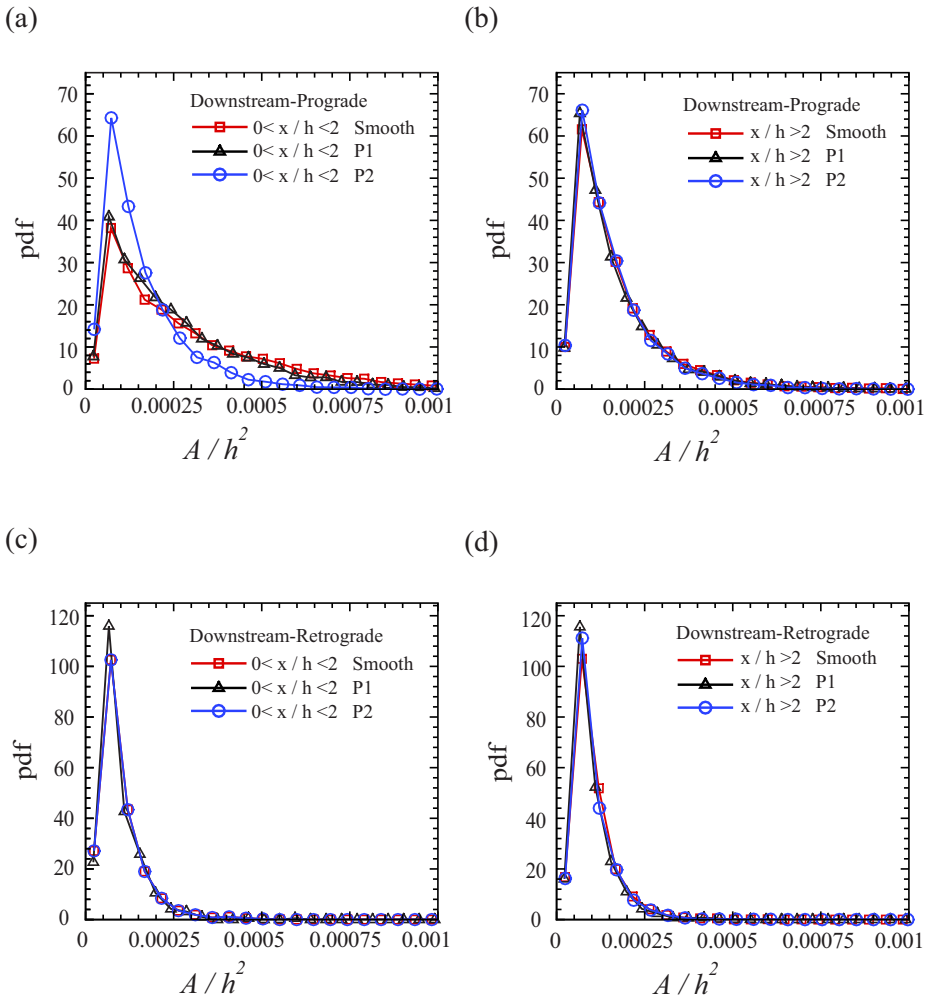

Figure 4.17: Comparison of probability density functions of the sizes of the prograde vortices downstream of the smooth and rough steps for (a) $0 < x/h < 2$ and (b) $x/h > 2$. Comparison of probability density functions of the sizes of the retrograde vortices downstream of the smooth and rough steps for (c) $0 < x/h < 2$ and (d) $x/h > 2$. Every other data is shown for clarity.

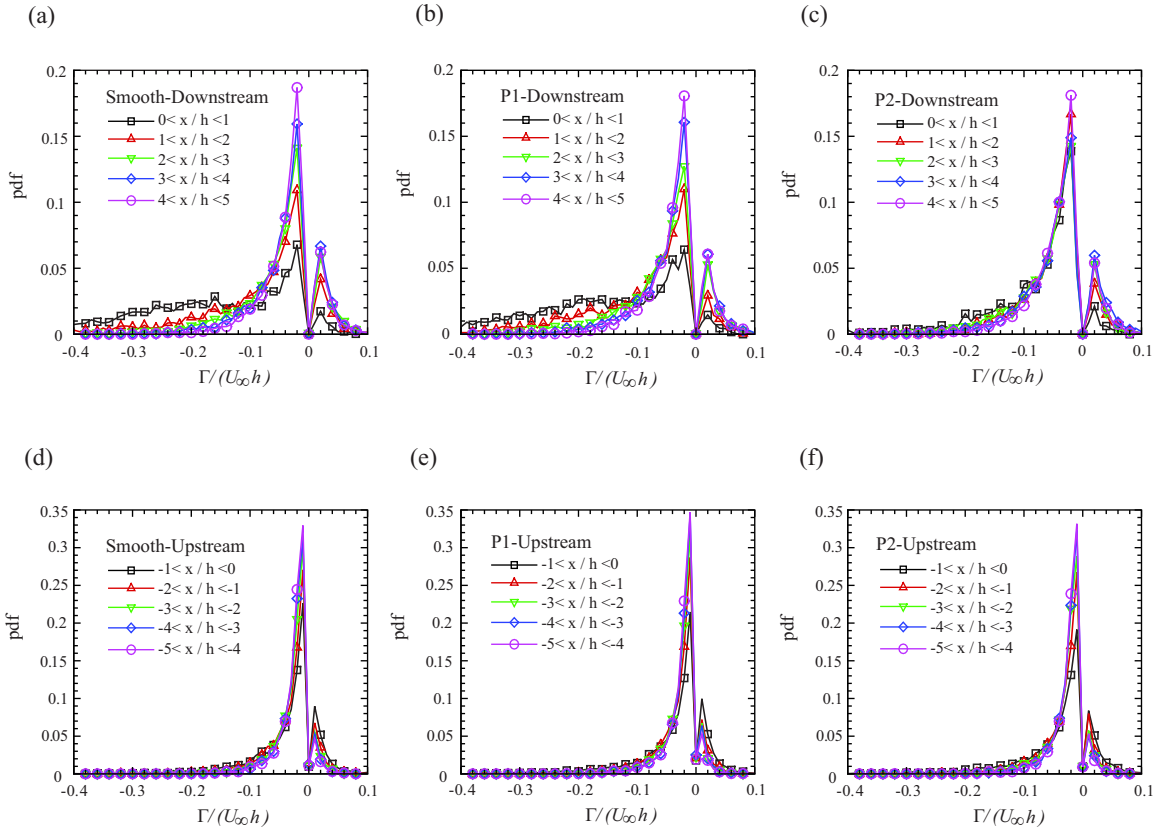

Figure 4.18: Probability density functions of the circulation of the vortices downstream of the (a) smooth step, (b) rough step at P1, and (c) rough step at P2. Probability density functions of the circulation of the vortices upstream of the (d) smooth step, (e) rough step at P1, and (f) rough step at P2. Every other data is shown for clarity.

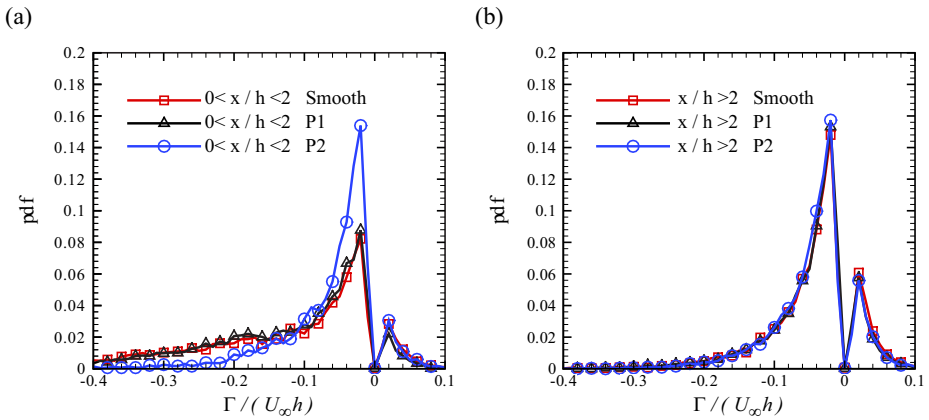

Figure 4.19: Comparison of probability density functions of the circulation of the vortices downstream of the smooth and rough steps for (a)$0 < x/h < 2$ and (b) $x/h > 2$. Every other data is shown for clarity.

Turbulent Boundary Layers Over Coarse Scale Resolution Approximations of the Rough Forward-facing Steps

This chapter presents results concerning the impact of coarse scale resolution approximations at levels A6 and A4 of the full roughness on the forward-facing step turbulent flows. In particular, the mean flow structure, Reynolds normal and shear stresses, quadrant analysis, ensemble averaged spanwise vorticity and the characteristics of the coherent spanwise vortices of the turbulent boundary layers over A6 and A4 steps are compared with those over the original rough step.

5.1 Mean flow structures

Ensemble averaged velocity fields over A6 and A4 at two different measurement positions P1 and P2 are presented in figure 5.1. At very coarse scale approximation of the rough step (A6), the turbulent boundary layer separated both upstream and downstream of the step showing separation bubbles in both recirculation regions as illustrated in figure 5.1 (a) and (b). The mean flow structures are quantitatively similar to those over the smooth step since the large scale roughness have very small roughness heights. On the other hand, at approximation level A4, the roughness profile at position P2 produces a positive slope that is similar to that in the full roughness. This positive slope may create a favorable pressure

gradient that is comparable to the one for the full surface and is strong enough to prevent the flow separation (figure 5.1 (d)). Although the negative slope of the full roughness is also reproduced well by step approximation A4 at position P1, the adverse pressure gradient incurred will not prevent the flow being separated by the step as expected from observation made from figure 4.2 (a). The mean flow structures over A4 are therefore observed to be qualitatively similar to those over the full-roughness step. However, a very coarse approximation such as A6 fails to produce a qualitatively similar mean flow structures as those in the full roughness step.

The characteristics of the upstream recirculation region such as the separation and reattachment points as well as the bubble centers are summarized in table 5.1. Note that the separation and reattachment points on the vertical wall of the step are measured only at the grid point closest to the solid surfaces which is different for different cases and therefore these values can only be compared loosely and will be smaller than the true values. The characteristics of the upstream recirculation region are invariant to different scales of the roughness on the step's top surface. Within measurement uncertainties, the locations of separation point, reattachment points and bubble center for the rough steps at scale levels of A6 and A4 are also about the same as those for the smooth step and the rough step with full roughness. However, the downstream recirculation regions are found to be sensitive to roughness scales and specific roughness topographies. For the coarse step approximation A6, table 5.2 shows that the reattachment length, X_r, at position P2 is almost 30% larger than that at P1 although the closest grid point is even further away from the step's top surface at P2. In addition, although the streamwise (x) locations of the downstream bubble center are about the same within measurement uncertainty, the wall-normal (y) location at P2 is significantly ($\sim$ 11%) higher than that at P1 as illustrated in table 5.2. Even though step A6 is a little higher at position P2 than P1, the bubble's center at P2 is still noticeably further away from the step's top surface as can be observed in figures 5.1 (a) and (b). Therefore, it is seen that the downstream recirculation region is distorted by the waviness

Table 5.1: Locations of the separation point, reattachment position on the vertical wall of the step, and the bubble center in the upstream recirculation region in the turbulent boundary layers over FFSs at scale resolutions of A6 and A4.

	Separation Point	Reattachment Position	Bubble Center
A6 at P1	$x = -0.67 \pm 0.10h$	$y = 0.52 \pm 0.03h$	$(-0.26 \pm 0.02h, 0.21 \pm 0.02h)$
A6 at P2	$x = -0.77 \pm 0.10h$	$y = 0.55 \pm 0.03h$	$(-0.28 \pm 0.02h, 0.21 \pm 0.02h)$
A4 at P1	$x = -0.63 \pm 0.10h$	$y = 0.49 \pm 0.03h$	$(-0.24 \pm 0.02h, 0.20 \pm 0.02h)$
A4 at P2	$x = -0.70 \pm 0.10h$	$y = 0.54 \pm 0.03h$	$(-0.27 \pm 0.02h, 0.20 \pm 0.02h)$

Table 5.2: Reattachment length, X_r, and locations of the bubble center in the downstream recirculation region on top of the forward-facing steps at scale resolutions of A6 and A4.

	Reattachment Length X_r	Bubble Center
A6 at P1	$0.99 \pm 0.03h$	$(0.77 \pm 0.05h, 1.15 \pm 0.02h)$
A6 at P2	$1.27 \pm 0.03h$	$(0.72 \pm 0.05h, 1.28 \pm 0.02h)$
A4 at P1	———	$(0.75 \pm 0.05h, 1.08 \pm 0.02h)$
A4 at P2	———	———

of the large-scale roughness such that recirculation bubble becomes smaller and closer to the surface where the step's height is lower. With the inclusion of finer scales of the roughness as in step A4, the downstream recirculation can be dramatically changed to be highly three-dimensional as seen in figure 5.1 where the bubble disappears at position P2. The finest-scale roughness included in the full-surface step appear to only fine-tune the characteristics of the mean flow structures such as the streamwise location of the separation bubble at position P1.

5.2 Reynolds stresses

The streamwise Reynolds normal stress, $\frac{\langle u'^2 \rangle}{U_\infty^2}$, over A6 and A4 at measurement positions P1 and P2 are presented in figure 5.2. $\frac{\langle u'^2 \rangle}{U_\infty^2}$ for the step of full rough surface is also included for comparison. For step A6 with large-scale roughness, large values of streamwise Reynolds normal stress comparable to that over the smooth step is generated in the downstream recirculation region. However, the distribution of $\langle u'^2 \rangle$ is not observed to be the same

between measurement positions of P1 and P2 revealing a three-dimensional feature of the separated turbulent flow. As finer scale roughness is included in A4, $\langle u'^2 \rangle$ is significantly decreased in the downstream recirculation region, especially at P2 where the bubble is annihilated by the positive roughness slope. While $\langle u'^2 \rangle$ is quite similar between step A4 and full surface step at position P1, it is still quite different between these two steps at position P2, particularly within $1h$ downstream of the step. This is probably because the roughness profile of A4 at P2 is a little different from that of full surface in that A4 starts as a plateau and gradually produces a positive slope while the full surface starts up with a strong positive slope at position P2.

Wall-normal Reynolds normal stress, $\frac{\langle v'^2 \rangle}{U_\infty^2}$, over steps of A6, A4 and full surface at measurement positions P1 and P2 are presented in figure 5.3. For step A6, a large region of significant $\langle v'^2 \rangle$ exists downstream of the step at both P1 and P2, which is similar to that over the smooth step. However, $\langle v'^2 \rangle$ in this region at P1 is weaker than that at position P2 probably because the large-scale roughness profile at P1 gradually goes up producing a slightly favorable pressure gradient while the roughness profile at P2 gradually goes down. When finer roughness scales are included in step A4, $\langle v'^2 \rangle$ is dramatically reduced at position P2, especially around $x = 1h$ compared to step A6. On the other hand, the difference of $\langle v'^2 \rangle$ between A6 and A4 at position P1 is not as obvious as at P2. A comparison between steps of A4 and full surface reveals that $\langle v'^2 \rangle$ is further decreased significantly around the local roughness peak at $x = 1h$ at position P2 by the even finer roughness scales included in the full surface. At position P1, the finer scale roughness excluded in A4 also slightly reduces $\langle v'^2 \rangle$.

Reynolds shear stress, $\frac{\langle u'v' \rangle}{U_\infty^2}$, over steps of different scale resolutions at measurement positions P1 and P2 are shown in figure 5.4. Similar to the smooth step case, a large region of strong $\langle u'v' \rangle$ is produced downstream of the steps at A6. Due to the slightly different slope of the large-scale roughness profiles between P1 and P2, $\langle u'v' \rangle$ is a little stronger and larger in extent at position P2. At position P1, the inclusion of finer scale roughness in

A4 does not noticeably alter the distribution of $\langle u'v' \rangle$ compared with that of A6 although the negative slope of the roughness profile immediately downstream of step A4 is much stronger than the slope of A6. At position P2, the extent of strong Reynolds shear stress is reduced by the smaller scale roughness included in A4 even though the peak value of $\langle u'v' \rangle$ does not appear to be altered appreciably. The inclusion of even finer scale roughness from A4 to full surface further reduces Reynolds shear stress, but much more significantly at position P2 than at P1.

5.3 Quadrant analysis

Reynolds shear stress contributions from ejections and sweeps for a threshold of $H = 0$ are presented in figures 5.5 and 5.6, respectively, for steps of A6, A4 and full surface at both P1 and P2. It is observed that ejections always contribute more to the Reynolds shear stress than sweeps irrespective of the roughness length scales. Downstream of step A6 with coarse scale roughness, both ejections and sweeps contribute more at P2 than P1 resulting a stronger and larger region of total Reynolds shear stress at P2 as seen in figure 5.4. At position P1, $\langle u'v' \rangle$ contributions from either ejections or sweeps are very similar between A6 and A4 while these contributions are slightly decreased from A4 to full surface. In contrast, dramatic changes occur at position P2 in $\langle u'v' \rangle$ contributions. At P2, the inclusion of smaller scale roughness from A6 to A4 and to full surface significantly decreases the contributions to Reynolds shear stress from both ejections and sweeps. It is through the inhibition of the contribution from ejections and sweeps that the total Reynolds shear stress is dramatically reduced by the finer scale roughness at P2, especially around $x = 1h$.

The space fractions occupied by ejections and sweeps are shown in figures 5.7 and 5.8, respectively, for a threshold of $H = 0$. Irrespective of the roughness length scales, ejections are found to occur more often close to the top surface of the step while, on the contrary, sweeps occupy more space further away from the step's top surface. When finer

scale roughness is added to the surface topography, the number of occurrences of ejections is reduced at both P1 and P2, most noticeably in the region close to the step's top surface, as seen in figure 5.7. However, figure 5.8 shows that the space fractions of sweeps do not appear to be very much different for steps with different roughness length scales for $H = 0$.

Figures 5.9 and 5.10 present the Reynolds shear stress contributions from ejections and sweeps, respectively, for a threshold of $H = 4$ which means only very strong $Q2$ and $Q4$ events are included. At position P1 (figure 5.9 (a), (c) and (e)), the contributions from strong ejections are quite similar between step A6 and A4 while peak values of ejection contributions are slightly higher for step A4 than step of full surface. At measurement position P2 (figure 5.9 (b), (d) and (f)), $\langle u'v' \rangle$ contributions from strong ejections are decreased successively by the inclusion of finer roughness scales from step A6 to A4 and to full surface. Figure 5.10 shows that the contributions from strong sweeps are less than those from strong ejections regardless of the roughness length scales. $\langle u'v' \rangle$ contributions from strong sweeps are not much different between steps of different roughness length scales at position P1 (figure 5.10 (a), (c) and (e)), albeit the peak values at A4 are slightly higher. At position P2 (figure 5.10 (b), (d) and (f)), the trend of the Reynolds shear stress contributions from strong sweeps is the same as contributions from strong ejections, i.e., less contributions are resulted from strong ejections when finer scales of roughness are included in the surface topography of the step. In fact, the difference in $\langle u'v' \rangle$ contributions from over steps of different roughness scale resolutions is caused by the difference in their number of occurrences as shown in figures 5.11 and 5.12 which present the space fractions occupied by strong ejections and sweeps, respectively.

5.4 Spanwise vorticity

The ensemble averaged spanwise vorticity at both measurement positions P1 and P2 over steps of A6, A4 and full surface are presented in figure 5.13. The three-dimensionality

of the recirculation region downstream of the step A6 with large-scale roughness is also revealed from the slightly different vorticity distribution as shown in figures 5.13 (a) and (b). At measurement position P1 (figures 5.13 (a), (c) and (e)), the finer length scales of roughness in A4 do not appear to reduce the peak vorticity downstream of the step compared to that for step A6. However, the peak vorticity for step of full surface is slightly weaker than that for step A4 indicating that the small-scale roughness excluded in step A4 slightly damps the strength of the shear layer. At position P2 (figures 5.13 (b), (d) and (f)), the peak vorticity in the downstream recirculation region is successively decreased by the fine scale roughness. The streamwise spatial extent of the shear layer indicated by strong vorticty within $2h$ downstream of the step is also observed to be reduced by the small roughness scales. The generation of a stronger vorticity at step A4 than that at step of full surface is probably because its roughness profile immediately after the edge of step A4 possesses a small plateau region.

5.5 Characteristics of spanwise vortices

The number of both prograde and retrograde spanwise vortices per measurement field at an interval of $1h$ in the streamwise direction at position P1 for steps of A6, A4, and full surface is presented in figure 5.14. It is observed that at both upstream and downstream of the steps, the maximum difference in the number of both prograde and retrograde spanwise vortices between steps of different scale resolutions along the streamwise direction is about 20%, illustrating that the vortex numbers are quite invariant to the roughness length scales at position P1. Figure 5.15 shows the prograde and retrograde spanwise vortex numbers both upstream and downstream of the steps of A6, A4 and full surface at measurement position P2. At this position, the most obvious difference is in the number of prograde vortices downstream of the steps (figure 5.15 (b)). Within $1h$ downstream of the steps, approximately 50% more prograde vortices are found over step A6 and about 30% more

prograde vortices exist over step A4 when compared with the step of full surface. Between $1h$ and $2h$ downstream of the steps, there are almost twice many prograde vortices over A6 as those over step of full surface while more than 50% prograde vortices are observed over step A4 than over step of full surface. Further downstream of the steps at P2, the number of prograde vortices falls within 17% between these steps of different length scales.

The spacial probability distributions of prograde vortices for steps A6, A4 and of full surface are presented in figure 5.16. Compared with the cases of step A4 and full surface, the prograde vortices downstream of step A6 at both measurement positions are more concentrated closer to the step's front. At P1, the spatial distributions of prograde vortices downstream of step A4 and full surface are quite similar showing very little effect of the finer roughness scales excluded in A4 at this position where the roughness profile possesses a leading negative slope. However, the finer roughness scales excluded in A4 at position P2 appear to play a more noticeable impact on the prograde vortices' spatial distributions. A more scattered spatial distribution is resulted by including these fine length scales of the roughness for full surface at P2.

Figure 5.17 illustrates a comparison of the probability density functions of the sizes of the prograde vortices downstream of the steps of different roughness length scales. Figure 5.17 (a) and (b) show that the sizes of the prograde vortices have the same distributions along the streamwise direction at position P1 irrespective of the roughness length scales of the steps. In contrast, at position P2, significant differences exist in the pdf functions of the sizes of the prograde vortices within $2h$ downstream of the step as shown in figure 5.17 (c). As finer roughness scales are included in the surface topography, fewer large prograde vortices are observed within $2h$ downstream of the step. In addition, the difference in PDF between A6 and A4 is observed to be smaller than the difference between A4 and full surface. As shown in figure 5.17 (d), the size distributions become insensitive to the roughness length scales beyond $2h$ downstream of the step. Nevertheless, the PDF functions of the prograde vortices at both positions are found to peak at the same size

irrespective of step's roughness length scales.

A comparison of probability density functions of the circulation of both prograde and retrograde spanwise vortices downstream of the steps of A6, A4, and full surface is presented in figure 5.18. It is observed that only the circulation pdf function for the prograde vortices at position P2 within $x < 2h$ is affected by the different roughness length scales, as shown in figure 5.18 (c). As finer scales of roughness are included in the surface topography, the circulation of the prograde vortices within $2h$ downstream of the step becomes smaller.

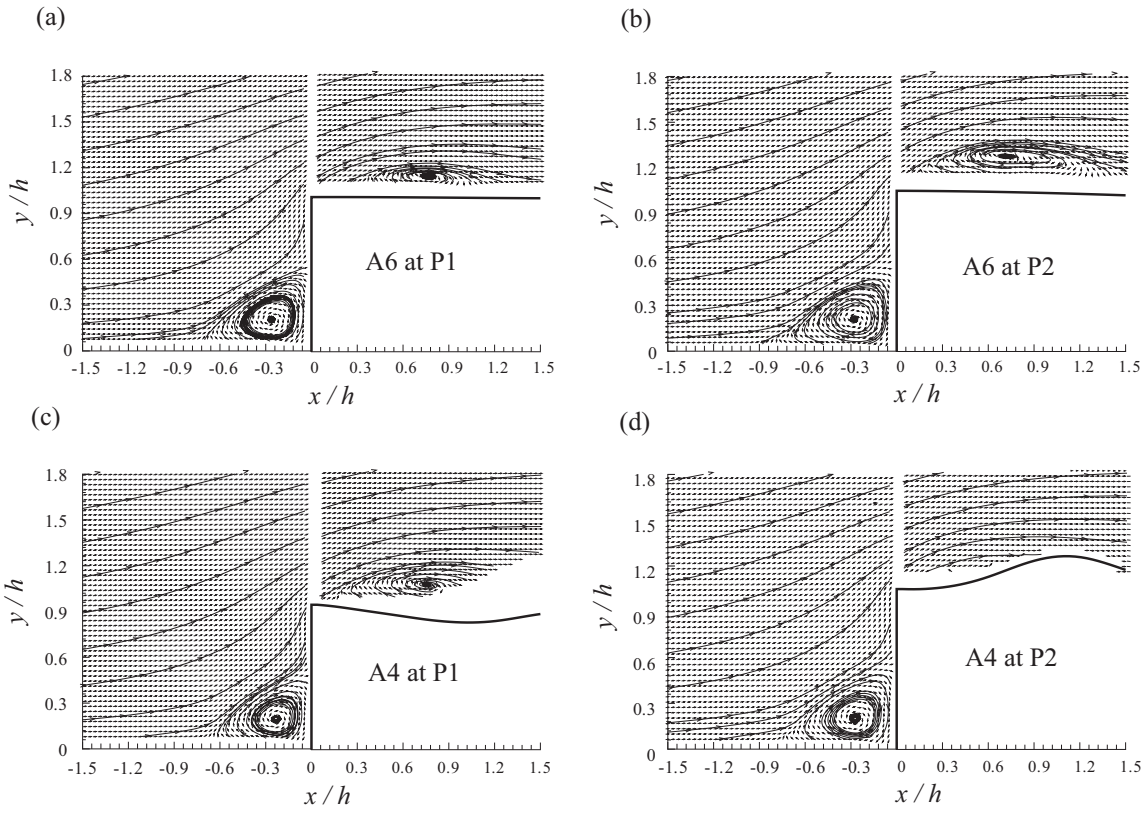

Figure 5.1: Ensemble averaged velocity fields over approximations of the rough forward-facing steps at different measurement positions. (a) A6 at position P1,; (b) A6 at position P2; (c) A4 at position P1; and (d) A4 at position P2. The flow direction is from left to right. The velocity vectors are set to be uniform in lengths for clarity.

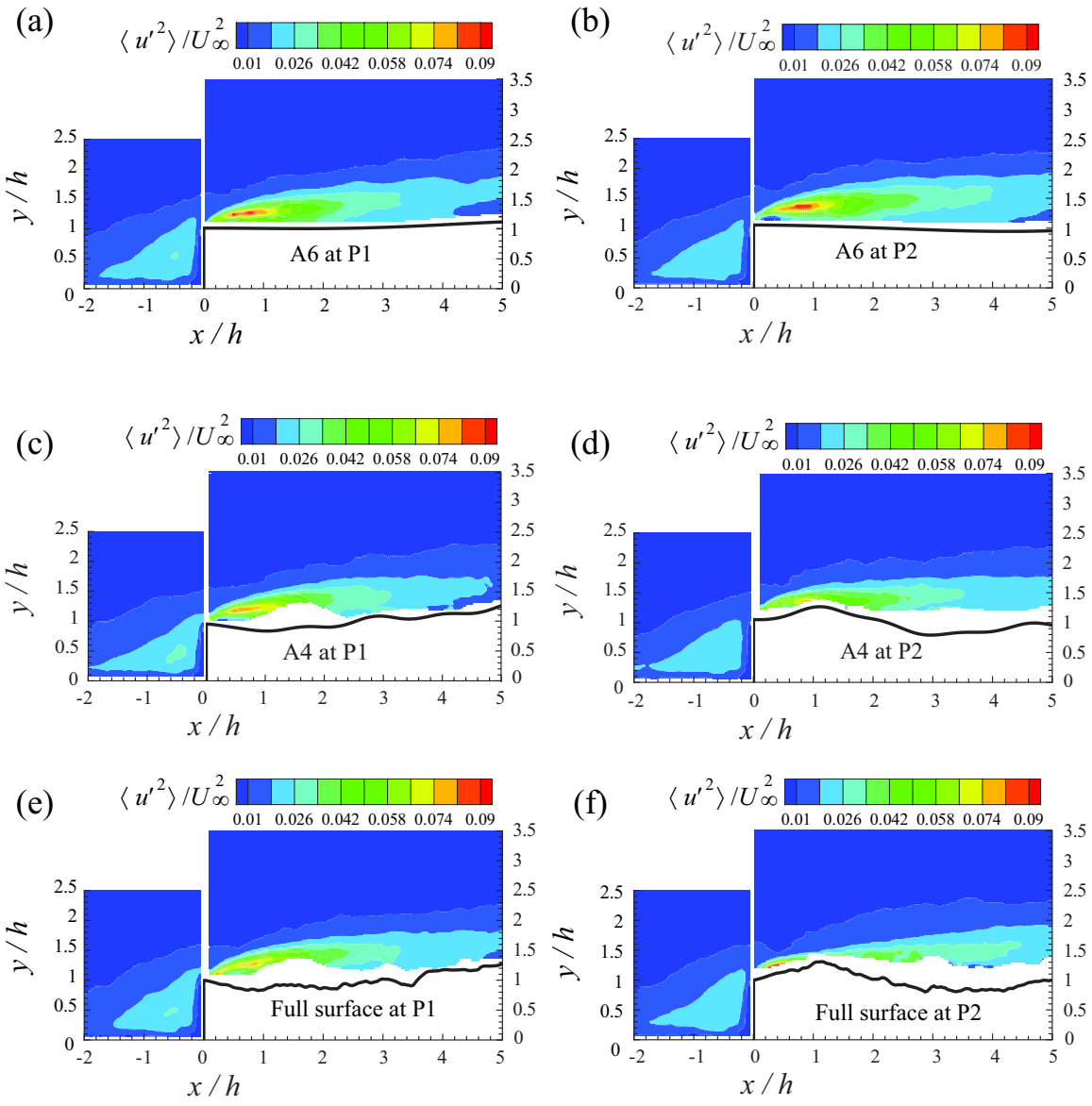

Figure 5.2: Contour of the streamwise Reynolds stress, $\frac{\langle u'^2 \rangle}{U_\infty^2}$, for (a) step A6 at position P1, (b) step A6 at position P2, (c) step A4 at position P1, (d) step A4 at position P2, (e) step of full surface at position P1, and (f) step of full surface at position P2.

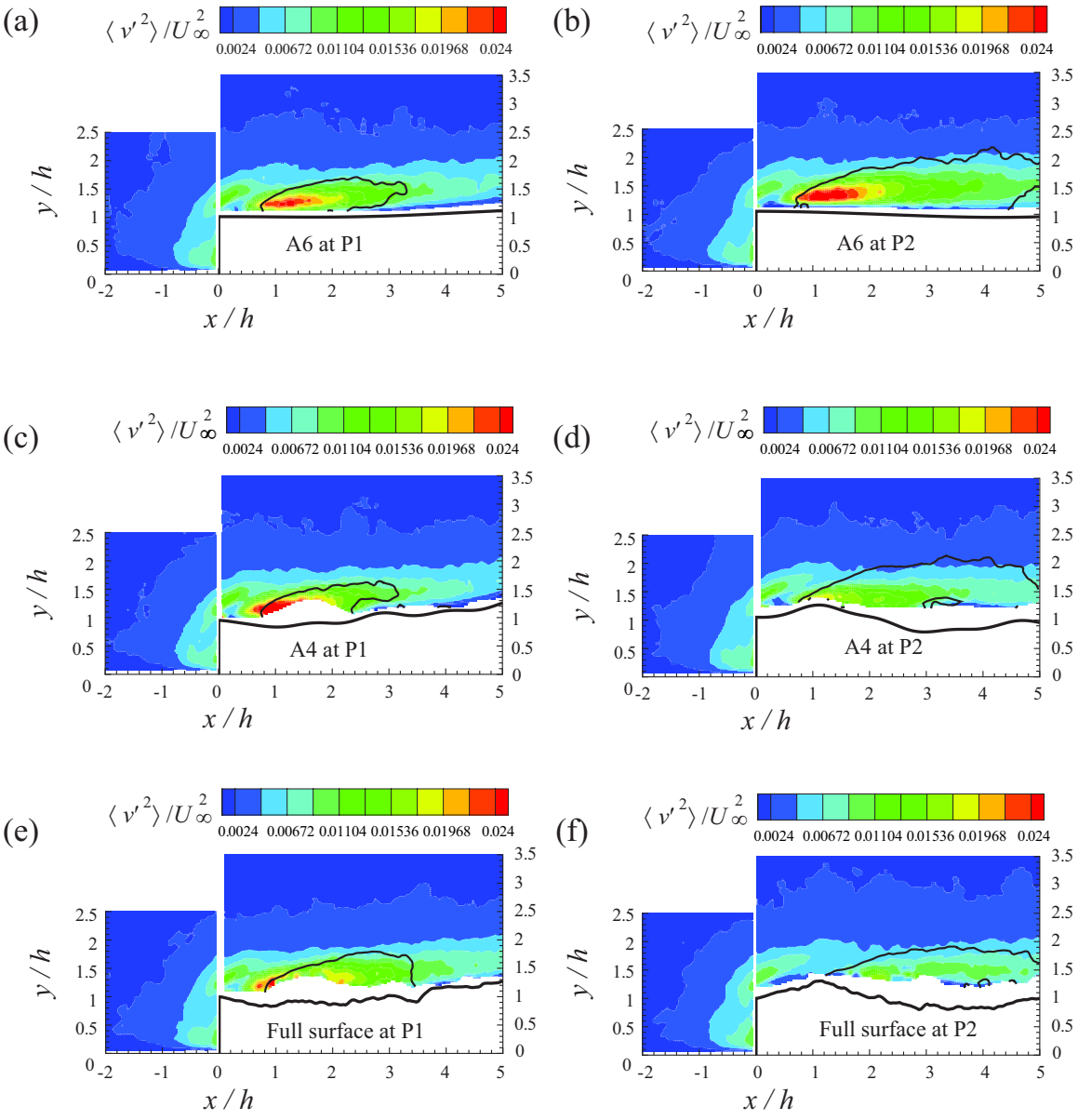

Figure 5.3: Contour of wall-normal Reynolds stress, $\frac{\langle v'^2 \rangle}{U_\infty^2}$, for (a) step A6 at position P1, (b) step A6 at position P2, (c) step A4 at position P1, (d) step A4 at position P2, (e) step of full surface at position P1, and (f) step of full surface at position P2. Line contour of $V = 0$ is overlaid in the downstream region of the FFS flow. $V < 0$ within the region enclosed by this contour line and $V > 0$ outside of this contour line.

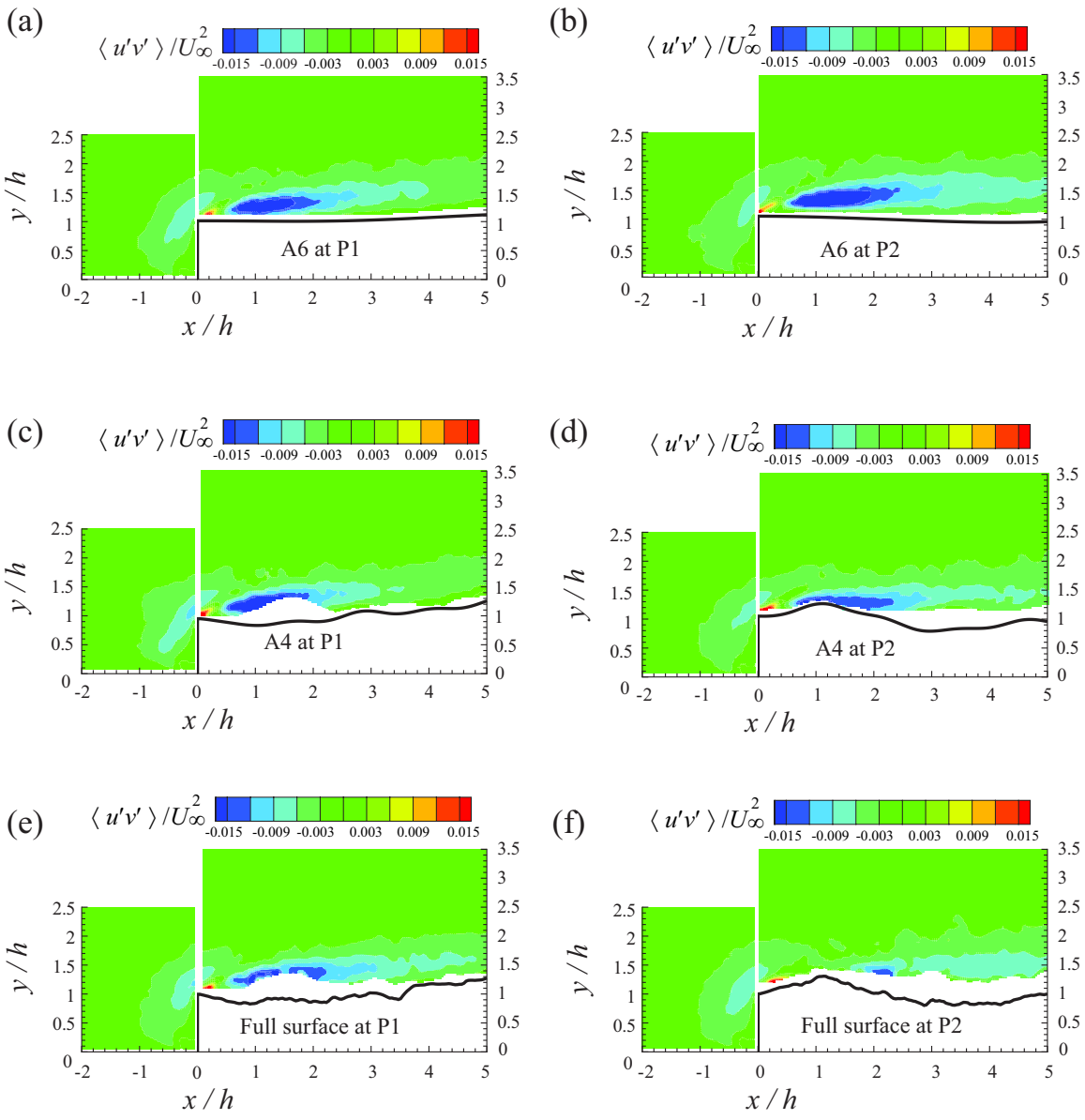

Figure 5.4: Contour of the Reynolds shear stress, $\frac{\langle u'v' \rangle}{U_\infty^2}$, for (a) step A6 at position P1, (b) step A6 at position P2, (c) step A4 at position P1, (d) step A4 at position P2, (e) step of full surface at position P1, and (f) step of full surface at position P2.

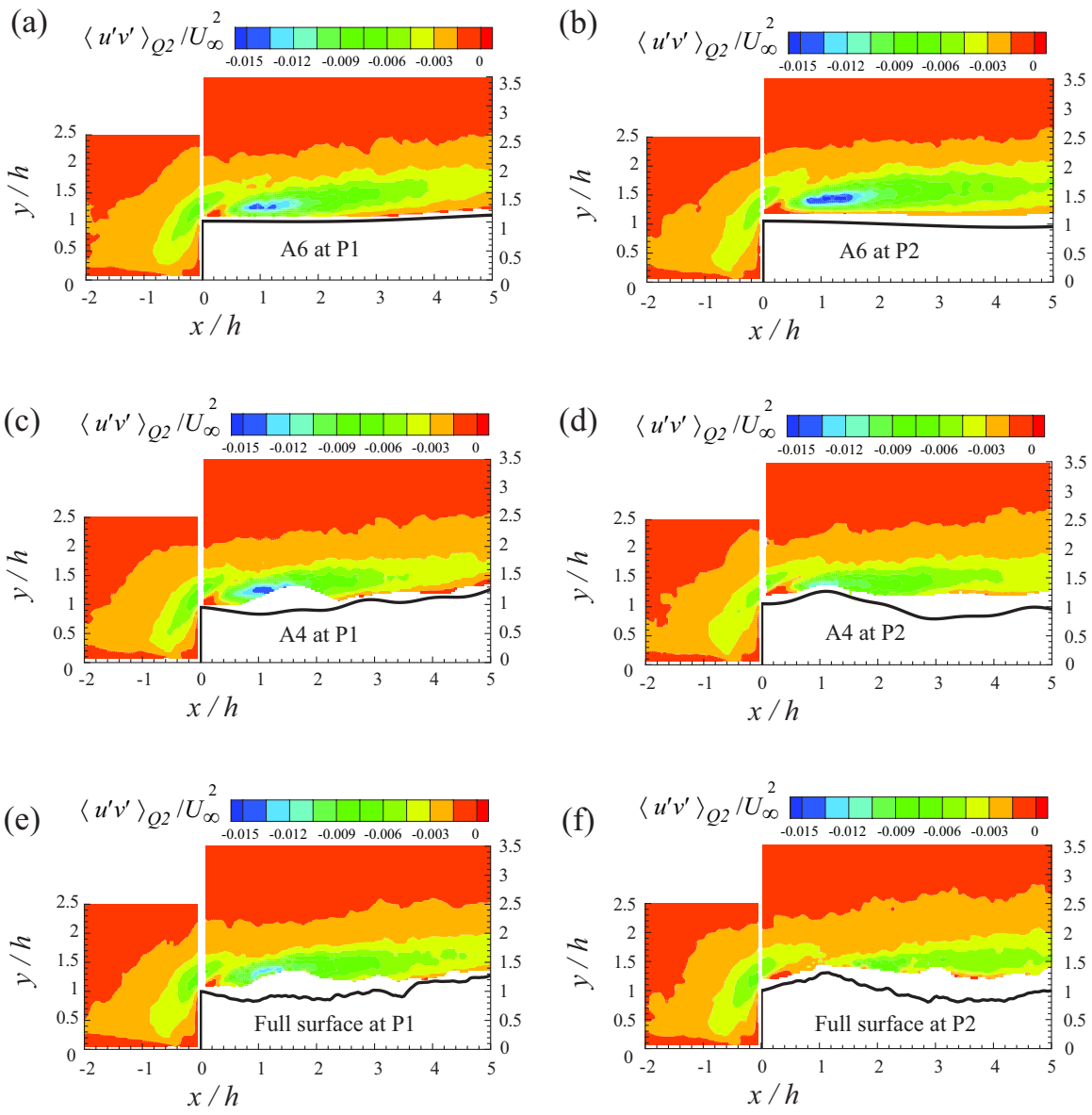

Figure 5.5: Reynolds shear stress contributions from ejections ($Q2$ event) for the threshold of $H = 0$ for (a) step A6 at position P1, (b) step A6 at position P2, (c) step A4 at position P1, (d) step A4 at position P2, (e) step of full surface at position P1, and (f) step of full surface at position P2.

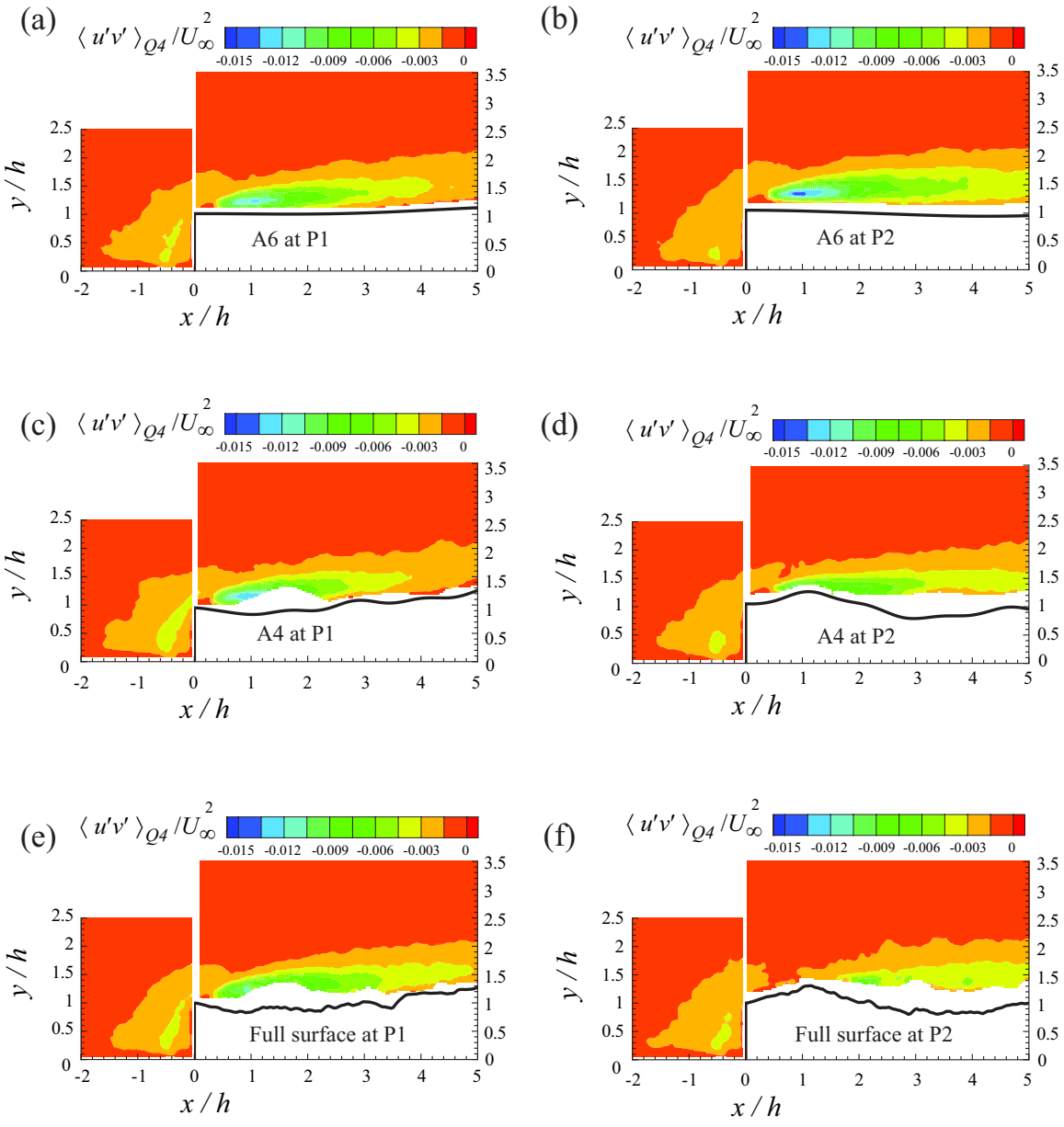

Figure 5.6: Reynolds shear stress contributions from sweeps ($Q4$ event) for the threshold of $H = 0$ for (a) step A6 at position P1, (b) step A6 at position P2, (c) step A4 at position P1, (d) step A4 at position P2, (e) step of full surface at position P1, and (f) step of full surface at position P2.

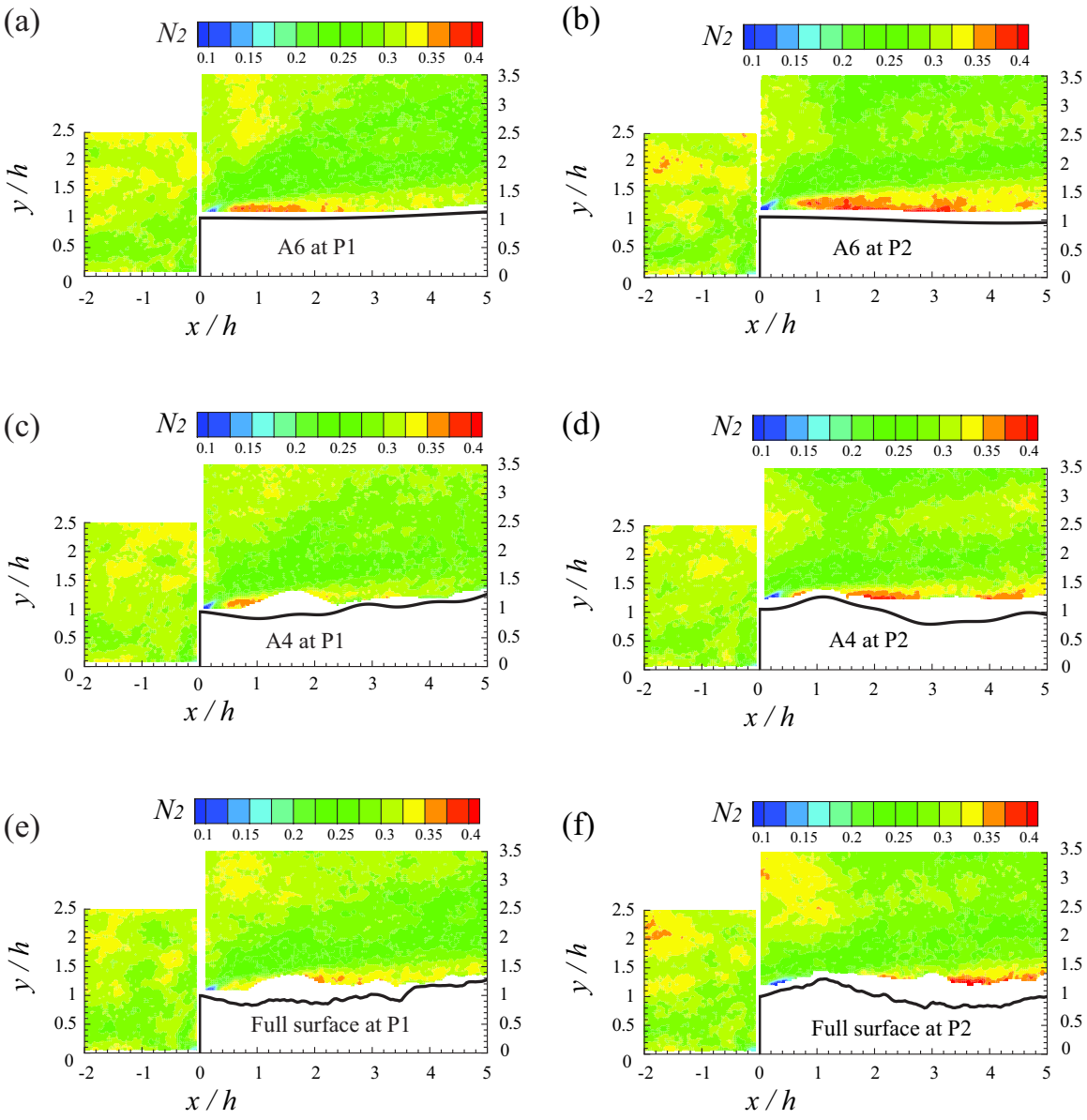

Figure 5.7: Space fractions, for a threshold of $H = 0$, occupied by ejections ($Q2$ event) for (a) step A6 at position P1, (b) step A6 at position P2, (c) step A4 at position P1, (d) step A4 at position P2, (e) step of full surface at position P1, and (f) step of full surface at position P2.

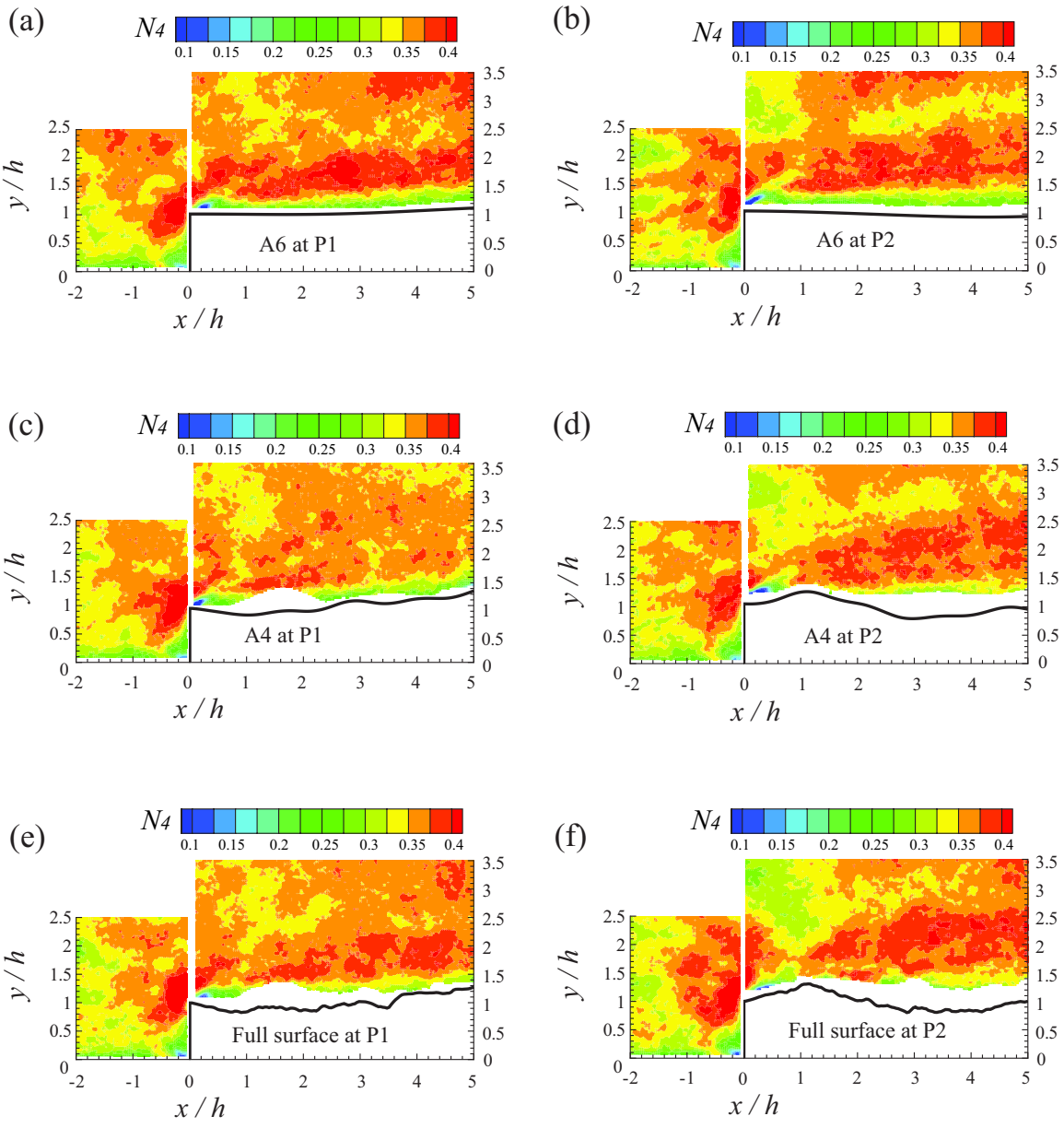

Figure 5.8: Space fractions, for a threshold of $H = 0$, occupied by sweeps ($Q4$ event) for (a) step A6 at position P1, (b) step A6 at position P2, (c) step A4 at position P1, (d) step A4 at position P2, (e) step of full surface at position P1, and (f) step of full surface at position P2.

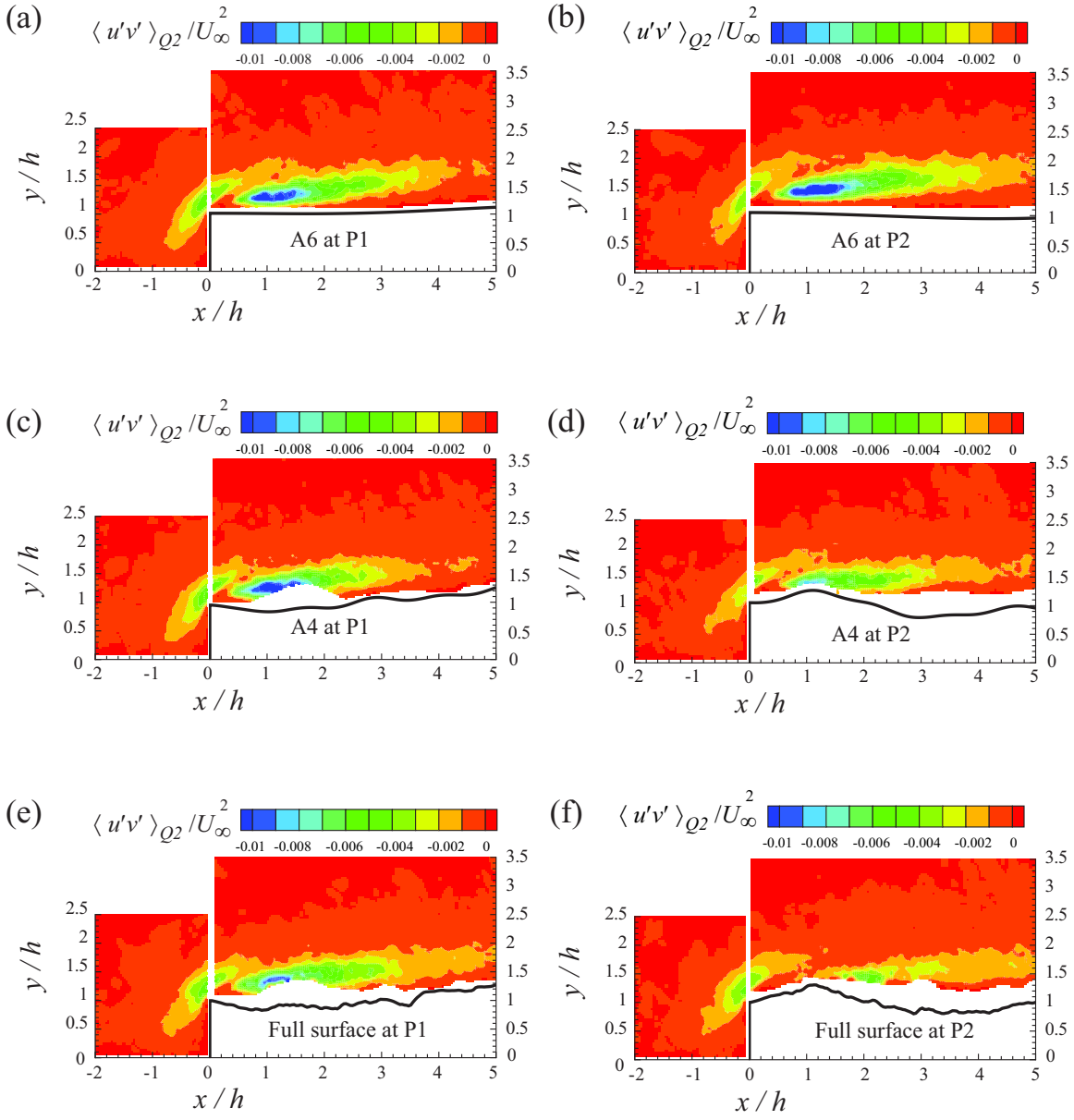

Figure 5.9: Reynolds shear stress contributions from ejections ($Q2$ event) for the threshold of $H = 4$ for (a) step A6 at position P1, (b) step A6 at position P2, (c) step A4 at position P1, (d) step A4 at position P2, (e) step of full surface at position P1, and (f) step of full surface at position P2.

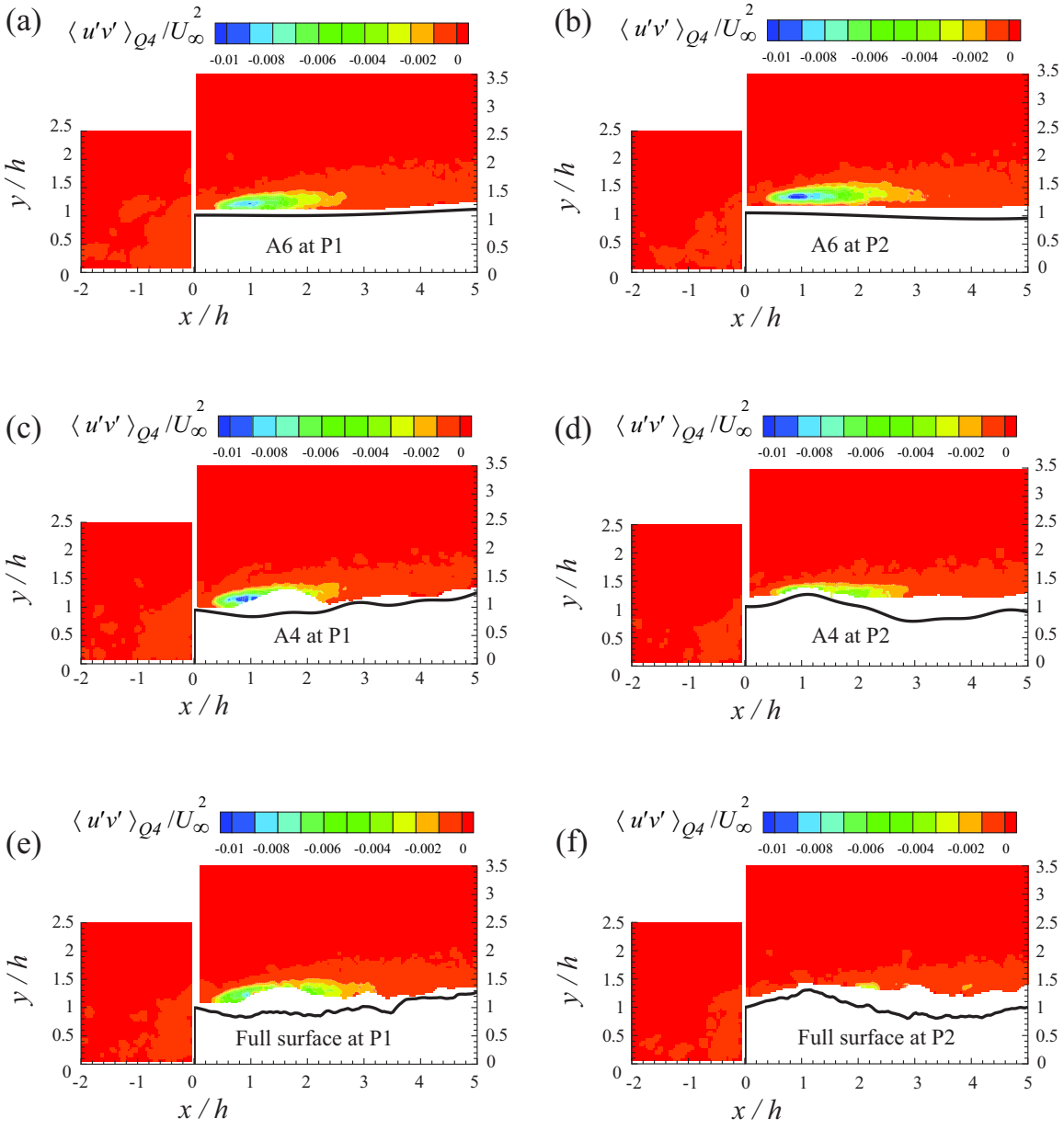

Figure 5.10: Reynolds shear stress contributions from sweeps ($Q4$ event) for the threshold of $H = 4$ for (a) step A6 at position P1, (b) step A6 at position P2, (c) step A4 at position P1, (d) step A4 at position P2, (e) step of full surface at position P1, and (f) step of full surface at position P2.

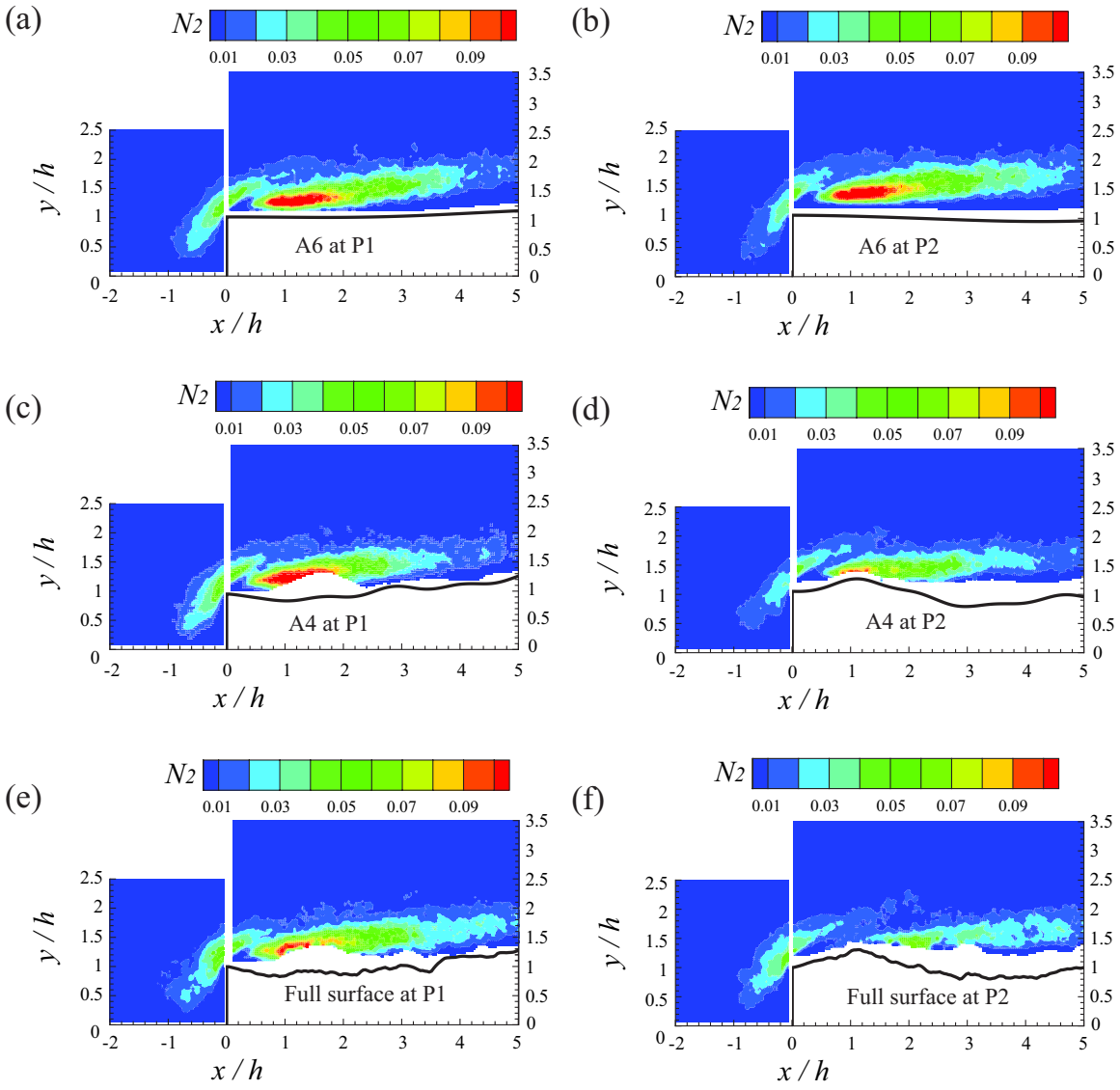

Figure 5.11: Space fractions, for a threshold of $H = 4$, occupied by ejections ($Q2$ event) for (a) step A6 at position P1, (b) step A6 at position P2, (c) step A4 at position P1, (d) step A4 at position P2, (e) step of full surface at position P1, and (f) step of full surface at position P2.

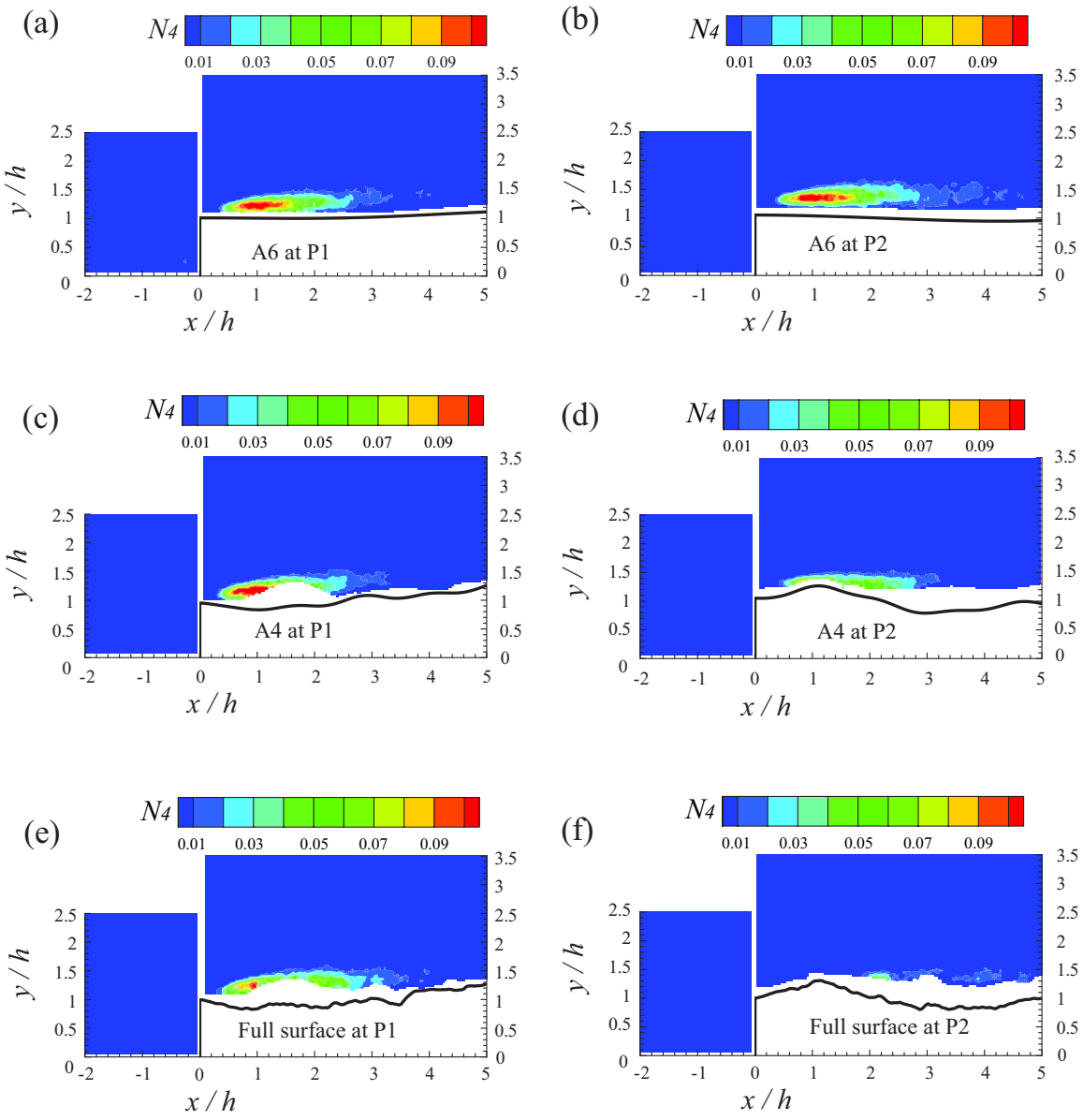

Figure 5.12: Space fractions, for a threshold of $H = 4$, occupied by sweeps ($Q4$ event) for (a) step A6 at position P1, (b) step A6 at position P2, (c) step A4 at position P1, (d) step A4 at position P2, (e) step of full surface at position P1, and (f) step of full surface at position P2.

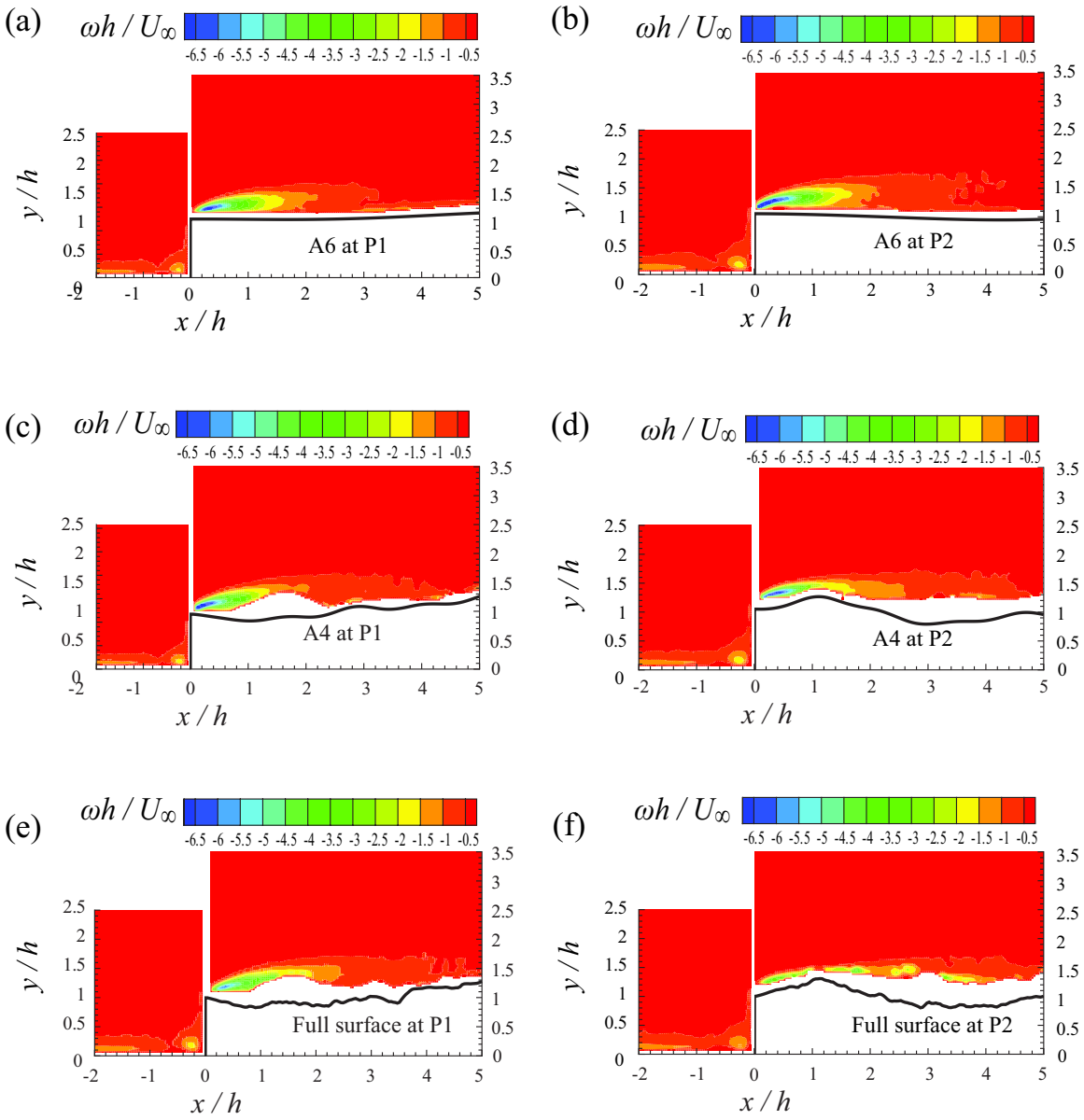

Figure 5.13: Ensemble averaged Spanwise vorticity for (a) step A6 at position P1, (b) step A6 at position P2, (c) step A4 at position P1, (d) step A4 at position P2, (e) step of full surface at position P1, and (f) step of full surface at position P2.

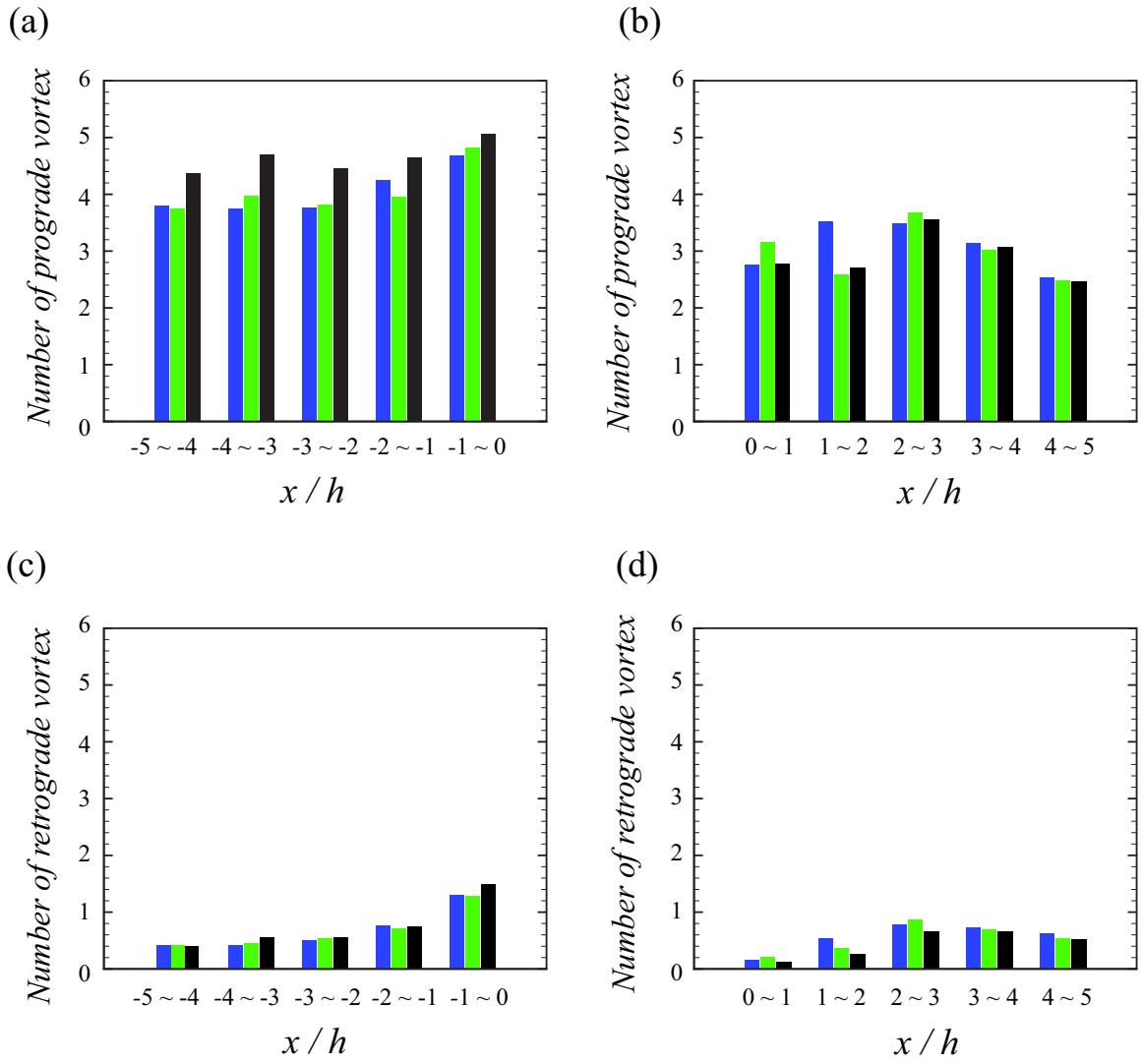

Figure 5.14: Number of spanwise vortices per field at measurement position P1. (a) Prograde ($R_{\lambda\omega} < 0$) vortices upstream of the step, (b) prograde vortices downstream of the step, (c) retrograde ($R_{\lambda\omega} > 0$) vortices upstream of the step, (d) retrograde vortices downstream of the step. Blue (left) bar is for step A6, green (middle) bar is for step A4, and black (right) bar is for step of full surface.

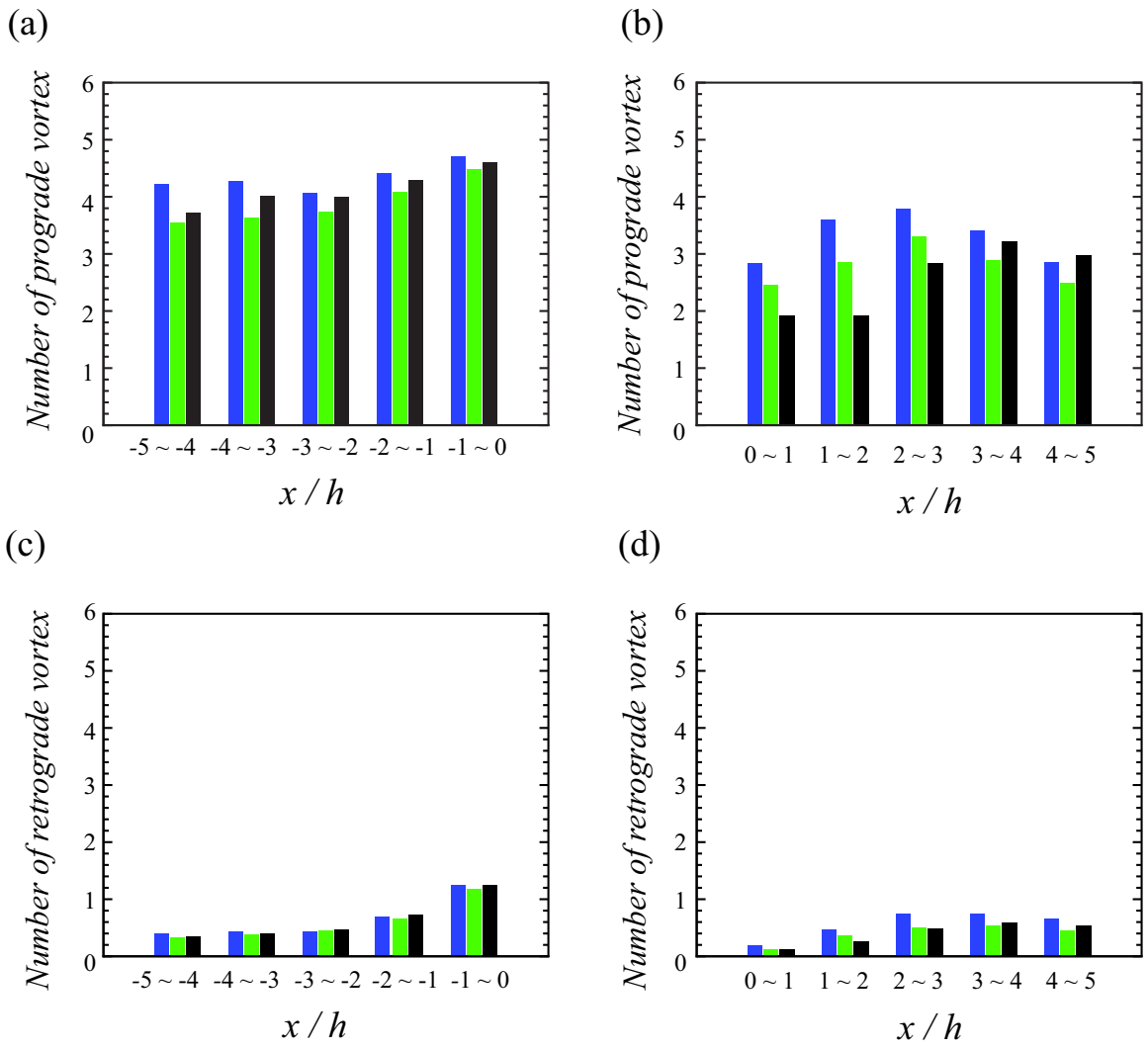

Figure 5.15: Number of spanwise vortices per field at measurement position P2. (a) Prograde ($R_{\lambda\omega} < 0$) vortices upstream of the step, (b) prograde vortices downstream of the step, (c) retrograde ($R_{\lambda\omega} > 0$) vortices upstream of the step, (d) retrograde vortices downstream of the step. Blue (left) bar is for step A6, green (middle) bar is for step A4, and black (right) bar is for step of full surface.

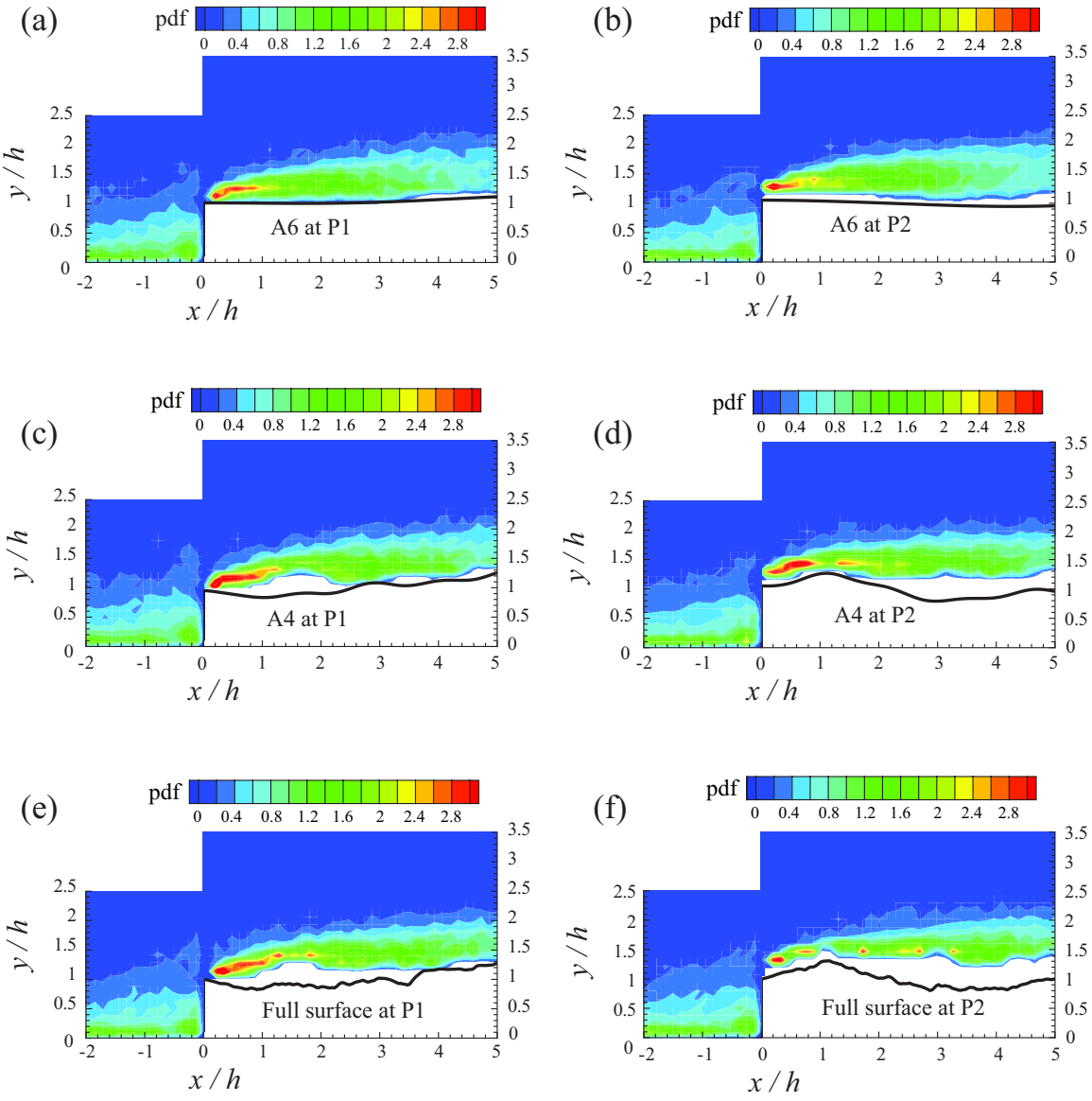

Figure 5.16: Spatial probability distributions of prograde vortices for (a) step A6 at position P1, (b) step A6 at position P2, (c) step A4 at position P1, (d) step A4 at position P2, (e) step of full surface at position P1, and (f) step of full surface at position P2.

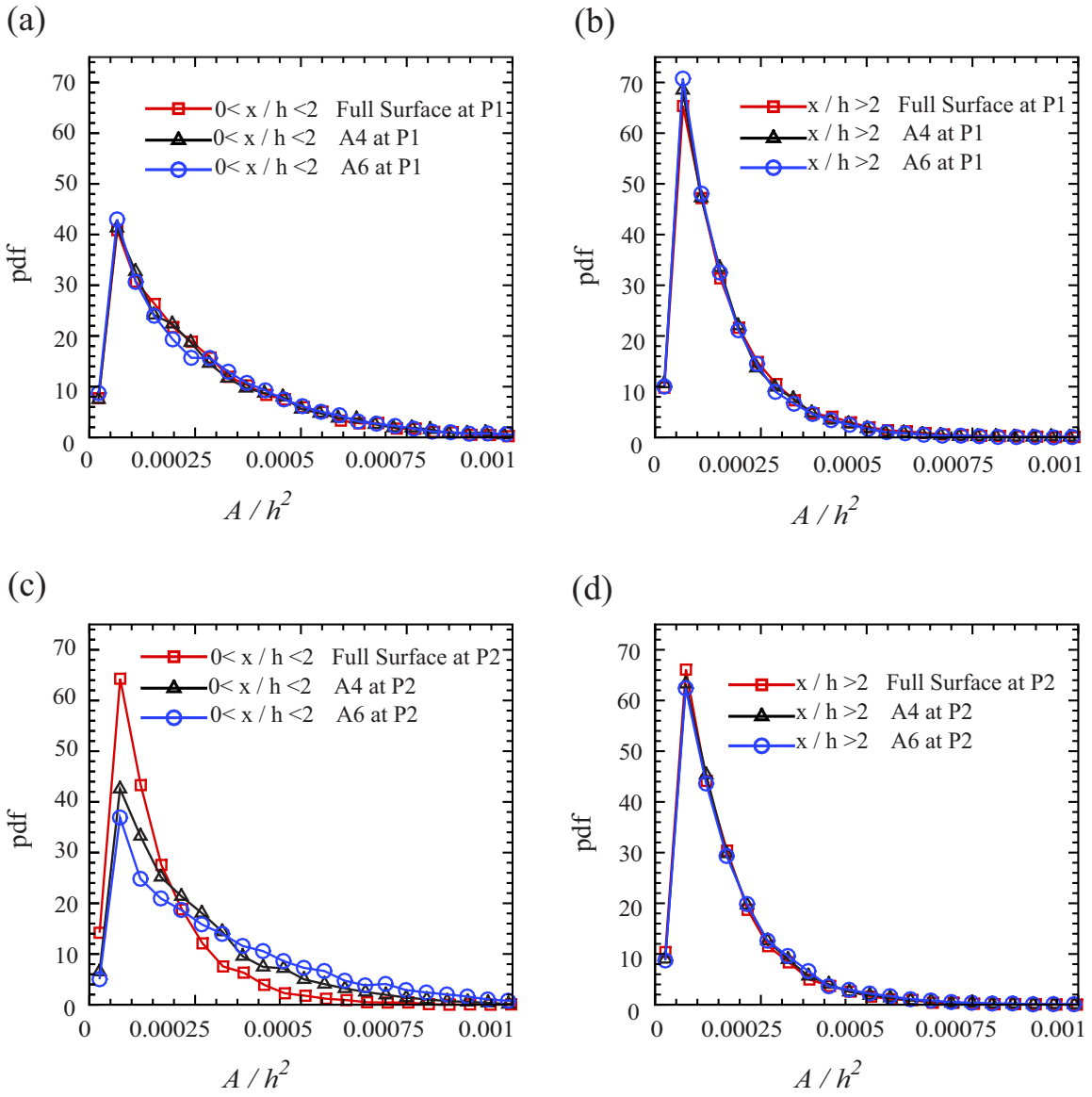

Figure 5.17: Comparison of probability density functions of the sizes of the prograde vortices downstream of the steps A6, A4 and full surface for (a) $0 < x/h < 2$ at measurement position P1, (b) $x/h > 2$ at position P1, (c) $0 < x/h < 2$ at position P2, and (d) $x/h > 2$ at position P2. Every other data is shown.

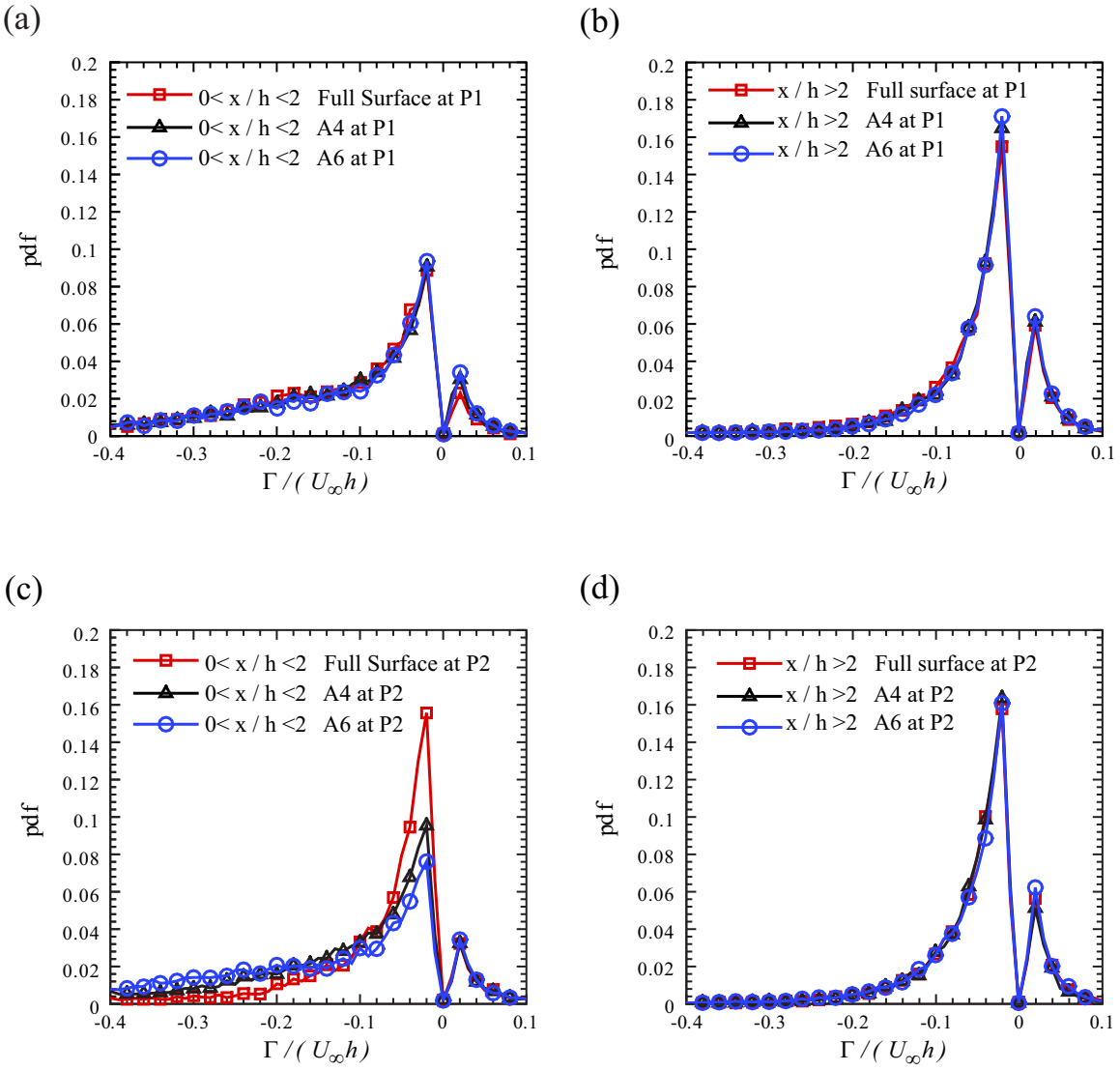

Figure 5.18: Comparison of probability density functions of the circulation of both prograde and retrograde spanwise vortices downstream of the steps A6, A4 and full surface (a) $0 < x/h < 2$ at measurement position P1, (b) $x/h > 2$ at position P1, (c) $0 < x/h < 2$ at position P2, and (d) $x/h > 2$ at position P2. Every other data is shown.

Summary and Conclusions

This chapter summarizes the results which are found by comparing the turbulent boundary layers over smooth and rough forward-facing-steps as well as the rough step's two coarse scale-resolution approximations at two different spanwise positions. The roughness topography on the top surface of the rough step is replicated from a realistic turbine blade and its coarse scale resolution approximations are obtained from multi-resolutional analysis using DWT.

6.1 The effects of realistic roughness on the forward-facing turbulent flow

The results show that the upstream recirculation region is little affected by the surface topography on top of the surface. However, the flow in the downstream recirculation region on the step's top surface is strongly dependent on the specific roughness topographies. These results indicate that there exists insignificant upstream propagation of the disturbances of the flow caused by the roughness on the top surface of the forward-facing step. The effects of the realistic roughness topography on the turbulent flow downstream of the forward-facing step are summarized below.

For the ensemble average velocity fields, the separation bubble is not observable at measurement position P2 where the roughness profile illustrates a positive slope which may generate a local favorable pressure gradient in the flow. In the measurement plane at

P1 where a negative slope exists in the roughness profile at the leading edge of the FFS, a similar recirculation bubble to that over the smooth step is still observed but its center location is slightly shifted downstream. As such, the mean flow structures become to be highly three dimensional downstream of the rough step's leading edge due to the three-dimensional topographical features of the roughness on the top surface.

For the Reyonlds stresses, $\langle u'^2 \rangle$, $\langle v'^2 \rangle$ and $\langle u'v' \rangle$, they are obviously inhibited downstream of the steps, especially at measurement position P2 where a positive slope exists immediately after the step's sharp edge. Two dimensional quadrant analysis revealed that the intermittent strong ejections are still the most Reynolds shear stress contributors, which is similar to the turbulent boundary layer. However, most ejections occur further away from the step's top surface while most sweeps occur and contribute to $\langle u'v' \rangle$ closer to the top wall of the step. The roughness is observed to reduce the shear stress contributions from both ejections and sweeps and the positive slope of the roughness profile at P2 is more effective in this regard.

The ensemble averaged spanwise vorticity fields show that the vorticity in the downstream recirculation region after the sharp edge of the step is strongly affected by the surface conditions. The peak vorticity in the shear layer downstream of the rough step is found to be decreased compared to the smooth-step case, especially at P2 where the flow separation is prevented due to the favorable pressure gradient caused by a positive slope of the roughness. In addition, at measurement position P2, elevated vorticity is noticed to be sustained by the surface roughness much further downstream when compared with the smooth-step case.

The number of coherent spanwise prograde vortices is significantly reduced within 2 h downstream of the rough step at position P2 compared that that over the smooth FFS. About 40% less prograde vortices are also observed for the rough step at P1 in the region between 1 h and 2 h downstream of the step. Though the spatial distributions of the prograde vortices ahead of the steps are not observed to be different, those downstream of the steps

are apparently affected by the roughness conditions. The size distributions of the prograde vortices observed downstream of the steps show that although majority of the them have the same size, there is much less chances to find large prograde vortices for the rough step at P2 with a positive roughness slope. However, the size distributions of prograde vortices over the smooth and rough step at P1 with a negative roughness slope are about the same. The circulation distributions of the vortices downstream of the steps show that there exists significantly less possibilities for the vortices at P2 to have large circulation. On the other hand, the size and circulation distributions of vortices upstream of the step are insensitive to the surface roughness conditions on the top surface.

The results presented illustrate that the rough surface conditions on the top surface of the forward-facing step tend to weaken the separated flows from the sharp edge. The comparison of the results at two different measurement positions indicates that the slope of the roughness profile immediately after the step's edge plays an important role in affecting the flow. This is probably due to the local pressure gradients induced by the roughness topography. A relatively strong favorable pressure gradient may prevent the generation of recirculation region downstream of the step. However, the welcoming effects of the roughness may only be confined within $2\sim3$ h downstream of the sharp edge of the step.

In a very recent study of aerodynamical performance of a bio-inspired airfoil from the dragonfly's wing for Micro Air Vehicle applications, Murphy & Hu (2010) found that a corrugated airfoil performed best in preventing the large-scale flow separation compared to a flat plate and a profiled airfoil as shown in figure 6.1. The authors argued that the separated laminar flow from the sharp edge of the corrugated airfoil was transitioned rapidly into a turbulent flow as it approached to the first protruding corner. With a high-momentum turbulent flow, large-scale separation was reduced by the corrugated airfoil. The current results may indicate that the strong positive slope windward of the first protruding corner in the corrugated airfoil also helps prevent the flow from separating. It may be speculated that if the turbulent flow generated by the laminar-flow separation by the sharp edge encoun-

tered a negative slope of a corrugated airfoil, it probably will maintain separated further downstream. It seems that the natural evolution has made the dragonfly's corrugated wing to provide two guards again flow separation. One is to transit laminar flow to turbulent flow fast to gain higher momentum and the other is to provide a strong local favorable pressure gradient by a positive slope in the wing's profile.

The current results also suggest that to avoid the fluctuating loads on the wind turbine sited on top of coastal cliffs, the preferred siting may be where the cliffs have a slope that is inclined in the direction of wind.

6.2 The effects of roughness length scales on the forward-facing turbulent flow

Ensemble averaged velocity fields show that the mean flow structure of the downstream recirculation region is distorted by the waviness of the large-scale roughness in step A6, a very coarse scale-resolution approximation of the rough step. The mean flow structure of step A4 is found to be qualitatively similar to that of full surface step. However, the streamwise location of the downstream recirculation bubble appear to be still slightly affected by the fine-scale roughness excluded from step A4.

Reynolds stresses downstream of the step are shown to be slightly changed by the specific topographical features of the large-scale roughness in step A6 compared with the smooth step case. The fine-scale roughness included in step A4 weakens the Reynolds stresses, especially at position P2 where a positive slope in the roughness profile is produced immediately after the step's front. Although the Reynolds stresses over step A4 are only a bit smaller than those over the full surface step at measurement position P1, a significant reduction in Reynolds stresses was found around the local roughness peak (around $x = 1h$) by the finest roughness scales excluded from A4 at position P2. Quadrant analysis also reveals a smaller difference in shear stress contributions and space fractions of ejec-

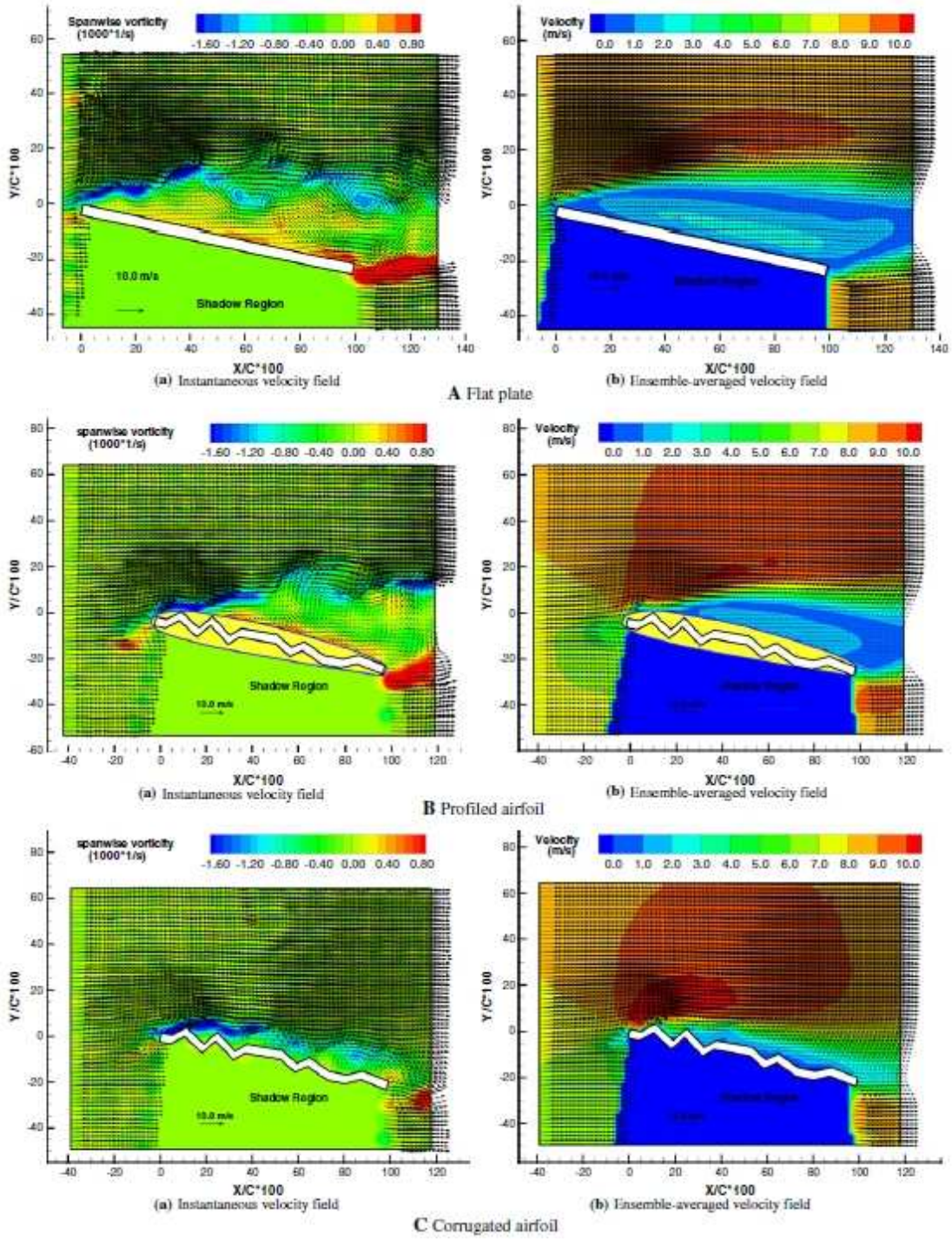

Figure 6.1: PIV measurements for a plat plate, profiled airfoil and a corrugated airfoil at angle of attach of 12°. Murphy & Hu (2010).

tions and sweeps at position P1 than at position P2 between steps of different roughness length scales.

At position P1, the peak value of the ensemble averaged spanwise vorticity downstream of the step is observed not to be altered from step A6 to A4 but slightly reduced from A4 to full surface. At P2, the reduction of vorticity is more dramatic from A4 to full surface than from A6 to A4. Few changes are found in the spatial characteristics of coherent spanwise vortices at position P1 between steps A6, A4 and full surface. In contrast, successive inclusion of finer roughness length scales from A6 to full surface significantly changes the characteristics of prograde spanwise vorticies observed within $2h$ downstream of the step at position P2.

The observations made in this project show that the step approximation A4 which contains almost 90% of the rough surface energy cannot reproduce faithfully the characteristics of turbulent boundary layer over the step of full roughness studied herein. Finer length scale roughness needs to be included in the surface topography in order to improve the reproduction of the turbulent flow by step approximations. As shown in figure 2.2, the next level of rough-surface approximation, A3, will contain 97.3% of the roughness energy. As such, A3 will be comparable to 16-mode model (which contains 95% of the roughness energy) from POD analysis in the study of Mejia-Alvarez & Christensen (2010) in terms of the details of the roughness features included in the surface topography. Therefore, DWT does not have any advantage against POD in terms of reducing the complexity of the current roughness for the forward-facing step turbulent flows. Nevertheless, as illustrated in Chapter 2, DWT simplified roughness holds the advantages of being invariant to the surface sample size and being smoother, which is more lenient in grid generation for CFD efforts.

The results also show that the characteristics of the turbulent flows over step A4 and full surface at position P1 are quite similar while the flows at position P2 are significantly distinct between A4 and full surface. Therefore, the impacts of the finer scale roughness excluded in A4 on the separated turbulent flow downstream of the step's front appear to

depend strongly on the specific topographical features of the roughness. The current results indicate that if the leading roughness profile has a negative slope, the FFS flow is little affected by the finer roughness length scales while if the leading roughness profile has a positive slope, the impacts of the finer roughness scales are quite dramatic. It is indicated that it is more critical to include sufficiently fine scale roughness in the step approximation to replicate the leading *positive* slope in the full roughness topography in order to produce more similar FFS turbulent flows. In addition, since the major differences in flows at position P2 between step A4 and full surface lie within $2h$ downstream of the step's front, finer roughness scales may need to the included only in this region of the surface approximation to reduce the difference in the characteristics of the flows. Therefore, in order to find a step approximation with reduced roughness complexity to reproduce the turbulent flow over a realistic rough step, multiple scale resolutions may need to be used with finer scale resolution in the part of surface topography that has a larger impact on the turbulent flow.

Bibliography

ADDAD, Y., LAURENCE, D., TALOTTE, C. & JACOB, M. 2003 Large eddy simulation of a forward-backward facing step for acoustic source identification. *International Journal of Heat and Fluid Flow* **24**, 562–571.

AGELINCHAAB, M. & TACHIE, M. 2008 PIV study of separated and reattached open channel flow over surface mounted blocks. *Journal of Fluids Engineering* **130**, 1–9.

BANDYOPADHYAY, P. R. & WATSON, R. D. 1988 Structure of rough-wall turbulent boundary layers. *Phys. Fluids* **31**, 1877–1883.

BONS, J., MCCLAIN, S., WANG, Z., CHI, X. & SHIH, T. 2008 A comparison of approximate versus exact geometrical representations of roughness for CFD calculations of c_f and s_t. *J. Turbomach.* **130**, 021024–1–10.

BONS, J. P. 2002 s_t and c_f augmentation for real turbine roughness with elevated freestream turbulence. *J. Turbomach.* **124**, 632–644.

BONS, J. P., TAYLOR, R. P., MCCLAIN, S. T. & RIVIR., R. B. 2001 The many faces of turbine surface roughness. *J. Turbomach.* **123**, 739–748.

BRADSHAW, P. & WONG, F. 1972 The reattachment and relaxation of a turbulent shear layer. *J. Fluid Mech.* **52** (1), 113–135.

CAMUSSI, R., FELLI, M., PEREIRA, F., ALOISIO, G. & MARCO, A. D. 2008 Statistical properties of wall pressure fluctuations over a forward-facing step. *Phys. Fluids* **20**, 075113–1 075113–13.

CHAKRABORTY, P., BALACHANDAR, S. & ADRIAN, R. J. 2005 On the relationships between local vortex identification schemes. *J. Fluid Mech.* **535**, 189–214.

CHONG, M., PERRY, A. & CANTWELL, B. 1990 A general classification of three-dimensional flow fields. *Phys. Fluids* **2** (5), 765–777.

DAUBECHIES, I. 1992 *Ten Lectures on Wavelets*. Philadelphia, PA: Society for Industrial and Applied Mathematics.

DUBIEF, Y. & DELCAYRE, F. 2000 On coherent-vortex identification in turbulence. *Journal of Turbulence* **1** (11), 1–22.

GASSET, N., POITRAS, G., GAGNON, Y. & BROTHERS, C. 2005 Study of atmospheric boundary layer flows over a coastal cliff. *Wing Engineering* **29** (1), 3–24.

GRGIC, S., GRGIC, M. & ZOVKO-CIHLAR, B. 2001 Performance analysis of image compression using wavelets. *IEEE Transactions on Industrial Electronics* **48** (3), 682–695.

HUNT, J., WRAY, A. & MOIN, P. 1988 Eddies, stream, and convergence zones in turbulent flows. *Tech. Rep.* Report CTR-S88. Center for Turbulence Research.

JEONG, J. & HUSSAIN, F. 1995 On the identification of a vortex. *J. Fluid Mech.* **285**, 69–94.

JI, M. & WANG, M. 2010 Aeroacoustics of turbulent bounday-layer flow over small steps. In *AIAA-2010-6*.

JIMENEZ, J. 2004 Turbulent flow over rough wall. *Annu. Rev. Fluid Mech.* **36**, 173–196.

JOHNSON, B. & CHRISTENSEN, K. 2009 Turbulent flow over low-order models of highly-irregular surface roughness. *AIAA J.* **47** (5), 1288–1299.

KIYA, M. & SASAKI, K. 1983 Structure of a turbulent separation bubble. *Journal of Fluid Mechanics* **137**, 83–113.

KUMAR, P. & FOUFOULA-GEORGIOU, E. 1997 Wavelet analysis for geophysical applications. *Reviews of Geophysics* **35** (4), 385–412.

LARGEAU, J. & MORINIERE, V. 2007 Wall pressure fluctuations and topology in separated flows over a forward-facing step. *Exp Fluids* **42**, 21–40.

LECLERCQ, D., JACOB, M., LOUISOT, A. & TALOTTE, C. 2001 Forward-backward facing step pair: aerodynamic flow, wall pressure and acoustic characterisation. In *AIAA-2001-2249*.

LIANG, H. & LIN, Z. 2002 Multiresolution signal decomposition and its applications to electrogastric signals. *Recent Res. Devel. Biomed. Engi.* **1**, 15–31.

MALLAT, S. 1989 A theory for multiresolution signal decomposition: the wavelet representation. *IEEE Trans. Pattern Anal. Mach. Intell.* **11** (7), 674–693.

MEJIA-ALVAREZ, R. & CHRISTENSEN, K. 2010 Low-order representations of irregular surface roughness and their impact on a turbulent boundary layer. *Physics of Fluids* **22**, 015106.

MOSS, W. & BAKER, S. 1980 Re-circulating flows associated with two-dimensional steps. *Aeronautical Quarterly* (151-172).

MURPHY, J. & HU, H. 2010 An experimental study of a bio-inspired corrugated airfoil for micro air vehicle applications. *Exp. Fluids* **49**, 531–546.

NAGAOSA, R. & HANDLER, R. 2003 Statistical analysis of coherent vortices near a free surface in a fully developed turbulence. *Phys. Fluids* **15** (2), 375–394.

NATRAJAN, V. K., WU, Y. & CHRISTENSEN, K. T. 2007 Spatial signatures of retrograde spanwise vortices in wall turbulence. *J. Fluid Mech.* **574**, 155–167.

RAUPACH, M. R., ANTONIA, R. A. & RAJAGOPALAN, S. 1991 Rough-wall turbulent boundary layers. *Appl. Mech. Rev.* **44**, 1–25.

SCARANO, F. 2002 Iterative image deformation methods in PIV. *Meas. Sci. Technol.* **13**, R1–R19.

SCHRAM, C., RAMBAUD, P. & RIETHMULLER, M. L. 2004 Wavelet based eddy structure eduction from a backward facing step flow investigated using particle image velocimetry. *Exp. Fluids* **36**, 233–245.

SCHULTZ, M. P. & FLACK, K. A. 2009 Turbulent boundary layers on a systematically varied rough wall. *Phys. Fluids* **21**, 015104.

SHERRY, M., JACONO, D., SHERIDAN, J., MATHIS, R. & MARUSIC, I. 2009 Flow separation characterisation of a forward facing step immersed in a turbulent boundary layer. In *Sixth International Symposium on Turbulence and Shear Flow Phenomena*. Seoul, Korea.

WU, Y. & CHRISTENSEN, K. T. 2006 a Reynolds-stress enhancement associated with a short fetch of roughness in wall turbulence. *AIAA J.* **44**, 3098.

WU, Y. & CHRISTENSEN, K. T. 2006 b Population trends of spanwise vortices in wall turbulence. *J. Fluid Mech.* **568**, 55–76.

WU, Y. & CHRISTENSEN, K. T. 2007 Outer-layer similarity in the presence of a practical rough-wall topography. *Phys. Fluids* **19**, 085108.

WU, Y. & CHRISTENSEN, K. T. 2010 Spatial structure of a turbulent boundary layer with irregular surface roughness. *J. Fluid Mech.* **655**, 380–418.

ZHOU, J., ADRIAN, R. J., BALACHANDAR, S. & KENDALL, T. M. 1999 Mechanisms for generating coherent packets of hairpin vortices in channel flow. *J. Fluid Mech.* **387**, 353–396.